

Functional Polymers with Defined Architecture for Biointerface Interactions: From Nanoparticles to Nanosheets

Inaugural-Dissertation

to obtain the academic degree

Doctor rerum naturalium (Dr. rer. nat.)

submitted to the Department of Biology, Chemistry, Pharmacy
of Freie Universität Berlin

by

Vahid Ahmadi Soureshjani

From Esfahan, Iran

Berlin 2021

This doctoral dissertation was completed under the supervision of Prof. Dr. Rainer Haag at the Institute of Chemistry and Biochemistry, Freie Universität Berlin, from December 2017 to November 2021. This thesis has been funded by the Federal Ministry of Education and Research of Germany (031B0363F/BMBF) and German Science Foundation (DFG) (SFB 1449).

1. Reviewer: Prof. Dr. Rainer Haag, Freie Universität Berlin

2. Reviewer: PD Dr. Kai Licha, Freie Universität Berlin

Date of defense: ---13.12.2021---

Declaration of independence

All of the content in this thesis is original and has not previously appeared in any form of application for a degree. The works presented herein are entirely my own, except where referenced or acknowledged otherwise.

Berlin, November 2021 ----- (Vahid Ahmadi Soureshjani)

Acknowledgments

Over the past four years, several people have supported me directly and indirectly in my doctoral studies both scientifically and emotionally. Without their help, I would not have been able to accomplish this. First and foremost, I am grateful to my supervisor, Prof. Dr. Rainer Haag, for granting me the opportunity to work in his group and pursue my research interests. Thanks to his guidance, I have had the opportunity to gain a lot of knowledge and experience. Likewise, I would like to thank the second reviewer of this thesis, PD Dr. Kai Licha.

I would like to thank the Federal Ministry of Education and Research of Germany (BMBF) and the German Science Foundation (DFG) for their financial support in running the projects. I would also like to acknowledge the assistance of the Core Facility BioSupraMol, funded by the DFG.

It was my pleasure to work with Prof. Mohsen Adeli in the 2D project, and I gained a great deal of knowledge and experience from him. I would also like to thank Prof. Jürgen P. Rabe and Mohammad Fardin Gholami from Humboldt-Universität zu Berlin for their efforts and valuable input to this project. I would also like to thank Dr. Ievgen S. Donskyi and Dr. Jörg Radnik from Bundesanstalt für Materialforschung und -prüfung (BAM) for their contributions to the characterization of the materials with XPS.

Professor Annika Vogt at Charité-Universitätsmedizin Berlin has been an invaluable collaborator on the dermal drug delivery project, and I am grateful she allowed us to use her facilities. Special thanks go to Dr. Fatemeh Zabihi and Dr. Fiorenza Rancan for performing the skin penetration studies.

Thanks are due to Dr. Chuanxiong Nie, Dr. Walid Azab, Oleksandr Kolyvushko, and Prof. Klaus Osterrieder from Freie Universität Berlin for their great contributions to virus inhibition studies. I would like to thank Elisa Quass, Dr. Katharina Achazi, and Dr. Stefanie Wedepohl for their support in conducting biological studies.

I wish to extend my sincere appreciation to Dr. Wiebke Fischer for her valuable assistance. Further, I would take this opportunity to thank the former and current members of the AG Haag in particular Dr. Ehsan Mohammadifar, Dr. Abbas Faghani, Eike Ziegler Rameez Ahmed, Dr. Mohammad Suman Chowdhury, Dr. Guy Guday, Dr. Matthias Wallert,

Dr. Olaf Wagner, Dr. Raju Bej, Dr. Ievgen S. Donski, Justin Arenhoevel, Daniel Braatz, Mariam Cherri, Xin Fan, Dr. Jose Luis Cuellar Camacho, Dr. Svenja Herziger, and Dr. Manoj Kumar Muthyala. Moreover, I would like to thank my labmates from 33.04, Boonya, Felix, Mathias, Ann-Cathrin, Hanna, Fatemeh, Anja, Wanjun, Manoj, and Paria for creating a positive and harmonious environment. Paria Pouyan is my former classmate in Polymer Science who became a friend, colleague, and labmate when I was in AG Haag. Our close friendship led us to create the NoVirall project, for which we have raised funding jointly, and which we intend to develop further. I also want to thank Ehsan for our interesting coffee talk about scientific and non-scientific topics.

I would like to thank Dr. Pamela Winchester and Ben Allen for proofreading my manuscripts, and Dr. Mathias Dimde, Dr. Katharina Achazi and Dr. Abhishek Kumar Singh for proofreading my thesis.

In the end, none of this would have been possible without my family. My very deep gratitude goes out to my parents, Hamidreza and Bahar, and my sister Nahid for their encouragement, patience, and support during this challenging time.

To my parents,

Hamidreza and Bahar

Table of content

1	Introduction	1
1.1	Polymer architecture.....	2
1.1.1	Linear polymers.....	3
1.1.2	Branched polymers.....	3
1.1.3	Complex polymeric nanoarchitectures	4
1.1.3.1	Non-covalent networks	4
1.1.3.2	Covalent networks.....	5
1.2	Synthesis of well-defined complex polymeric architectures.....	7
1.2.1	Chain growth approach	7
1.2.1.1	Ring-opening polymerization (ROP)	7
1.2.1.2	Anionic ring-opening polymerization (AROP)	9
1.2.1.3	NCA Polymerization	10
1.2.2	Step-growth approach.....	16
1.2.2.1	Azide–alkyne click chemistry	16
1.2.2.2	Architectures obtained from Azide–alkyne click chemistry.....	16
1.2.3	Multistep-growth approach	18
1.3	Antiviral polymers.....	18
1.3.1	Herpesvirus	20
1.3.2	Coronavirus	20
1.3.3	Toolbox for designing antiviral polymers	21
1.3.3.1	Architecture of inhibitors	21
1.3.3.2	Inhibitor size.....	23
1.3.3.3	Surface charge of inhibitors	25
1.3.3.4	Hydrophobicity matters.....	27
1.3.3.5	Multivalency concept	27
1.3.3.6	Virucidal vs. virustatic inhibitors	28
1.4	Polymer for dermal delivery.....	30
1.4.1	Skin structure and penetration pathways	30
1.4.2	Toolbox for designing polymeric dermal carriers	31
1.4.2.1	Architecture of nanocarriers	31
1.4.2.2	Size of nanocarriers	32
1.4.3	Surface charge dictates transdermal fate	33
2	Scientific Goals.....	35
3	Publications.....	38
3.1	Graphene-Assisted Synthesis of 2D Polyglycerols as Innovative Platforms for Multivalent Virus Interactions	38
3.2	One-pot Gram-scale Synthesis of Virucidal Heparin-mimicking Polymers as HSV-1 Inhibitors.....	79
3.3	Amphiphilic Co-polypeptides Self-Assembled into Spherical Nanoparticles for Dermal Drug Delivery	100
4	Conclusion.....	123
5	Short summary	126
6	Kurzzusammenfassung	128
7	References	130
8	Appendix	143
8.1	List of abbreviations	143
8.2	List of publications, patents, and Conference Contributions	146
8.3	Curriculum Vitae	148

1 Introduction

"There's Plenty of Room at the Bottom", Richard Feynman's famous speech in 1959,¹ is considered to be the foundation of nanotechnology. Nevertheless, Norio Taniguchi was the first to use the term "nanotechnology" in a paper published 15 years later.² Following several breakthroughs in nanoscale characterization, such as the invention of the scanning tunneling microscope and atomic force microscope in the early 80s, scientists have been able to explore nanomaterials (NMs) for a range of applications, including electronic, and biomedical applications.³

In general, NMs are structures with 100 nm or smaller in at least one dimension⁴ and are classified into four groups based on their geometrical shape: zero-dimensional materials, also known as quantum dots⁵, one-dimensional materials, such as nanofibers⁶, two-dimensional materials, such as nanosheets⁷, and three-dimensional materials such as nanogels.⁸ NMs are widely used in biomedical applications thanks to their ultra-small size and large surface area, which gives them their unique physical, chemical, and mechanical properties.⁹⁻¹⁰ As of today, some NMs being applied to a variety of nanomedicines are currently undergoing clinical trials or being marketed under FDA approval.¹¹ Even though NMs are promising for biological applications, they still exhibit some limitations, such as colloidal instability and non-specific interactions with serum proteins, which result in poor targeting in biological fluids. Moreover, nanoparticles are prone to uncontrolled biodistribution and cytotoxicity.¹² In the other words, NMs can cause unfavorable biological responses when they come into contact with body fluids and/or are implanted into live tissue due to the formed biointerfaces between biomolecules and surfaces (**Figure 1**).¹³ As a result of these shortcomings, there is a growing concern regarding the overall safety of nanomedicine, which emphasizes the importance of the development of novel nanomedicines to fall behind medical applications.¹⁴

Using polymeric materials in nanotechnology can help overcome some of these barriers and give nanomedicine a better chance to succeed. For example, biointerface interactions can be facilitated with polymeric materials, thanks to their useful properties, such as simple synthesis and functionalization,¹⁵⁻¹⁶ biocompatibility,¹⁷⁻¹⁸ and biodegradability.¹⁹⁻²⁰ Numerous polymeric NMs with diverse properties have been developed and applied as functional

biointerfacial materials for a variety of purposes, such as drug delivery,²¹⁻²⁶ pathogen inhibition,²⁷⁻³² and bioimaging.³³⁻³⁶

Research topics in this dissertation include functional polymeric materials and their interactions at biointerfaces, as well as factors affecting these interactions, including architecture, size, and surface charge. These factors are discussed in the context of two different biointerfaces applications, namely virus inhibition (**section 1.3**) and dermal delivery (**section 1.4**). However, in order to discuss these factors in greater detail, it is advantageous to review the various polymer architectures (**section 1.1**) and the diverse approaches used to synthesize them (**section 1.2**).

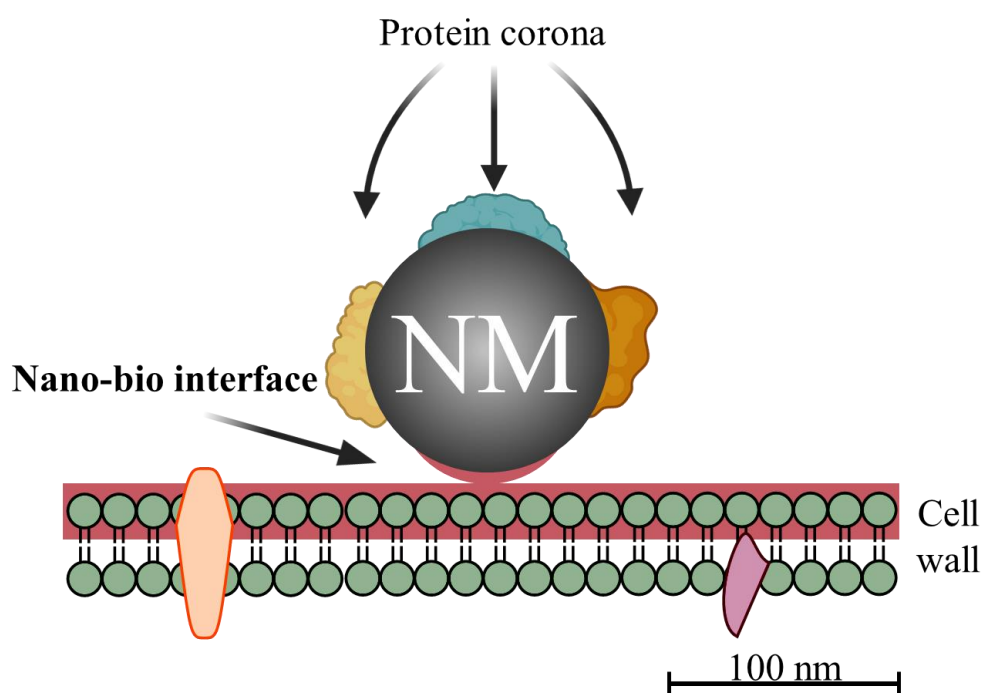


Figure 1. Illustration of the interface between a nanoparticle and a lipid bilayer.

1.1 Polymer architecture

Many studies have already addressed the role that polymer architectures play in the performance of the polymer in different applications, such as drug delivery³⁷⁻³⁸ and virus inhibition.^{27, 29} A cyclic polymer, for example, exhibits longer blood circulation times than similar linear polymers because they possess no chain ends as well as higher deformation resistance, which results in minimal renal filtration.³⁷ Therefore, the architecture of the polymer is extremely important to be considered in synthesizing novel functional polymers at biointerfaces interactions.

Polymer architectures can be divided into two different groups, namely linear and branched (**Figure 2a** and **b**). A few examples of these groups include linear block copolymers made of at least two different monomers, hyperbranched polymers, grafted polymers, dendrimers, and 2-D polymers. In addition, these types of polymers can be used to construct more complex structures, whether non-covalently (**Figure 2c**) or covalently (**Figure 2d**). The following section discusses various types of polymeric architectures.

1.1.1 Linear polymers

By linking repeating units called monomers together in a continuous length, linear polymers can be produced either by step-growth polymerization using AB or A₂ B₂ monomers or by chain-growth polymerization using an initiator to propagate a monomer (**Figure 2a**). Linear polymers can adopt different architectures in solution depending on the specific conditions such as solvent, temperature, salt concentration, and their structural features. This can be modified by the use a co-monomer, leading, for example, to alternating or diblock copolymers. These chains can further interact with each other and form non-covalent networks. A few of these noncovalent confirmations are explained in **section 1.1.3**.

1.1.2 Branched polymers

Polymers with more than two end groups and branch points are called branched polymers (**Figure 2b**). Branched polymers stand somewhere between linear polymers and polymer networks. However, it is demonstrated that their physical properties differ substantially from the other two.³⁹ Among polymer architectures that fall into this class are hyperbranched, grafted, star-shaped, and dendrimer polymers (**Figure 2b**). Here, I focus exclusively on hyperbranched polymers.

In 1952, Flory demonstrated that hyperbranched polymers can be synthesized without gelation by polycondensation of multifunctional AB_n-type monomers ($n \geq 2$).⁴⁰ Although the degree of branching is lower (0.4-0.6) than in dendrimers (1), the properties are comparable.⁴¹ It comes as no surprise that hyperbranched polymers have attracted substantial interest, as they are often considered as dendrimer alternatives and can be easily produced in one pot.⁴² One of the most intensively exploited examples of hyperbranched polymers is hyperbranched polyglycerol (hPG) which is a polyether polyol with a high number of functional hydroxyl groups. Due to its very high water-solubility, low non-specific interactions at biointerfaces, biocompatibility, and low toxicity, hPG has applications in a

instance, the *in vivo* toxicology study with hPGS amine, a 10 kDa amino-functionalized sulfated hPG, revealed a half-life of 12 days after intravenous injection.^[46]

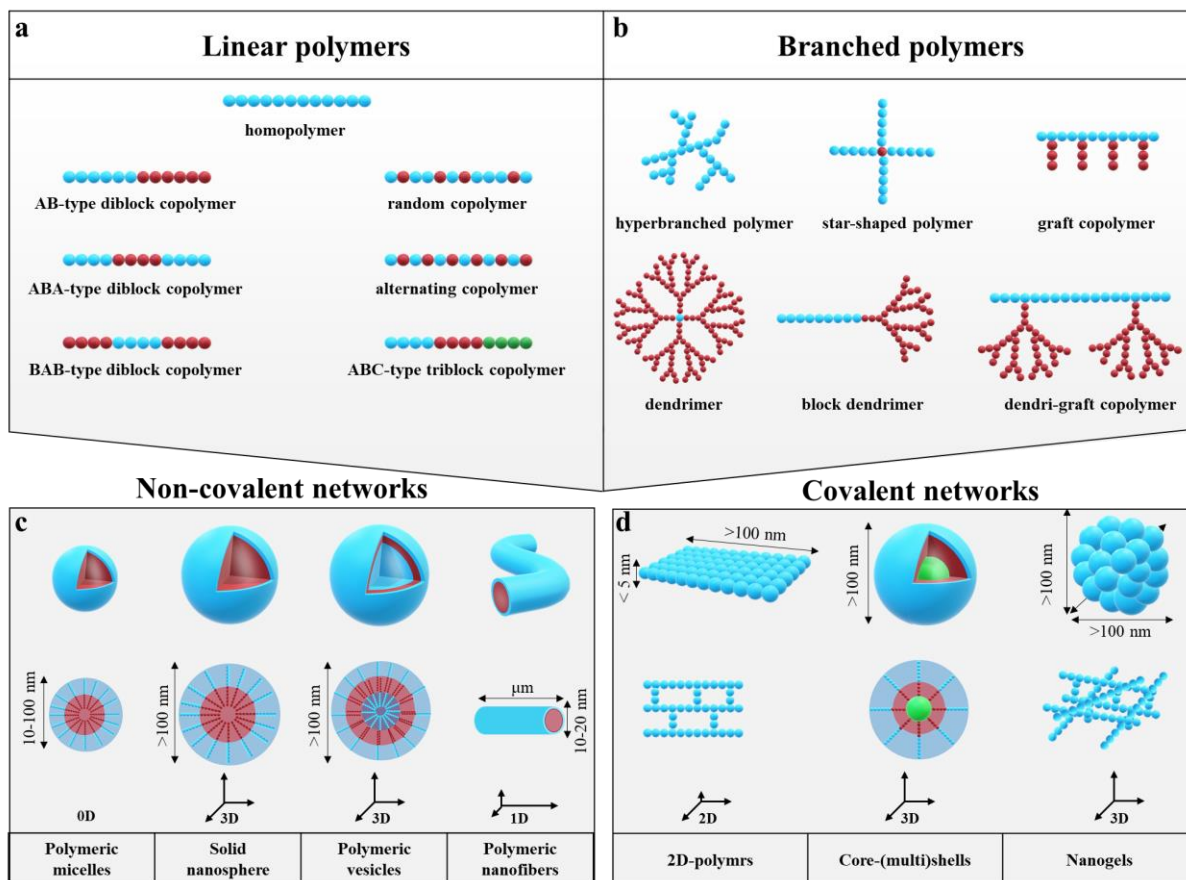


Figure 2. a) Linear polymeric architectures, b) branched polymeric architectures, c) non-covalent and d) covalent networks. Adapted from Ref. [8, 47-52]

1.1.3 Complex polymeric nanoarchitectures

In recent years, researchers have examined nanostructures made of polymer materials for their potential application in biointerfaces interactions.^[53] Many synthetic methods have been proposed to facilitate the fabrication of complex nanoscale polymeric architectures through both covalent and non-covalent interactions (**Figure 2c** and **d**).^[54] Some of the architectures from both categories are described and discussed in detail in the following two sections.

1.1.3.1 Non-covalent networks

Molecular noncovalent interactions, such as hydrophobic-hydrophobic interactions, may result in the formation of ordered aggregates/complex architectures and this phenomenon is termed self-assembly when it occurs spontaneously without external manipulation.^[55] As a

termed self-assembly when it occurs spontaneously without external manipulation.⁵⁵ As a matter of fact, self-assembly happens when forces of attraction, repulsion, and directions are in equilibrium.⁵⁶ A polymer can self-assemble under several different conditions resulting in nanostructures with diverse macromolecular architectures, including micelles, vesicles, nanofibers or solid nanoparticles (**Figure 2c**).^{50, 57} In this context, amphiphilic copolymers with appropriate hydrophobic-hydrophilic balance have the potential to autonomously self-assemble in an aqueous medium through hydrophobic effects, leading to the formation of stable nanostructures.⁵⁸ The self-assembly process generally occurs when amphiphilic polymers attain a concentration that exceeds a threshold known as the critical aggregation concentration (CAC). Recent developments in self-assembled polymers have found many uses in the biomedical field, especially for drug delivery, where they are valued for their versatility, spontaneity, scalability, and cost-effectiveness. A great deal of focus is devoted to the (dermal) delivery of drugs *via* micelles.⁵⁹⁻⁶⁰ In the case of dermal drug delivery, polymeric micelles may enhance the delivery of their intact cargos, but this mechanism is not well understood. There have been several reports suggesting that polymeric micelles can pass through the skin while carrying their cargo intact.⁶¹ According to another perspective, the micelles disassemble upon contact with the skin, and each polymer chain transfers therapeutic molecules. The latter approach led to the development of stable micelles, such as a core-crosslinking method and core-multi-shell nanoparticles.⁶²

1.1.3.2 Covalent networks

2D polymers

In recent years, synthetic 2D nanomaterials (2DN) have drawn considerable interest owing to their tunable physical and chemical properties.⁶³⁻⁶⁶ 2DNs are nanoscale compounds with a sheet-like structure, but with a thickness smaller than 5 nm and a lateral size greater than 100 nm.⁵² As of now, various rigid and soft 2DNs have been explored, including hexagonal boron nitride,⁶⁷ metal-organic frameworks (MOF),⁶⁸ covalent organic frameworks (COF),⁶⁹ polymers,⁷⁰ black phosphorus (BP)⁷¹, and graphene.⁷² In a literature review that includes publications until 2015, it appears that a great deal of interest exists in investigating the potential applications of 2D nanomaterials, such as drug delivery, biosensors, tissue engineering, cancer therapy, and bioimaging (**Figure 3**).⁷³ Nevertheless, concerns remain about the cytotoxicity of 2DNs, environmental hazards, and nonspecific interactions at

biointerfaces in biomedical applications, leading researchers to investigate how to address these issues.⁷⁴⁻⁷⁵

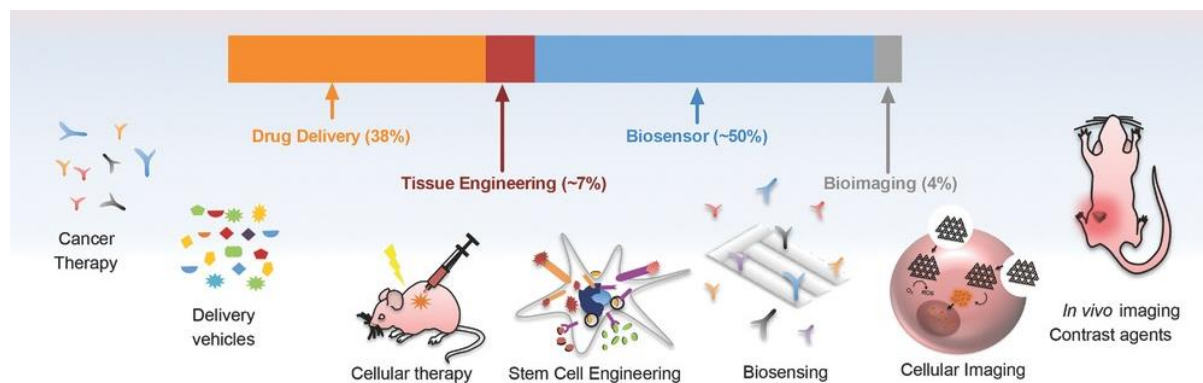


Figure 3. Research trends associated with 2DNs and some of their potential biomedical applications. Reprinted with permission from Ref. [73]. Copyright 2015 John Wiley and Sons.

To synthesize new 2DNs for use in biomedical applications, a deep understanding of their synthesis process and reaction conditions is crucial. There are numerous templates assisted synthetic techniques that are known for their ability to accurately generate a broad array of 2DNs. These include dip-pen lithography, photolithography, and vat photopolymerization.⁷⁶⁻⁷⁷ Although these approaches are effective, they are often not feasible for large scale production of 2DNs. Colloidal templates, on the other hand, allow for the synthesis of 2DNs in a convenient, scalable, and efficient manner.⁷⁸⁻⁷⁹ Typically, this method involves covalent and noncovalent interactions of the template surface with monomers. Regarding noncovalent interaction, monomers are stabilized on the template and monomers' mobility facilitate self-rearrangement during polymerization.⁸⁰⁻⁸¹ However, the monomers can detach from the template, which will result in defects or cracks, as well as side products.⁸²⁻⁸³ This means that the template-monomer interaction must be stronger than that of the solvent-monomer, thereby restricting the use of colloidal templates in on-surface reactions. The approach of attaching monomers covalently on a template surface was thereby considered, which has been less investigated. Thanks to the strong covalent bond between monomers and the template, side reactions are reduced in this method, resulting in more precise products containing fewer impurities. This method is especially useful for functional (macro) molecules, since embedding them on templates is challenging. When using the covalent approach, the pivotal point is the binding of monomers to the template by readily cleavable bonds, thus enabling the 2DNs to be later separated from the template by external forces.

3D polymers (Nanogels)

Polymers with three-dimensional (3D) architectures, which are composed of pure polymers or polymer composites with interconnected networks and continuous pores, have a variety of potential applications.⁸⁴ For example, polymeric nanogels consist of cross-linked hydrogel particles with 3D networks provide improved stability and efficiency as a scaffold in the development of effective virus entry inhibitors. Nanogels are typically water-swollen particles and fabricated by either polymerization in homo-/heterogeneous phases (e.g., inverse nanoprecipitation or macro/mini-emulsion polymerization), or by using template-assisted techniques such as nanolithography. In addition, the cross-linking of polymers, for instance using a telechelic cross-linker, and their self-assembly by physical interaction may also result in nanogels.⁸⁵ However, the latter one is a non-covalent network. In addition to the high-water content, nanogels are soft, biocompatible, and have exceptional dispersibility in aqueous media. These materials have the ability to encapsulate biologically active substances, as well as being broken down into smaller pieces, which can then be eliminated from the body by the kidneys. Due to these intrinsic properties, nanogels have found considerable application in the biomedical fields such as the (dermal) delivery of drugs, proteins, and genes, bioimaging, and the inhibition of virus entry.^{8, 86-87}

1.2 Synthesis of well-defined complex polymeric architectures

To achieve well-defined complex architectures, it is necessary to precisely control the molecular structure of the building blocks. In general, synthetic polymers are synthesized either by the chain-growth or step-growth polymerization method. However, these methods yield polymers with high polydispersity. In order to address this, several polymerization methods have been devised, including living step-growth polymerization, ionic living polymerization, ring-opening polymerization (ROP), atom-transfer radical polymerization (ATRP), nitroxide-mediated polymerization (NMP), reversible addition–fragmentation chain-transfer polymerization (RAFT), and multistep-growth techniques. **Figure 4** provides an overview of the main polymer synthesis approaches.

1.2.1 Chain growth approach

1.2.1.1 Ring-opening polymerization (ROP)

ROP is a living chain-growth polymerization method in which cyclic monomers are attacked

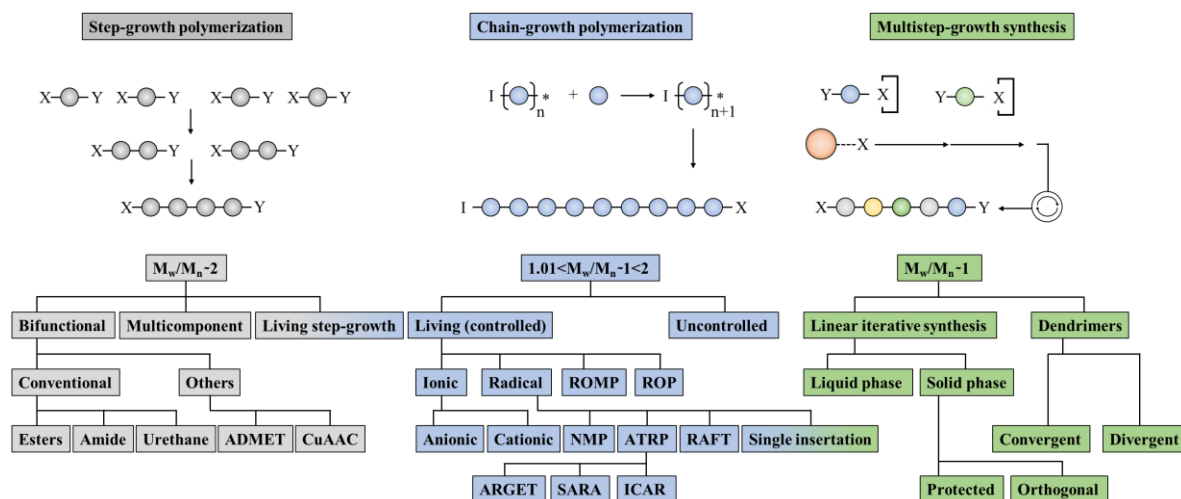


Figure 4. An overview of the main polymer synthesis approaches. M_w/M_n = polydispersity index (PDI). Adapted with permission from Ref.[88]. Copyright 2016 Springer Nature.

by the polymer chain to form a longer chain. Depending on the initiation reaction, the reactive site can be radical, anionic, or cationic (**Figure 5**). The method can also be conducted by using metal catalysts, namely ring-opening metathesis polymerization (ROMP) and coordination-insertion polymerization. The advancement of the metathesis method in organic synthesis by Chauvin, Grubbs, and Schrock was acknowledged with the Nobel Prize in chemistry in 2005. Metathesis polymerization of olefin is an implementation of metathesis reactions to polymer synthesis, which includes ROMP and acyclic diene metathesis polycondensation (ADMET). Norbornene, for example, can be polymerized through ROMP.⁸⁹ Ring-opening in a cyclic monomer is primarily driven by bond-angle strain and steric repulsion between atoms in the center, leading to negative enthalpy change. Three and four-membered rings are most affected by relief of bond-angle strain, whereas eight to eleven-membered rings are more affected by steric crowding relief. Five-, six-, and seven-membered rings have a smaller enthalpic effect, and polymerizing these rings is thus more difficult.⁹⁰

Some cyclic monomers like cyclic esters (e.g., β -propiolactone, ϵ -caprolactone, and L,L-lactide), cyclic ethers (e.g., ethylene oxide, propylene oxide, and tetrahydrofuran), or *N*-carboxy anhydrides (NCA) (e.g., Lysine(Z)-NCA and γ -Benzyl Glutamate NCA) can be polymerized resulting in high-molecular-weight polymers by using this method. Herein, two important ROP processes will be discussed in-depth, anionic ring-opening polymerization (AROP) and NCA polymerization.

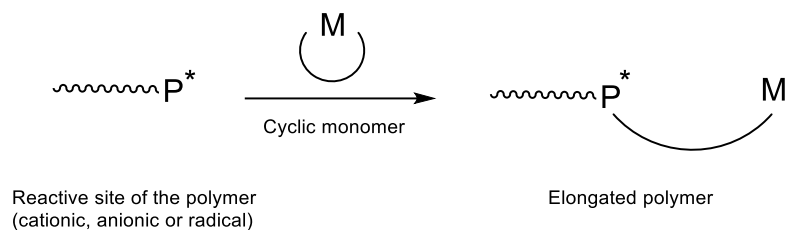


Figure 5. General scheme of ROP method. Redrawn with permission from Ref. [91]. Copyright 2016 Elsevier.

1.2.1.2 Anionic ring-opening polymerization (AROP)

A typical AROP reaction is initiated by nucleophilic reagents such as organometals, alkoxides, phosphines, amines or alcohols. AROP is commonly performed on cyclic compounds with high electrophilicity, for example, ester, carbonate, amide, urethane and phosphate. However, monomers with three-membered ring structures can still undergo AROP, even if they lack electrophilic functions like those of ether, amine, or thioether.⁹²

General mechanism of AROP

Cyclic monomers usually have polarized functional groups symbolized by X-Y, in which X (in most cases carbon) is electron-poor because of the atom Y that is strongly electron-withdrawing (e.g., oxygen, nitrogen, sulfur, etc.). The ring is then opened *via* a nucleophilic attack on the atom X by the initiator, which releases Y⁻. Nucleophilic species generated in the first step will then attack atom X in another monomer, and as this process is repeated multiple times, the corresponding polymer is produced.⁹² A general mechanism for AROP reaction is presented in **Figure 6**. During anionic ROP, propagating chain ends normally attack monomers nucleophilically. Alternatively, an acidic proton of a monomer may be deprotonated, resulting in an anionic monomer that can act as an initiator and nucleophilic attack another monomer. This mechanism is called 'activated monomer mechanism' and is explained in detail in the NCA polymerization section.

Architectures obtained from AROP

A variety of polymeric architectures can be developed using AROP, ranging from linear polymers to branched polymers to polymeric networks. hPG, for example, can be synthesized using an alkoxide, such as 1,1,1-tris (hydroxymethyl) propane (TMP), to serve as an initiator of glycidol *via* AROP (**Figure 7a**).⁹³ By protecting the hydroxyl function of the monomer

prior to polymerization, linear polyglycerol (LPG) can be obtained through AROP (**Figure 7b**).⁹⁴

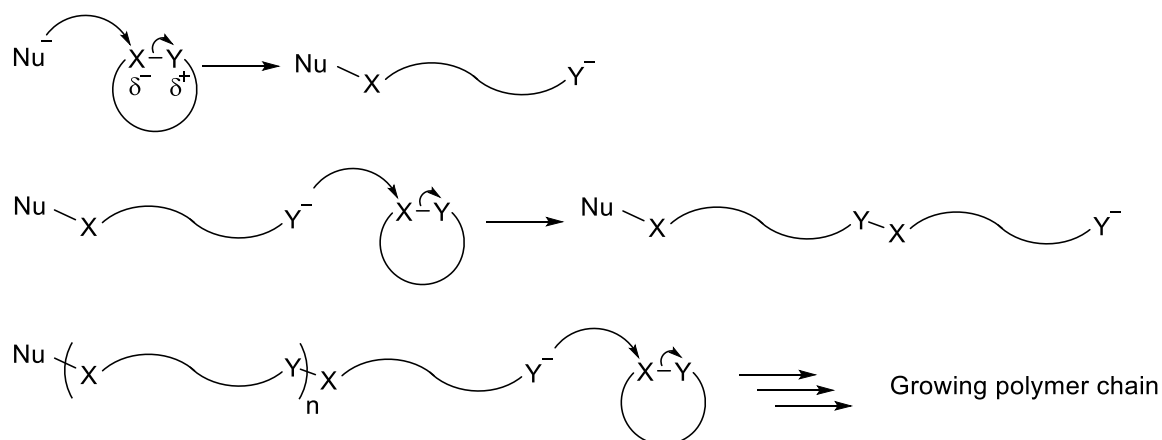


Figure 6. General mechanism for AROP. Adapted from Ref. [95].

AROP can also be combined with other techniques to produce more complex structures. For example, one can produce precise structures of clickable precursors using AROP and thereby produce a variety of polymeric architectures *via* intramolecular click reactions. Sisson *et al.*⁹⁶ prepared hPG based nanogels by combining AROP bio-orthogonal click reactions. They synthesized two hPG molecules bearing click moieties through AROP. These materials have been used as macromonomers for strain-promoted azide-alkyne cycloaddition reactions, which result in nanogels (**Figure 7c**).

1.2.1.3 NCA Polymerization

Another example of cyclic monomers undergoing ROP is amino acid-derived *N*-carboxyanhydrides (NCA). The discovery of α -amino acid NCA and the recognition of Staudinger's theory of covalent macromolecules in the 1920s opened doors for synthesizing polypeptides derived from α -amino acid NCA, which were extensively studied by many different research groups.⁹⁷

Synthesis of α -amino acid NCA

NCA monomers were first synthesized by Leuchs a century ago⁹⁸ and because it remains of interest, other researchers have worked on modifying and developing new synthetic methods (**Figure 8**). Synthesis of NCA monomers by Leuchs method involves reacting the *N*-carbamoyl-amino acids with thionyl chloride. The reaction was modified by Wessely *et al.*⁹⁹ in 1950 by using acetyl chloride and acetic anhydride to obtain higher yields.

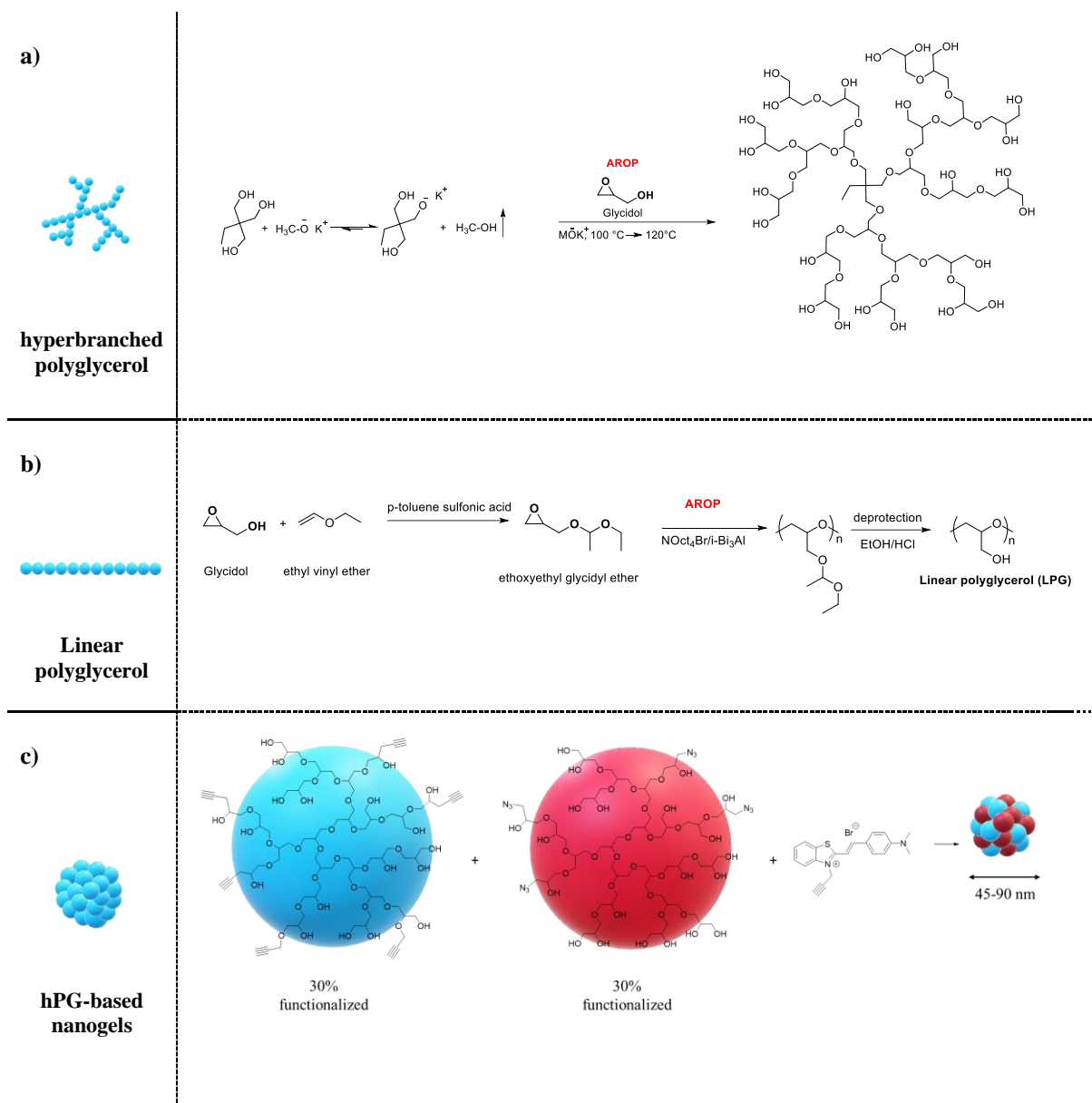


Figure 7. Diverse polymer architectures obtained from ROP. a) hyperbranched polyglycerol (hPG), b) linear polyglycerol (LPG), and c) hPG based hydrogels. Part a adopted from Ref. [93]. Part b adopted from Ref. [94]. Part c adopted from Ref. [96].

In 1958, Katachalski & Sela^[100] used phosphorous tribromide as a chlorinating agent with higher activity and found that the reaction temperature and, consequently, the decomposition of the monomer was decreased. In 1950, Farthing^[101] developed a more direct method of synthesizing NCA monomer by using phosgene. This is the most commonly used method since the NCA monomer can be easily obtained with a good yield and without racemization. Due to high toxicity of phosgene, a less dangerous version of this technique has been developed by using other phosgene derivatives such as diphosgene^[102] and triphosgene.^[103] Moreover, numerous studies have been made to fully eliminate the use of

toxic phosgene derivatives when synthesizing NCA amino acids. In 2007, Endo *et al.*¹⁰⁴ developed a phosgene-free method for synthesizing NCA monomers using bisarylcarbonates having electron-withdrawing substituents (**Figure 8**).

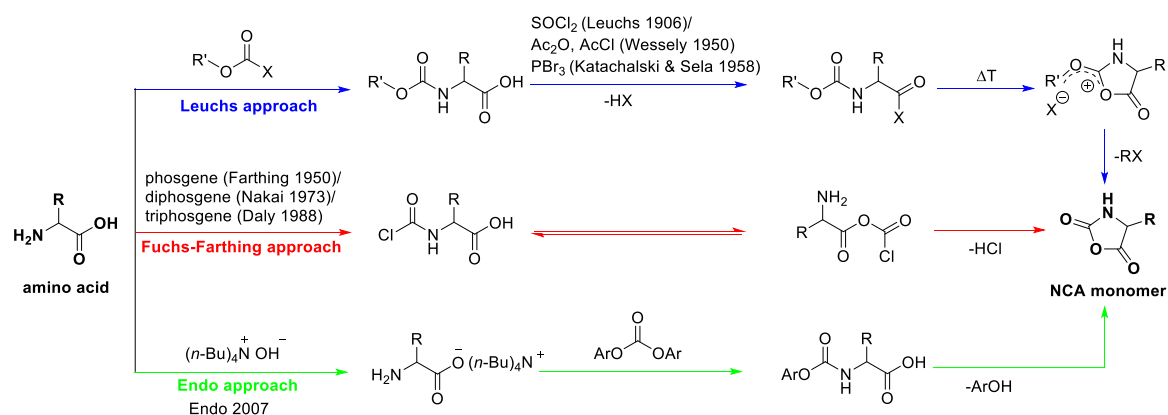


Figure 8. Pathways for the synthesis of NCA monomers.

ROP of NCA monomer

Polypeptides, also known as poly(l-amino acids), are commonly synthesized by ROP of NCA monomers derived from α -amino acid. ROP of amino acid NCAs is often triggered by nucleophiles like primary amines,¹⁰⁵ tertiary amines,¹⁰⁶ thiols,¹⁰⁷ alcohols,¹⁰⁸ or transition metal complexes.¹⁰⁹ In the NCA polymerization, the monomer is traditionally initiated by an amine, and, based on the monomer and the conditions of the polymerization, there are two possible polymerization pathways: normal amine (NA) and activated monomer (AM) mechanisms (**Figure 9a** and **9b**).¹⁰⁶ The NA mechanism of polymer synthesis involves nucleophilic ring-opening, with polymerization occurring linearly upon monomer conversion in the absence of side reactions (**Figure 9a**). Despite this, the AM mechanism is initiated by a deprotonated monomer of NCA, which functions as the nucleophile (**Figure 9b**). Thus, the initiators that have higher basicity and therefore lower nucleophilicity, such as tertiary amines, result in AM, and those that have lower basicity and therefore higher nucleophilicity, such as aliphatic primary amines, result in NA mechanism.¹⁰⁶ The polymerization of any given system, however, can switch between AM and NA mechanisms at any time. Thus, as one mechanism advances, the other one may intervene and result in undesirable side reactions.¹¹⁰ Many methods have been developed to suppress AM, including Deming's transition-metal catalysts¹¹¹⁻¹¹² and Schlaad's ammonium-mediated NCA polymerization (**Figure 9c**).^{106, 113}

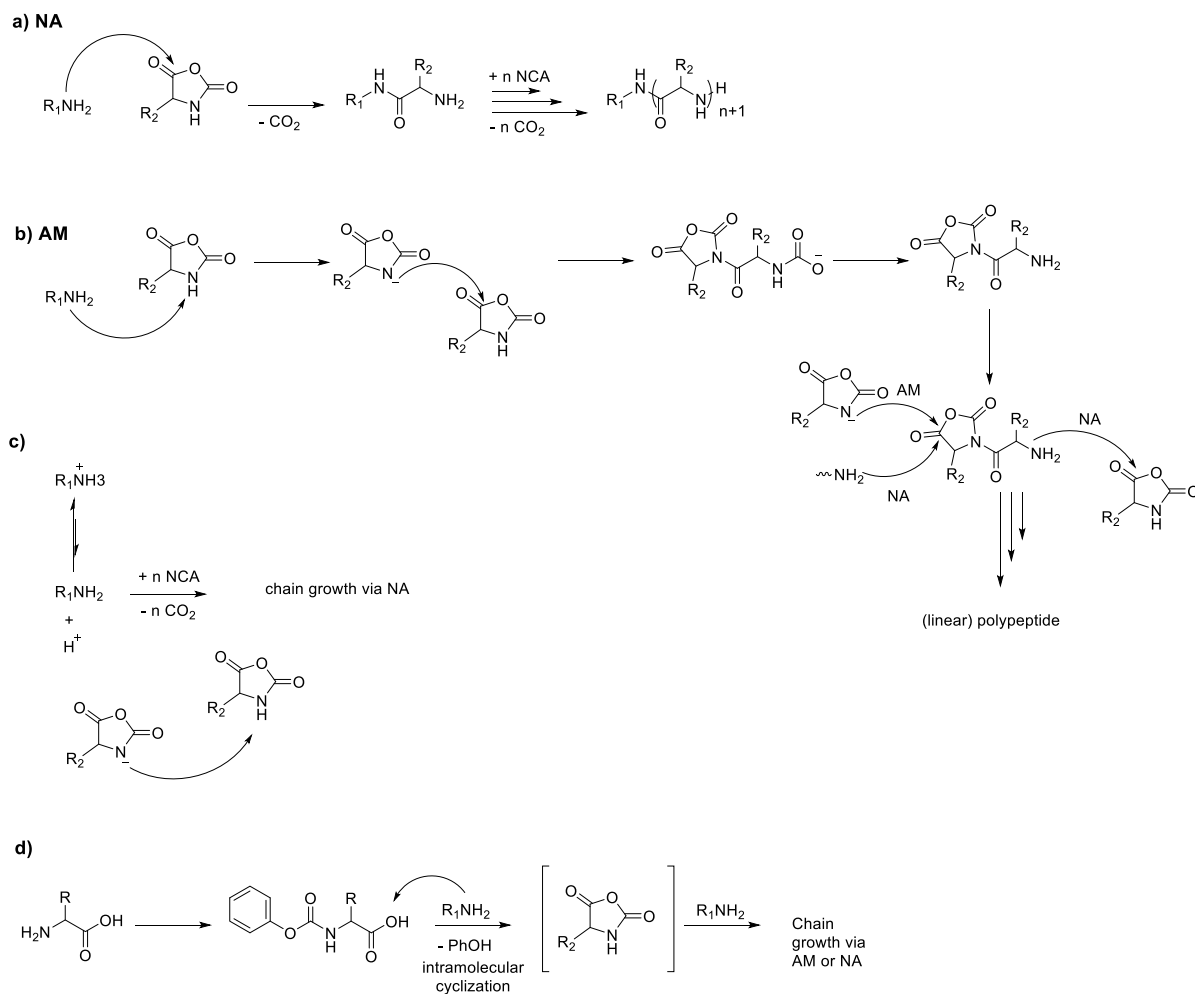


Figure 9. a) Normal amine (NA), b) activated monomer (MA) mechanism, c) proposed mechanism for the ammonium-mediated ring-opening polymerization of NCA, and d) Mechanism of synthesis of polypeptides from *N*-aryloxycarbonyl amino acids. Scheme 2a-c adopted from Ref. [113] and scheme 2d adopted from Ref. [114].

As previously mentioned, Endo developed a way to synthesize monomers without using phosgene. Later, he developed this method further to synthesize polypeptides without isolation of the NCA monomer (**Figure 9d**). In this way, the activated urethane derivatives of amino acids can be polymerized with or without using a nucleophile and accompanied by *in situ* formation of NCA amino acids as a result of chain-growth polycondensation.¹¹⁵⁻¹¹⁷ The process involves neither the use of toxic chemicals nor the isolation of NCAs, which is a very challenging process.

Architectures obtained from NCA polymerization

NCA polymerization can be used by itself or in combination with other polymerization methods to synthesize various polymer architectures. These architectures can be approached

either in a one-pot method (**Figure 10a** and **10d**) or as a multi-step method (**Figure 10b** and **10c**). A block-copolyptide can, for example, be made by conjugating polypeptide segments or with a macroinitiator (first block) for initiating an NCA monomer (second block), or by sequentially adding monomers after the previous one is fully consumed (converted). There are also other strategies for synthesizing an amphiphilic block-copolymer. For instance, two monomers were mixed in one pot to synthesize p(Lys-*b*-Leucine).¹¹⁸ In this study, Lys(Z)-NCA and *N*-thiocarboxyanhydride (NTA) of leucine were used. It was observed that when Lys(Z)-NCA is consumed then Leu-NTA start to propagate to form a block-copolyptide, reflecting NCA's higher reactivity than NTA's. Endo's method was also found to be useful in combination with other polymerization methods to produce block copolymers. In a study, Endo *et al.*¹¹⁹ combined living cationic polymerization of oxazoline with chain-growth polycondensation of activated urethane derivatives of α -amino acids such as l-Lys(z), l-Alanine, l-Phenylalanine, and l-Serine(Bz) in order to synthesize poly(2-ethyl-2-oxazoline)-*b*-polypeptide. Poly(2-ethyl-2-oxazoline), thanks to its terminal amine, acts as a macro-initiator in the chain-growth polymerization of activated urethane derivatives of amino acids. The discussion above was mostly aimed at different types of initiators, including (multi)functional initiators and (multi)functional micro-initiators. However, the type of monomer also determines the architecture, especially in the case of noncovalent architectures. A good example is ionic amphiphilic co-polypeptides, which have both ionic and hydrophobic properties that enable them to self-assemble into a wide variety of nanostructures. The most commonly used poly(l-amino acids) which are water-soluble and provide ionic charges are poly(l-lysine), poly(l-aspartic acid), and poly(l-glutamic acid). In contrast, poly(l-phenylalanine) and poly(l-leucine) are two examples of hydrophobic segments used in this class of copolymer. Ionic amphiphilic polypeptides can self-assemble into vesicles, polymersomes, micelles, and solid polymer particles by manipulating the hydrophobic/hydrophilic ratios, degree of polymerization, and ionic strength. An amphiphilic polymer of glutamic acid and phenylalanine was synthesized which self-assembled into polymersomes in water.¹²⁰ This polymersomes could range in size from 60 to 350 nm with varying the pH of the solution and the length of the hydrophobic blocks. In another study, poly(butadiene)-*b*-poly(l-lysine) was synthesized and found that the architecture of this amphiphilic block copolyptide can be altered from spherical to rodlike micelles by changing the pH value of the solution from 2 to 9.¹²¹ These polymers have an ionic character, which makes them suitable for controlled drug release.

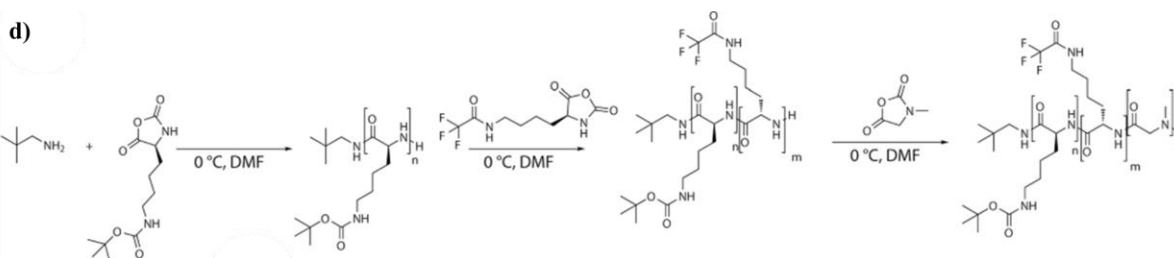
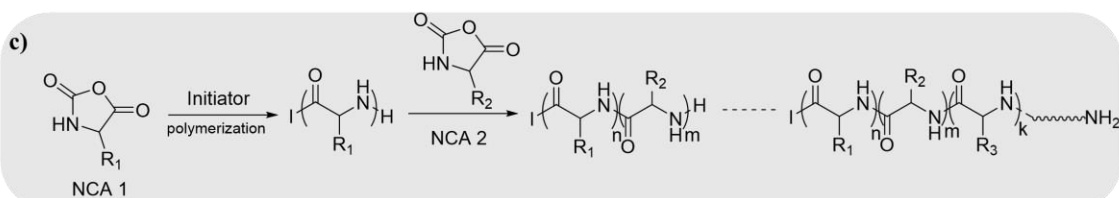
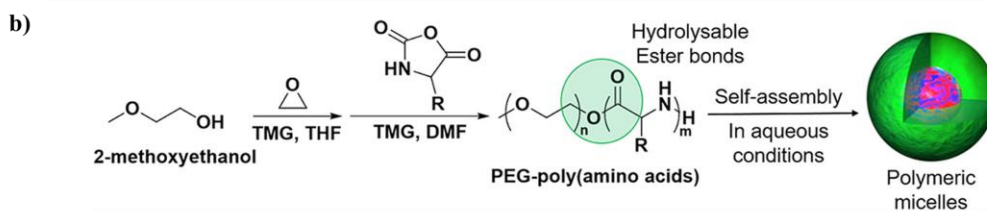
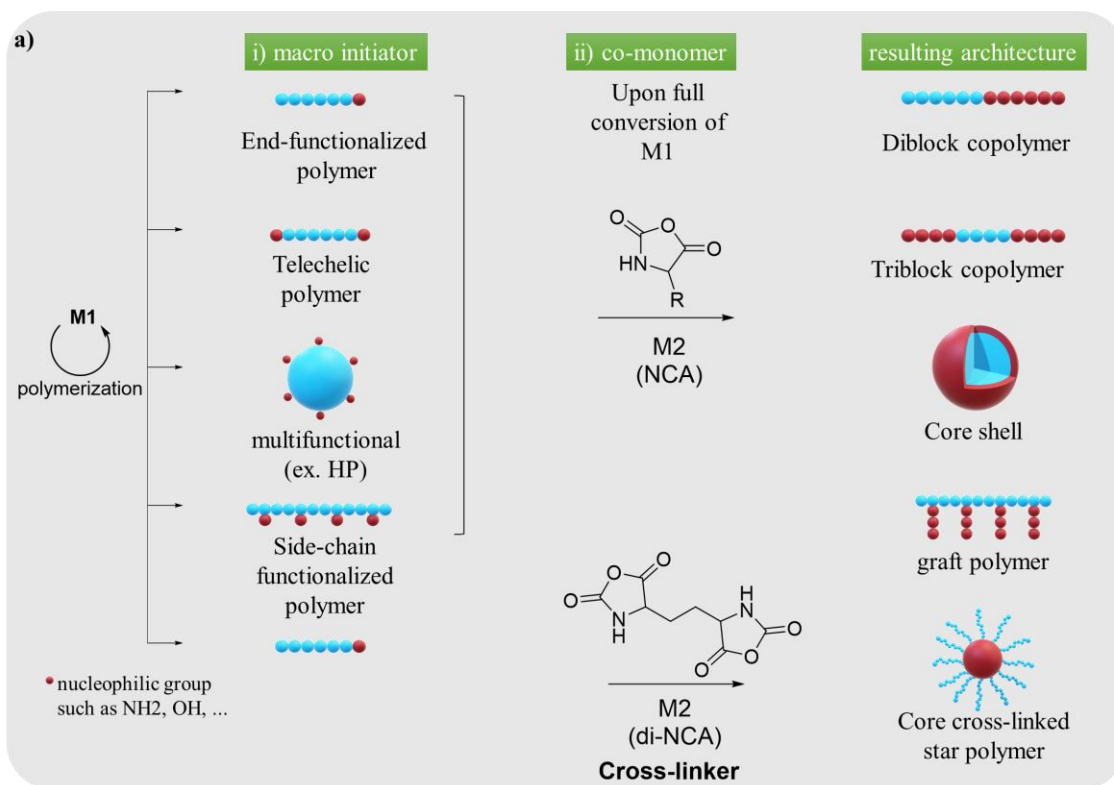


Figure 10. Representation of potential polymeric architectures obtained from a and b) one-pot and c and d) sequential NCA polymerization approach. c) One-Pot Synthesis approach to synthesis PEG-polyamino acid diblock copolymer. d) Synthesis of PLys(Boc)-PLys(TFA)-PSar triblock copolymers by sequential NCA polymerization. Part a partially adapted from Ref. [122]. Part b reprinted with permission from Ref. [123]. Copyright 2019 American Chemical Society. Part d reprinted with permission from Ref. [124]. Copyright 2014 John Wiley and Sons.

At physiological pH levels, *i.e.*, pH 7.4, the loaded drugs are retained in the polymer; at lower pH levels, they are rapidly released. Polymers with this property are advantageous for serving as smart drug carriers, for example, to target tumors.¹²⁵

1.2.2 Step-growth approach

The step-growth approach, also known as polyaddition, is often used in classical polymerizations, such as polyamide polymerization, in which bifunctional or multifunctional monomers react at first to form dimers, trimers, then oligomers, and finally polymers. One can obtain different architectures based on the functional groups in monomers, *i.e.*, monomers with bifunctional or multifunctional groups lead to linear and branched polymers, respectively. However, a large extent of reactions is required to obtain a high molecular weight. Despite this, there is still progress being made in developing step-growth techniques to synthesize polymers with precise architectures, such as azide-alkyne cycloaddition.

1.2.2.1 Azide–alkyne click chemistry

In 1963, Rolf Huisgen¹²⁶ introduced the concept of 1,3-dipolar cycloadditions that result in five-membered heterocycles. In Huisgen's 1,3-dipolar cycloaddition between an azide and alkyne at 100°C, a mixture of 1,4- and 1,5 disubstituted triazoles are formed (**Figure 11a**). On the other hand, Sharpless *et al.*¹²⁷ introduced the concept of “click chemistry” in 2001 to describe reactions which are modular, wide-ranging, give high yields, do not generate toxic byproducts, can be purified by nonchromatographic methods, and are stereospecific without solvents or in benign solvents. In their definition, Huisgen's 1,3-dipolar cycloaddition falls into this category. However, due to high temperature, slow reaction kinetics, and mixtures of regioisomers, this reaction had limited application in biomedical applications. Sharpless *et al.*¹²⁸ and Meldal *et al.*¹²⁹ independently discovered copper-catalyzed azide-alkyne cycloadditions (CuAAC), yielding only the 1,4-regioisomer (**Figure 11b**). In a follow-up study, Jia *et al.*¹³⁰ found that azide-alkyne cycloadditions using a ruthenium(ii) catalyst yield only the 1,5 isomer (**Figure 11c**). Polymer scientists began using click chemistry to produce macromolecules with defined architectures.¹³¹ The following examples illustrate how azide-alkyne click chemistry can be used to prepare well-defined polymer architectures.

1.2.2.2 Architectures obtained from Azide–alkyne click chemistry

Click chemistry can be utilized in the procedure of synthesizing polymers resulting in 1,2,3-triazoles from bifunctional alkyne and azide monomers *via* step-growth polymerization.¹³²

However, it was found that this technique leads to undefined structures. Therefore, it was suggested that the click chemistry should be combined with other polymerization techniques such as living radical polymerization to achieve well-defined structures.¹³³ Consequently, it is necessary to construct polymers with alkyne and azide functionalities at either the end of the chains or along their backbone.¹³⁴⁻¹³⁵ **Figure 7c** provides an example of how to make hydrogels using Click chemistry and AROP. Here is a discussion on how this valuable tool can be used in combination with other polymerization methods to generate more complex

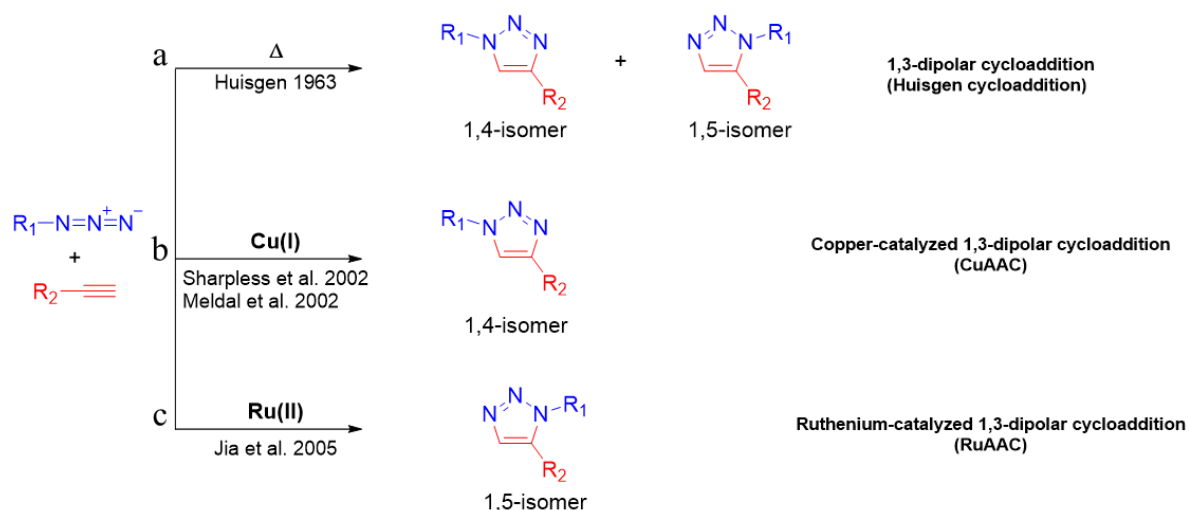


Figure 11. 1,3-dipolar cycloadditions between alkynes and azides giving a) the mixture of regioisomers without catalysis, b) the 1,4-regioisomer of 1,2,3-triazole in presence of Cu(i), c) the 1,5-regioisomer of 1,2,3-triazole in presence of Ru(ii).

polymer architectures that are hard or impractical to fabricate by conventional polymerization methods. For example, ATRP which is a metal catalyzed radical polymerization, has turned out to be highly effective in this case. Since polymers derived using this method can be readily exchanged into azide by using sodium azide. For instance, Gao and Matyjaszewski¹³⁶ prepared star-shaped polymers by combining ATRP with click-CuAAC. Polystyrene (PS) was prepared by ATRP followed by the treatment with sodium azide in order to obtain azido-terminated PS ($PS-N_3$). $PS-N_3$ and multifunctional compounds containing alkyne were coupled to produce three- and four-arm star polymers with yields of 83 and 90%, respectively, within 3 h.¹³⁶ Garyson and Laurent¹³⁷ synthesized polystyrene macrocycles effectively by combining ATRP and click reaction. Using an initiator with alkyne functionality, they were able to click cycle polymer chains after switching their end groups from bromo to azide. Another attempt was made to synthesize PEG-peptide hydrogels, cross-linked networks, with well-defined structures for use in cell delivery by using the CuAAC click reaction. In this study, tetra acetylene PEG and peptide diazide or PEG diazide or their

mixture, were employed to synthesize RGD-containing hydrogels by Click chemistry with high efficiency.¹³⁸ There have been excellent reviews of some of the more advanced polymer architectures reported using click and polymer chemistry.^{133-134, 139-142}

1.2.3 Multistep-growth approach

For the preparation of specific monodisperse polymers with precise structures, known as sequence-defined polymers, like peptides and dendrimers, it is necessary to use multiple steps.¹⁴³ This approach, which is known as multi-step-growth synthesis, was initially developed for synthesizing peptides using solid phase peptide synthesis (SPSS) method. Recent research has demonstrated that the principles of this "bio-inspired" procedure can be used in a variety of novel synthesis methods, including high molecular weight dendrimers,¹⁴⁴ as well as novel orthogonal techniques without requiring main-chain protective groups.¹⁴⁵

So far some of the most prominent polymeric architectures that can be used in biointerface interactions have been reviewed, with a particular emphasis on the methods that can be utilized to develop them. Within the next two chapters (**1.3** and **1.4**), two noteworthy applications will be explored in greater detail: antiviral polymers and polymeric nanocarriers for dermal drug delivery. Several parameters will also be discussed that should be considered when designing polymer-based architectures for these specific applications.

1.3 Antiviral polymers

The global COVID-19 pandemic that continues to ravage the world has raised an enormous awareness towards suppressing the spread of viruses. Furthermore, it takes several years to develop safe vaccines through classic methods of production and clinical trials. It is therefore vital that broad-spectrum antiviral drugs are available before the next pandemic so that vaccines can be developed in time.¹⁴⁶ Before developing antiviral drugs that block viruses effectively, one must know the mechanism of viral infection and replication. In spite of the wide variety of viruses that exist, viruses generally replicate in the following ways (**Figure 12**)¹⁴⁷ : at the onset of an infection, the virus attaches *via* the interaction of its surface protein with the cell surface and cell surface receptors. The virus or its nucleic acid genome then invades the cytoplasm. Following this, the genome is released from its protective capsid and enters the nucleus of the cell (most DNA viruses) or is transcribed in the cytoplasm (most RNA viruses) and leads to protein synthesis. Upon replication, the newly synthesized viral

genomes and their structural proteins are assembled into new virions and that are released from the cell. Antiviral drugs are meant to inhibit one or multiple of these steps to break the cycle of infection.¹⁴⁸

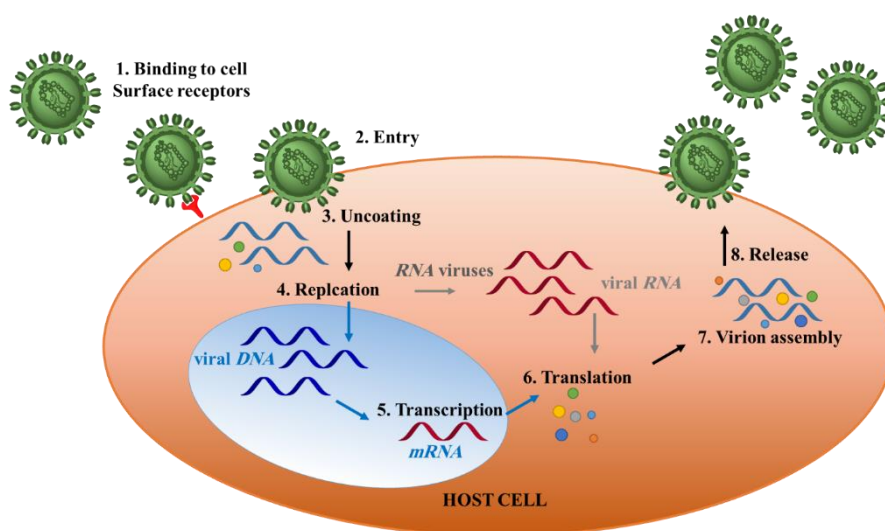


Figure 12. Schematic representation of the cycle of a virus's infection in the host cell. Adopted from Ref. [149].

There are two types of approaches for developing antiviral drugs which operate intra- or extracellularly. Intracellular antiviral drugs are typically small molecules that are designed to treat a specific process of the viral replication within a cell. Due to the differences in how viruses replicate, it is unlikely to develop a comprehensive drug with this intracellular approach and it is likely that a drug needs to be redesigned whenever a new virus emerges. On the other hand, extracellular antivirals are of relevance since they have the capability of being broad spectrum by targeting a universal process of the infection cycle. Extracellular antivirals can be classified as entry inhibitors, which bind to the virus surface and prevent viral-cell interactions, and invasion of the virus into the cell. The entry inhibitors are designed to mimic the specific receptors that may be used by viruses to bind to cells. The fact that different viruses can use similar or even identical initial attachment structures, such as heparan sulfate, or receptors on the surface of cells explains why extracellular antivirals are more likely to be broad-spectrum.¹⁵⁰

To date, however, only a handful of antiviral drugs have been tested for the treatment of viruses that can cause human infection,¹⁵¹ and the majority have either limited effectiveness, as with acyclovir, which is frequently administered for Herpes simplex virus type-1 (HSV-1),¹⁵² or are associated with severe side effects. These issues can be addressed

using polymers. It is possible to use them either as antiviral drug carriers to decrease the toxicity of a drug as well as to prolong the duration of drug circulation within the body or as materials that themselves possess antiviral activity.¹⁵³ The latter type, also known as antiviral polymers, is the subject of this section. Furthermore, antiviral polymers may contain metal particles and/or ions as well as moieties having antiviral properties, such as amines, ions moieties, carboxylic acids, sulfates, or phenol.¹⁵⁴

Many factors are involved in pathogen inhibitor effectiveness, such as inhibitor architecture, size, surface charge, hydrophobicity, and ligand distribution. **Section 1.3.3** will cover the most important of these; however, prior to that, the infection cycles of two viruses, HSV-1 and severe acute respiratory syndrome coronavirus 2 (SARS-CoV-2), will be explored, which is very important to understand before designing an antiviral agent.

1.3.1 Herpesvirus

Shedding light on the family of herpesviruses, one can find more than 100 viruses that can affect different species.¹⁵⁵ Humans are known to be at risk from eight of these viruses, including the HSV-1 and HSV-2.¹⁵⁵ The virus is composed of an icosahedral capsid enclosed in a membrane envelope and has an overall diameter of approximately 200 nm.¹⁵⁶ HSV-1 infections are prevalent around the world and affect about 70-90% of all adults.¹⁵⁷ Despite being well studied, this infection remains a serious public health concern since there is no vaccine against it, and existing treatments such as prescribing acyclovir show poor effectiveness.¹⁵² Heparan sulfate resides on host cell surfaces and facilitates entry of HSV-1 into the cell through electrostatic interaction with positively charged regions of the viral envelope glycoproteins B (gB) and C (gC) (**Figure 13 a**).¹⁵⁸

1.3.2 Coronavirus

The coronavirus (CoV) family is a group of enveloped, positive-sense, and single-stranded RNA viruses that vary in size from 60-140 nm and appear to have spikelike projections on their surface; hence it is called coronavirus.¹⁵⁹⁻¹⁶⁰ The viruses of this family can cause respiratory, enteric, hepatic, and neurological diseases in humans and animals.¹⁵⁹ SARS-CoV and MERS-CoV (the Middle East respiratory syndrome CoV) are two new CoVs which have caused severe human diseases in recent decades with a mortality rate of 10 and 35%, respectively.¹⁶¹ In late December 2019, SARS-CoV-2 emerged as the seventh virus affecting humans, causing a global pandemic unprecedented in history.¹⁶²

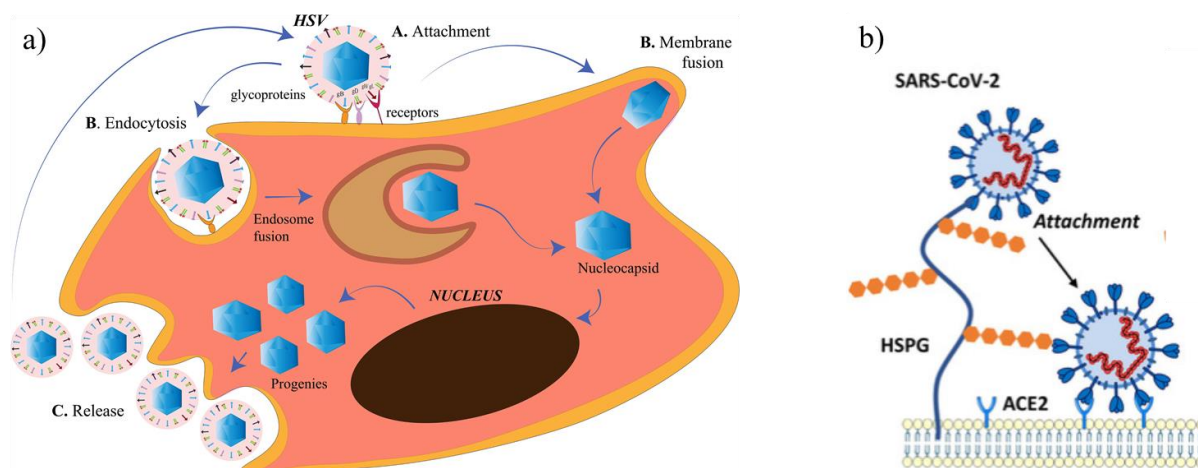


Figure 13. Lifecycle of a) HSV-1. b) Attachment of SARS-CoV-2 to surface-exposed heparan sulfate facilitates virus entry. SARS-CoV-2. Part a: this is an unofficial adaptation of an open-access article appeared in *Frontiers in Microbiology*¹⁶³. Part b reprinted with permission from Ref.[164] . Copyright 2021 John Wiley and Sons.

The four structural proteins of CoVs are spike (S), envelope (E), membrane (M), and nucleoprotein (N). It is the S protein found on the surface of CoVs that performs a significant task during virus invasion. This protein contains two subdomains, the S1 and S2, which are respectively involved in receptor binding and cell membrane fusion.¹⁶⁵ Formerly, angiotensin-converting enzyme 2 (ACE2) was recognized as the receptor for SARS-CoV,¹⁶⁶ and SARS-CoV-2 appears to use this enzyme similarly, however with a much higher affinity.¹⁶⁷ Once S protein binds to ACE2 receptors, TM protease serine 2 (TMPRSS2) found on the host cell membrane activates S protein, facilitating the entry of the virus into the host cell (**Figure 13 b**).¹⁶⁸ Upon fusion of the viral and plasma membranes, viral RNA is replicated and translated. The newly synthesized proteins and RNA genomes are assembled in the endoplasmic reticulum and Golgi and eventually bud into the endoplasmic reticulum-Golgi intermediate compartment lumen. Lastly, virus particles are released from the host cell.¹⁶²

1.3.3 Toolbox for designing antiviral polymers

1.3.3.1 Architecture of inhibitors

Architecture of the inhibitor scaffold plays a crucial role in facilitating multivalent interactions between nano and biological systems. The design of viral inhibitors is shown to be possible through different architectures including dendritic or linear polymers as well as a flexible 2D platform. Linear flexible scaffolds are likely to have a higher access rate to target receptors in comparison with relatively rigid globular or highly branched scaffolds with a similar molecular weight. The flexibility of linear scaffolds enables them to make more

ligand-receptor pairs, as well as sterically stanch off some areas of the pathogen.¹⁶⁹ A recent trend has been devoted to the use of diverse polymer architectures to reinforce interactions at nano-bio interfaces. For instance, it was demonstrated that LPG due to its more backbone flexibility inhibits the HSV-1 more efficiently than hPG (**Figure 14**). The purpose of the study was to examine the inhibitory effect of sulfated polyglycerol having three architectures including linear, dendronized, and hyperbranched against HSV-1. It was found that for the more flexible polymer, LPG, the half maximal inhibitory concentration (IC₅₀) was 0.03 nM, while it jumped significantly to 374 nM for less flexible compounds, including dendronized and hPG sulfate.²⁷ These results emphasize the crucial role of inhibitor architecture and, consequently, their flexibility in virus inhibition.

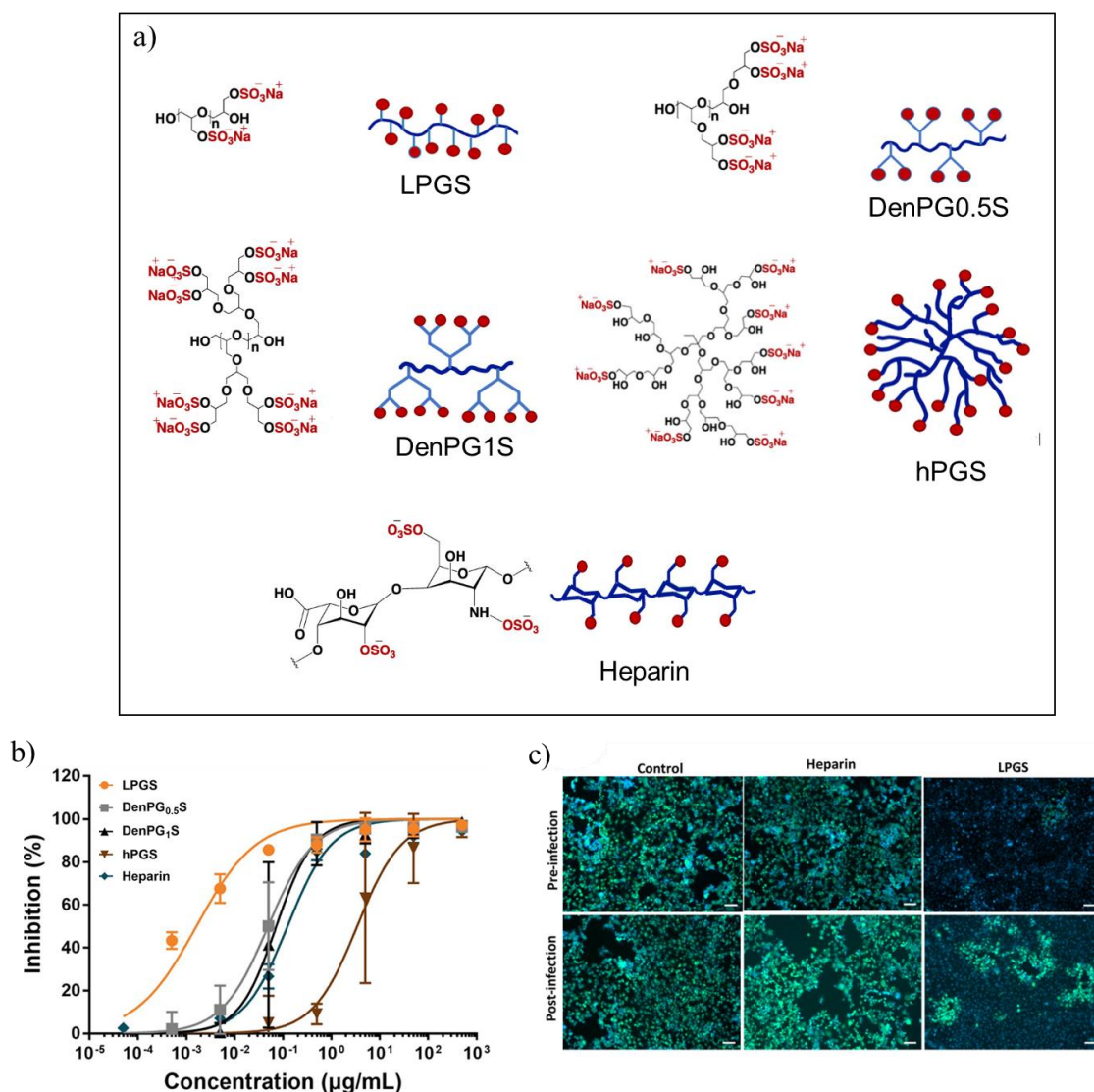


Figure 14. a) overview of the architectures. b) Dose-response curves of potential HSV-1 inhibitors. c) Fluorescent microscopy images of the infected cells that were treated with LPGS and Heparin before (post-modification) and after infection (post-infection). Reprinted with permission from Ref. [27]. Copyright 2021 American Chemical Society.

In another study, Dey *et al.*⁸ developed sulfated nanogels based on polyglycerol (PG) with different flexibilities but the same size (100-200 nm) (**Figure 15**). It was found that only around half of the concentration of flexible nanogels in comparison to rigid nanogels is required to achieve 50% inhibition. Moreover, functionalized 2D scaffolds are another potent class of inhibitors which are able to wrap up pathogens as they have a higher surface area and flexibility compared to 3D counterparts. However, there are still certain considerations to be aware of when applying 2D scaffolds as biological inhibitors. Studies have shown that the attachment of polymers to 2D templates can provide effective, yet low-cytotoxic, robust 2D platforms for a variety of biomedical uses.

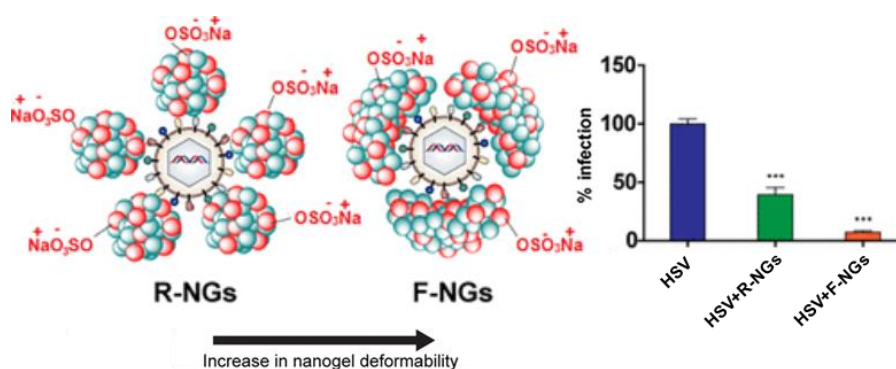


Figure 15. Schematic illustration of flexible and rigid dPGS-based nanogels and their efficacy against HSV. Reprinted with permission from Ref.[8]. Copyright 2018 American Chemical Society.

For instance, the functionalization of thermally reduced graphene oxide (TRGO) with sialylated hPG led to the development of functional 2D platforms with an effective inhibitory against influenza A virus (IAV) (**Figure 16**). It was observed that the combination of multivalency (hPG), flexible nanoplatforms architecture (TRGO), and optimal density of sialic acid (30%) can effectively bind and wrap virus particles, thereby inhibiting them.²⁹ The sulfated analogs of these compounds were also used in several other studies to mimic the extracellular matrix for effective HSV-1 and SARS-CoV-2 binding and inhibition.¹⁶⁹⁻¹⁷³

1.3.3.2 Inhibitor size

The size of an inhibitor can also have a major influence on its performance. It is therefore essential to choose the right size for designing potent and effective inhibitors. As it appears, the size dictates the area of the inhibitor that is in contact with a virus, and the greater the contact area, the more efficient the inhibition.¹⁷⁴

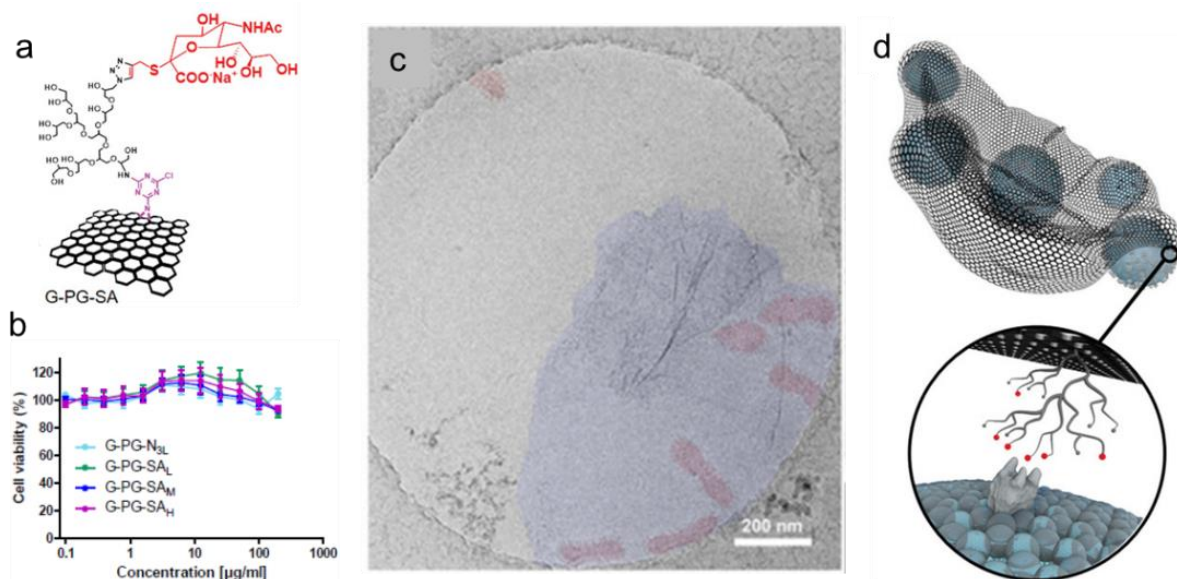


Figure 16. a) Schematic representation of TRGO functionalized with polyglycerol and sialic acid (G-PG-SA). b) Cell viability of the functionalized graphene. c) Cryo-electron micrograph of the G-PG-SA derivative incubated with IAV, the graphene sheet is blue and the virions red. d) Schematic representation of virus wrapping by functionalized graphene sheets. Many viruses can be trapped in graphene sheets due to their flexible structure. G-PG-SA derivatives bind to the virus surface via multivalent interactions between sialic acid ligands (red spheres) and spike glycoproteins (gray) localized on virus surfaces. Reprinted with permission from Ref. [175]. Copyright 2021 John Wiley and Sons.

As an example, sulfated hyperbranched polymers showed inhibition against heparan sulfate proteoglycans (HSPG)-binding viruses.⁴⁵ However, given their moderate molecular weight (<10 KDa), and consequently their relatively small size ($2 < d < 20 \text{ nm}$)⁴⁴ in comparison to pathogens ($100 \text{ nm} < D < \text{micrometers}$), these polymers cannot reach the same level of inhibition at the same concentration as larger scaffolds. It is also worth noting that larger inhibitors do not necessarily provide maximum inhibition, but more importantly, there is an optimal size, which has been determined to be a third of the virus size ($d/D \sim 0.3$) (**Figure 17**).¹⁷⁴

There are several ways to develop larger inhibitors including increasing the molecular weight of the polymer,²⁸ making hybrid structures by attaching polymers to bigger scaffolds such as carbon-based nanomaterials,¹⁷¹ and by crosslinking the polymer to build up larger architectures like nanogels.⁸ Wallert *et al.*²⁸ developed an antiviral compound inspired by mucins using hPG with a molecular weight of 2.6 MDa modified with sialic acid and sulfate moieties. As part of their study, they compared the inhibition potency of their mucin-sized inhibitor (2.6 MDa) to inhibitors with lower molecular weights (10-500 kDa) but bearing the equivalent functionalization. For the inhibitors of 10 to 500 kDa, IC₅₀ values were found to be in the micro molar range, whereas the mucin-sized inhibitors were in the pico molar range.

It has been suggested that the enhanced inhibition efficacy of the largest polymer comes from both its high molecular weight and its enhanced inhibition potency, as demonstrated through comparison of IC50 values given as mass concentrations.²⁸

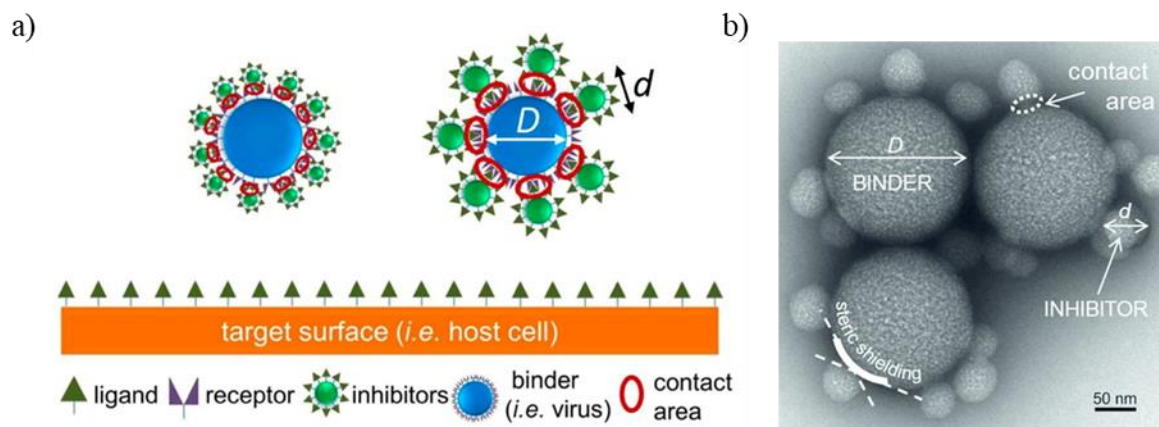


Figure 17. An illustration of the concept of globular inhibitors with varying sizes inhibiting virus-cell binding. Both the size of the inhibitor and the virus determines the contact area as well as the number of inhibitors needed to ensure steric shielding. These dimensions are indicated by d and D , respectively. b) TEM image of inhibitors with a diameter of 54 nm incubated with binders with a diameter of 192 nm. Reprinted with permission from Ref. [174]. Copyright 2015 American Chemical Society. Further permission related to the material excerpted should be directed to the ACS.

1.3.3.3 Surface charge of inhibitors

Most cell types of mammals are rich in HSPG, which is made from unbranched, highly sulfated HS polysaccharides. HSPG are negatively charged due to their high sulfation levels, allowing them to interact electrostatically with the basic residues of viral surface glycoproteins or capsid proteins of non-enveloped viruses. HSPG may serve as direct and specific entry receptors for viruses such as herpes simplex virus (HSV)-1.¹⁷⁶ However, it is common for most viruses such as SARS-CoV-2 to leverage these weak, yet nonspecific, interactions to boost their concentration on cell's surface and consequently increase their chance of interacting with more specific entry receptors, which in this case is the ACE2 receptor.¹⁶⁴ Furthermore, the receptor binding domain (RBD) of SARS-CoV-2 contains five amino acids that are positively charged and are located near the ACE2 binding site: R346, R355, K444, R466, and R509. Positively charged patches created by these amino acids, shown as blue in **Figure 18**, increase the virus' affinity for binding to the ACE2 receptor.¹⁶⁴ Understanding how viruses and cells interact electrostatically led to the development of polyelectrolytes as antiviral compounds.

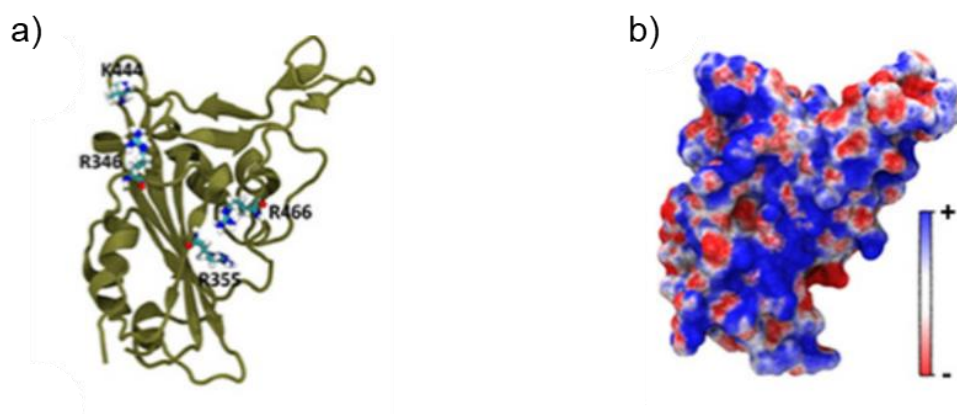


Figure 18. Crystal structure of RBD, the spike protein of SARS-CoV-2 (PDB ID: 6M0J). b) RBD's electrostatic potential map. Reprinted with permission from Ref.[164]. Copyright 2021 John Wiley and Sons.

As polycations cause membrane lysis,¹⁷⁷ they are extremely toxic and are solely applicable to non-viral gene transfections.¹⁷⁸ In contrast, polyanions are less toxic and have been found to inhibit viruses for decades.¹⁷⁹⁻¹⁸⁰ In the context of polyanionic systems, there are two theories that may explain how they inhibit viruses. In the first mechanism, the polymer attaches to the virus and contains its ability to interact with the host cell's surface. Nevertheless, the interactions between virion and polymer were shown to be reversible, so they cannot effectively neutralize viruses permanently. In addition, polyanions are ineffective if applied after viral replication has begun. *i.e.*, they are unable to suppress viral replication if the virus has entered the host cell. The second proposed mechanism is that polyanions may cause cells to release interferon, which alerts nearby cells to the presence of a virus.¹⁵³

There has been extensive *in vitro* research on polyanions for the inhibition of many viruses including HSV, HPV, or HIV.¹⁵³ For example, in a recent study, the efficacy of 14 polyanions with varying anionic functionalities (carboxylate, phosphate/phosphonate, and sulfonate) and hydrophobicity in treating 11 viruses, including Zika, HIV-1, and HSV-2 was evaluated (**Figure 19**). At least one polymer was found to have antiviral effects for enveloped viruses, which highlights the capability of anionic polymers to inhibit a broad range of pathogens. The researchers came to the conclusion that the combination of anion charge and hydrophobicity of the polymer backbones leads to efficiently broad-spectrum antiviral polymers.¹⁸¹ The impact of hydrophobicity will be discussed in more detail in the following sections.

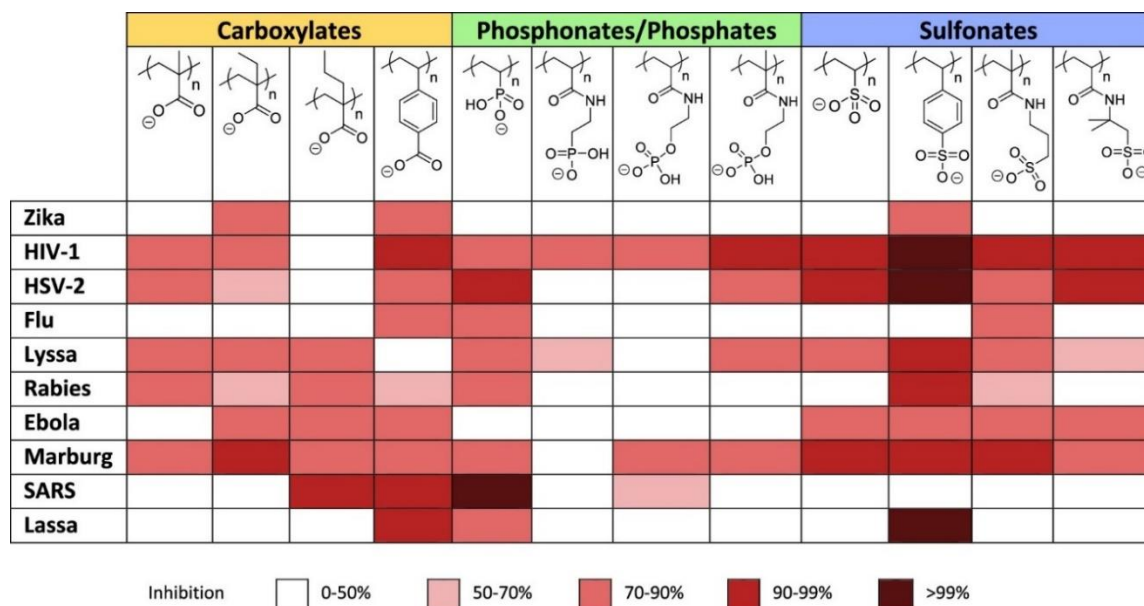


Figure 19. Evaluation of potential broad-spectrum polyanions. Reprinted with permission from Ref. [153]. Copyright 2020 American Chemical Society. Further permission related to the material excerpted should be directed to the ACS.

1.3.3.4 Hydrophobicity matters

Besides surface charge, size, and architecture of the scaffold, hydrophobicity plays a crucial role in infection inhibition. For instance, the hydrophobic-hydrophilic balance has been emphasized in the design of nucleic acid polymers acting as broad-spectrum inhibitors in clinical trials.¹⁸² However, the breakthrough came in combining electrostatics with hydrophobic interactions. The purpose of this strategy is often to lower inhibition concentrations; however, in some instances, the virus envelope was found to be irreversibly damaged, also known as the "virucidal inhibitory effect".^{146, 183} Further discussion regarding this subject will be found in **section 1.3.3.6**.

1.3.3.5 Multivalency concept

As the name implies, multivalent binding refers to non-covalent interactions between m-valent receptors and n-valent ligands ($m, n > 1$; and $m \neq n$).¹⁸⁴ Multivalent interactions are remarkably robust compared with their monovalent counterparts (**Figure 20**). Many commercial products benefit from multivalent interactions, such as Velcro tapes that use multiple flexible hooks to interact with targets with tight connections. Most of nature's biological interactions are also multivalent, as evidenced by interactions between viruses or bacteria and their receptors.¹⁸⁵ *i.e.*, viral surface components engage multivalently with the

receptors on cell membranes to attach to and, therefore, enter host cells. To inhibit viruses effectively, on the other hand, viruses must interact with inhibitors stronger than viruses do with cells. In this regard, monovalent inhibitors are not capable of fully blocking the receptors, thus they cannot defeat the viral binding effectively. As a result, for designing potent inhibitors, it is important to consider multivalency. There has been extensive research on the inhibition of many viruses including Influenza, HSV, HIV, and VSV using multivalent inhibitors of various architectures, such as linear polymers,^{27, 186-187} 2D polymers,^{170, 175} dendrimers,¹⁸⁸⁻¹⁸⁹ liposomes,¹⁹⁰⁻¹⁹¹ nanogels,^{8, 192} and nanoparticles.^{183, 193}

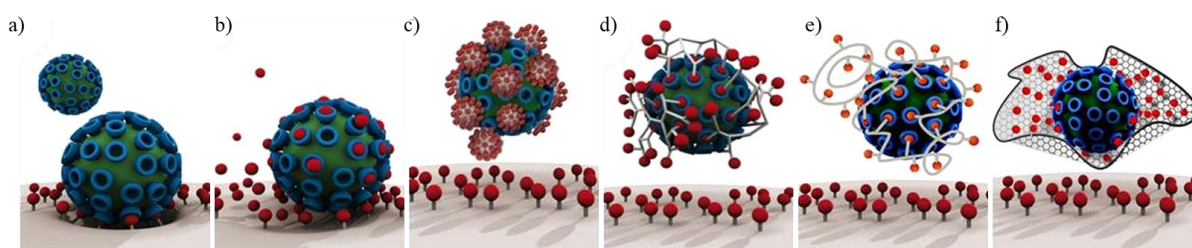


Figure 20. a) Inhibiting virus-cell interactions is possible using: b) monovalent inhibitors using conventional drugs, or multivalent inhibitors that protect cells from virus entry, including c) globular nanoparticles decorated with ligands, d) branched polymers such as hyperbranched, dendrimers, and star-like polymers, e) random coil linear polymers decorated with ligands, and f) a flexible 2D platform furnished with ligands. Reprinted with permission from Ref. [169]. Copyright 2016 American Chemical Society.

1.3.3.6 Virucidal vs. virustatic inhibitors

To kill or not to kill, that is the question. A virustatic entry inhibitor functions by attaching to the viral receptor, although inhibiting them in a reversible manner. In other words, the dilution effects *in vivo* result in reversible dissociation of binding complexes and ultimately causing the virus to become infectious again. Since these drugs reversibly inhibit inhibitors, they are of limited clinical value, although they have been the subject of a lot of research. On the other hand, virucidal compounds bind to viral particles and physically incapacitate them, for example by bursting their envelopes, which significantly restrict viral transmissions even when diluted in body fluids. Virucidal drugs are not defined solely based on their ability to kill viruses. For instance, surfactants can destroy and thereby inactivate a virus, but they cannot be classified as drugs because of their extreme toxicity. It is therefore crucial to design novel antiviral compounds capable of destroying viruses with minimal toxicity. Hydrophobic derivatives of polyethyleneimines (PEIs), polycation, were found to be bactericidal and virucidal in several studies performed by Klibanov's group.¹⁹⁴⁻¹⁹⁶ They synthesized linear and branched *N,N*-dodecyl methyl PEIs, prepared as painted coatings on glass slides and observed

that hydrophobicity can enhance the antiviral and antibacterial properties.¹⁹⁴ However, positively charged compounds are known to be highly toxic due to the possibility of disrupting the integrity of the cell membrane.^{177, 197} This approach was also explored by Stellaci's group using 11-undecane sulfonic acid as a hydrophobic linker to modify gold nanoparticles¹⁸³ and β -cyclodextrins¹⁹⁸ (**Figure 21**). These compounds appear to have virucidal effects on a variety of HSPG-binding viruses (e.g., HSV, respiratory syncytial virus (RSV), and Zika virus) without causing cellular toxicity of the concentration used. In order to emphasize the vital role of hydrophobicity, the hydrophobic alkyl chains were replaced by hydrophilic poly(ethylene glycol) (PEG) in another study.¹⁹⁹ Compounds with hydrophilic linkers exhibited only virustatic effects.

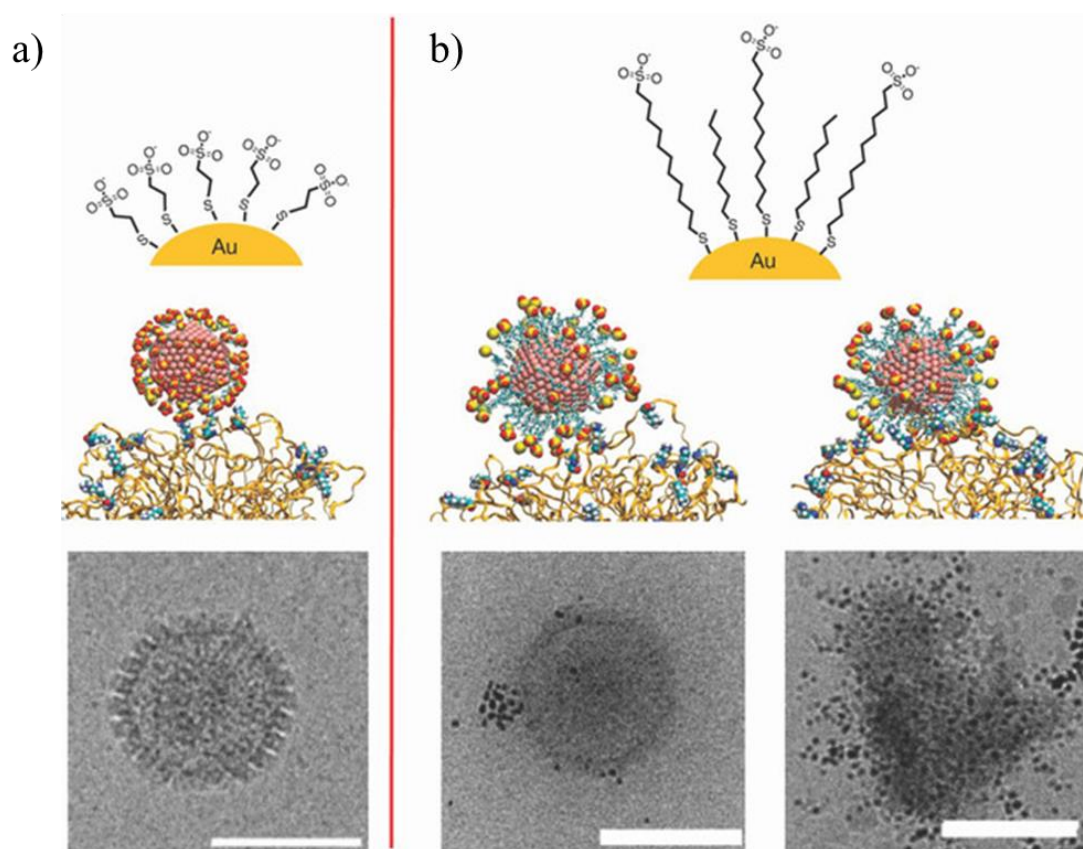


Figure 21. Images on (top) show chemical structures of the NPs, (middle) molecular dynamics simulations, and cryo-transmission electron microscopy (cryo-TEM) of HSV-2 interacting with the gold NPs coated with (a) 3-mercaptopropylsulfonate and (b) undecanesulfonic acid exhibiting virustatic and virucidal effect, respectively. This is an unofficial adaptation of an article appeared in *Advanced Healthcare Materials*¹⁴⁶ that is being made freely available through PubMed Central as part of the COVID-19 public health emergency response.

Beyond the development of tailor-made polymer architectures for the interaction and inhibition of viruses, their use in the delivery of mostly hydrophobic drugs *via* systemic

application is of importance as well. However, the focus will be on the delivery of the drugs through the skin in the following chapter.

1.4 Polymer for dermal delivery

The use of penetration enhancers (PEs) has been well understood and studied when it comes to dermatological diseases. PEs are agents or methods that enable other substances (e.g., drugs) to penetrate deeper layers of the skin by either changing the solubility of the administered therapeutic or disrupting the skin barrier. PEs can be classified into two groups: physical (e.g., microneedles) or chemical (e.g., fatty acids) PEs.²⁰⁰⁻²⁰¹ These methods have been studied over the last decade in an attempt to overcome the skin barrier, but the majority involve disrupting the stratum corneum.²⁰²⁻²⁰³ In an alternative approach, polymeric nanocarriers are employed to improve penetration without causing harm to the skin. Nanocarriers are used to carry drugs through the skin in three ways: i) by structural features such as hair follicles, ii) by interacting with skin lipids to enhance transport, or iii) by creating reservoirs that release drugs over time or under internal or external stimuli.²⁰⁴

1.4.1 Skin structure and penetration pathways

In order to understand how a drug may be transdermally administered, one must understand the fundamentals of skin anatomy and physiology. The human skin covers an area of 2 square meters and is the largest organ in the body.²⁰⁵ This organ serves as the body's interface with the external environment, therefore it is a vital physical barrier against a variety of environmental harmful influences such as ultraviolet radiation and xenobiotics. Anatomically speaking, the skin is composed of four layers: the stratum corneum (nonviable epidermis), the remaining layers of the epidermis (viable epidermis), the dermis, and subcutaneous tissues (hypodermis) (**Figure 22**).²⁰⁶ It is believed that the critical part of the skin's defense system lies in the stratum corneum, which is the epidermis' uppermost layer and has a thickness of 10-20 μm . It is formed of dead, flattened, keratin-rich cells (keratinocytes) and intercellular lamellar lipid bilayers.²⁰⁷ Potential penetration pathways for drug molecules across the stratum corneum are transcellular, intercellular, and transappendicular.²⁰⁸

A majority of drugs are absorbed *via* the intercellular route, which is defined as the transfer of drugs across intercellular bilayers of lipids. In the transcellular route, the drug crosses directly across keratinocytes and lamellar lipid bilayers to reach deeper layers of the

skin. These two pathways can be assessed by small molecules (<500 Da) and moderately lipophilic molecules. Highly lipophilic and larger molecules, however, cannot pass through these pathways.²⁰⁷

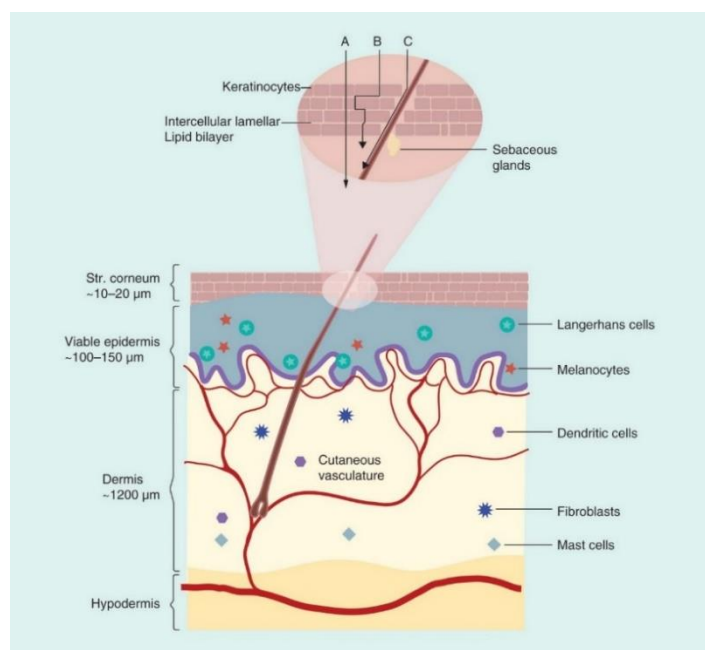


Figure 22. The structure of the skin and the potential penetration pathways. (A) Transcellular, (B) intercellular and (C) transappendageal routes. Reprinted with permission from Ref. [207]. Copyright 2017 Future Science Ltd.

This is where nanocarriers prove most promising as they enable the penetration of highly lipophilic and relatively high-molecular-weight drugs across the complex biological barrier with relatively few undesired side effects. In addition, although hair follicles are thought to play a minor role in skin penetration as they present a limited percentage of the whole skin surface (0.1 %), recent studies indicated that hair follicles have a notable role in penetration (transappendicular).²⁰⁹ It is believed that the movement of the hair functions as a pumping system. In particular, using larger nanoparticles provides a unique approach to bypass the stratum corneum barrier and deliver drug molecules throughout the hair follicle.²¹⁰

1.4.2 Toolbox for designing polymeric dermal carriers

1.4.2.1 Architecture of nanocarriers







Polymer architectures based on linear or branched polymers can be used for dermal drug delivery; however, they each have their own advantages and disadvantages. A number of derivatives of linear, branched, or a combination of the two have been used for dermal drug delivery, such as nanogels, nanofibers, core multi-shell, and solid nano particles. A wide

range of amphiphilic diblock copolymers that can form micelles, polymersomes, vesicles, and solid nanoparticles are of particular interest for dermal drug delivery. A few polymeric nanocarriers with diverse architectures for dermal drug delivery are listed in **Table 1**. In one study, Zabihi *et al.*¹⁶ synthesized 3D nanogels by enzymatic ROP of glycidol/succinic anhydride. Using succinic acid in nanogels improved biodegradability and loading capacity, while polyglycerol segments enhanced functionality, biocompatibility, and water solubility. Wang *et al.*²¹¹ reported preparing cationic TAT-conjugated polymeric lipid vesicles and investigating their potential to serve as transdermal drug delivery carriers. This polymeric-based architecture was able to enhance the drug's transdermal penetration and deliver a higher dose of the drug through the skin than conventional liposomes.

1.4.2.2 Size of nanocarriers

The size of nanocarrier is an important parameter for designing transdermal and dermal nanocarriers for two reasons: interface area and penetration depth.²¹²

Table 1. Some polymeric nanocarriers with diverse architecture for dermal drug delivery.

Architecture	Size (nm)	Surface charge (mV)	Cargo	Material used	Ref.
 Dendrimer	6-8	12 to 16	Dithranol	Fluorescein isothiocyanate-conjugated-polypropylene imine dendrimer (G ⁵)	[213]
 Micelle	70-165	n.a	Clotrimazole, econazole nitrate	mPEG-dihexPLA	[214]
 Nanofiber	168-396	n.a	Citrulline Malate	Poly (vinyl alcohol)	[215]
 Vesicle	50-60	27	lidocaine hydrochloride	TAT peptide conjugated with amphiphilic lysine-linoleic acid modified dextran and cholesterol	[212]
 Core multi-shell	12-254	n.a	dexamethasone	hPG-C18-mPEG	[216]
 Nanogels	160-280	-5 to -10	Tacrolimus, mTHPP	Poly(glycerol-co-succinic acid)	[16]

Firstly, the smaller particles have a larger interface area with the skin and, therefore, a larger contact.²¹⁴ Secondly, it has been demonstrated that the size of the carrier has a significant effect on the way it interacts with skin structures. Generally, the smaller the carrier, the deeper the penetration into the skin. This has been demonstrated in several studies with small nanoparticles (<10 nm).²¹⁷ For example, it was observed that smaller Poly(amidoamine) (PAMAM) dendrimers (generation 2 (G2)) penetrated deeper than those bigger (G4). Accordingly, the G2 PANAM had improved skin penetration up to 3.5% and penetrated more efficiently into the skin layers, as compared to the bigger nanoparticles (G4 PANAM), which penetrated only 0.6% after 24 hours.²¹⁸ Additionally, it has been found that even nanoparticles with a size of hundreds of nanometers can penetrate well but through different pathways. Nanoparticles such as nanogels with a size of 300-500 nm have shown effective penetration into hair follicles. Upon entering the hair follicles, they become a long-term reservoir of drugs that release when they are stimulated externally or internally.²¹⁹⁻²²⁰

1.4.3 Surface charge dictates transdermal fate

Many studies have proposed that surface charges on nanocarriers may contribute to drug penetration. Stratum corneum is known to have large proportions of negatively charged lipids, meaning that the skin acts like a negatively charged membrane. Consequently, a positively charged nanocarrier formulation may enhance skin penetration through electrostatic attraction.²²¹ However, in addition to positive nanoparticles, negative and neutral nanoparticles can also penetrate the skin.²²² Yang *et al.*²¹⁸ carried out a comprehensive study to better understand the consequence of surface charge on skin penetration by synthesizing cationic (G2-NH₂), anionic (G2-COOH), and neutral (G2-Ac) PAMAMs (**Figure 23**). It was discovered that the surface charge of nanoparticles dictates their transdermal fate. It has been hypothesized that G2-COOH passes through the layers of the skin extracellularly in order to avoid contact with the negatively charged membrane of the skin cells (charge repulsion). It is therefore faster to absorb negatively charged particles versus positively charged ones that internalize non-selectively into the cells. A lack of electrostatic interaction between neutral nanoparticles and the skin means that they follow concentration gradients to diffuse extracellularly through the skin layers, allowing them to penetrate into deeper layers more rapidly than G2-NH₂.

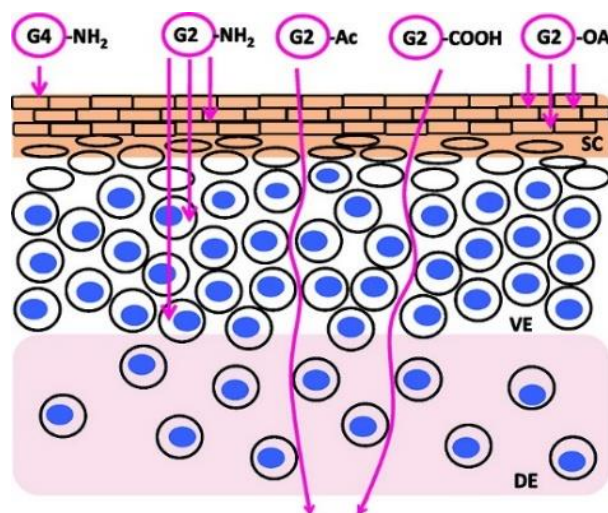


Figure 23. The penetration pathway for PAMAM based nanocarriers is controlled by their size, surface charge, and hydrophobicity. G2 and G4 of PAMAM with different functional groups including amino (NH_2), carboxylic acid (COOH), acetate (Ac), and oleic acid (OA) are applied to the skin. Reprinted with permission from Ref. [218]. Copyright 2012 American Chemical Society.

All in all, in addition to polymers architectures, many other factors must be considered when designing effective antiviral agents and nanocarriers that interact with biological interfaces, including biocompatibility, appropriate functionalization, flexibility, surface charge, hydrophobicity, and scaffold size.

2 Scientific Goals

In response to the ongoing COVID-19 pandemic, the world has become increasingly aware of the importance of combating the spread of viruses. Vaccine development, production, and clinical trials can take several years. It is therefore necessary to develop new materials for binding and incapacitate viruses before the next pandemic break out, so that vaccines can be produced in time.¹⁴⁶ Deactivation of viruses by wrapping them with flexible nanomaterials is an appealing strategy.¹⁷⁰ However, there are three critical characteristics that must be met: (i) the scaffold must be large (>100 nm), (ii) water dispersible (or, better, soluble), and (iii), sufficiently decorated with suitable ligands to bind effectively to viruses.¹⁷⁵ The distinctive physical and chemical features of 2D nanomaterials, such as mechanical strengths, flexibility, high surface areas, high level of loading, photothermal, photodynamic, and antimicrobial properties, make them potential candidates/scaffolds for biomedical applications.⁷³ However, there are still concerns regarding the cytotoxicity of 2DNs, environment hazard risks, and non-specific interactions at biointerfaces in biomedical applications.⁷⁴⁻⁷⁵ Our first project aims to address these issues by developing a new approach to synthesize biocompatible two-dimensional polymers using a 2D template. To avoid the aforementioned concerns, the template should be cleavable, making it easy to remove from the system. In order to prove that architecture plays a decisive role, three-dimensional counterparts on the same size scale need to be synthesized and compared with their effectiveness at nano-bio interfaces (*i.e.*, the attachment of viruses to cell surfaces).

Besides developing a polyfunctional 2D nanomaterial which can inhibit viruses using the wrapping strategy, the second objective involves proposing a straightforward and scalable technique by which antiviral compounds exhibiting virucidal activity can be synthesized. Compounds that are virucidal bind to viruses and physically render them inactive, *i.e.*, they disrupt the envelope of the virus, preventing the transmission of infection even after dilution in bodily fluids.¹⁹⁸ However, virucidal drugs are not evaluated exclusively by their ability to destroy viruses. Otherwise, a very toxic material such as a surfactant may also be capable of destroying and thereby inactivating a virus, but since they are highly toxic, they cannot qualify as a drug.¹⁴⁶ Thus, it is necessary to create novel antiviral compounds that can destroy viruses with minimal toxicity. The high biocompatibility of hPG makes it suitable for various biomedical applications, including the development of virus inhibitors.²²³ The ideal solution would be to develop a non-toxic method in which the high molecular weight hPG can be

produced without leaving toxic residues such as solvents.⁹³ The combination of hydrophobic and electrostatic interactions has proven to be invaluable in achieving virucidity.^{146, 183, 199} These parameters should, therefore, be factored into the design of final inhibitors. It was found that sulfation affects inhibitory effects, so compounds with high levels of sulfation can be advantageous. Hydrophobicity of the compounds, however, should be regulated, as high hydrophobicity was reported to cause toxicity and thus reduce the selectivity index. Furthermore, the reproducibility and the batch size of the polymerization and functionalization have to be taken into consideration.

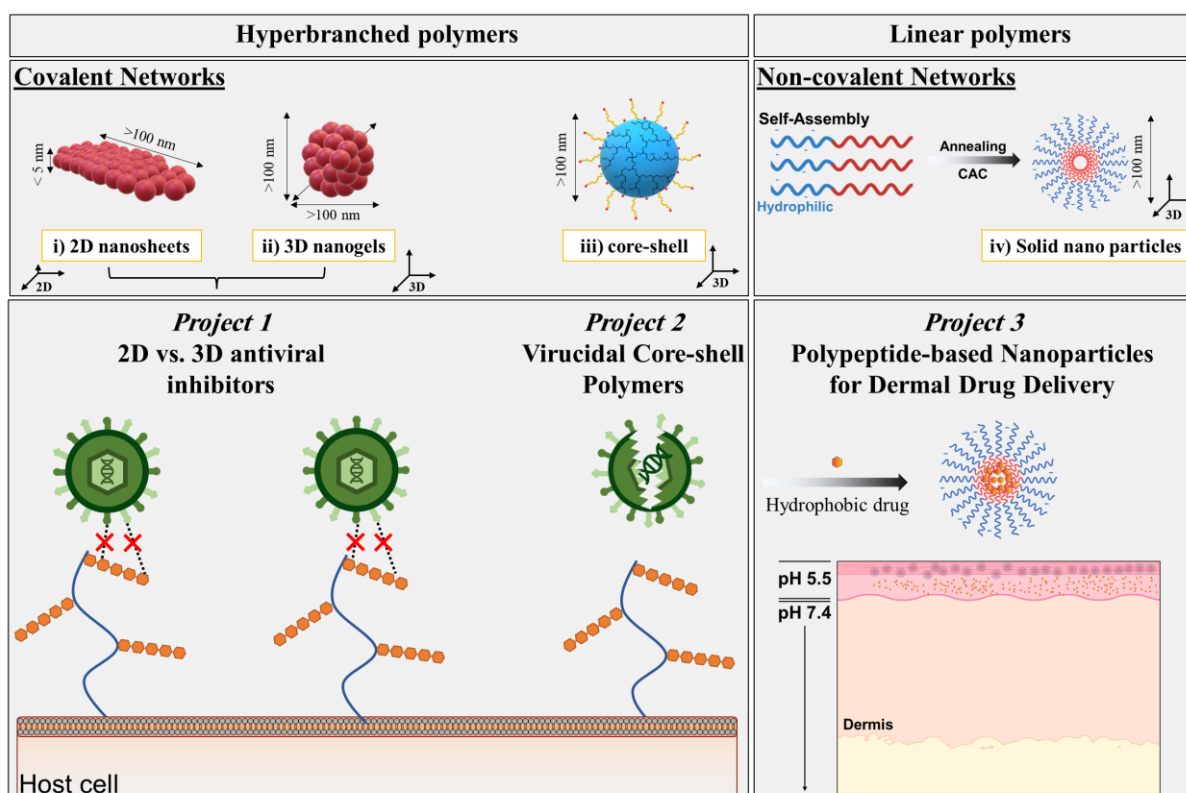


Figure 24. An overview of the projects outlined in this thesis.

The third objective of this thesis is to synthesize a functional polymeric network with a defined architecture that can be studied in a more complex physicochemical environment than *in vitro*, namely *ex vivo* skin penetration and dermal drug delivery. This class of compounds should be biodegradable and have a high loading capacity. In this context, ionic amphiphilic co-polypeptides are of particular interest due to their biocompatibility, biodegradability, and long circulation time in the blood.²²⁴⁻²²⁵ By regulating their hydrophobic-hydrophilic balance, they have the capability of self-assembling in water, typically forming stable nanostructures, which are relevant to biomedicine in particular.⁵⁰ To

do so, I aim to synthesize polypeptides as potential functional materials. In order to determine the sweet spot, the aim is to synthesize a series of ionic block copolymers that differ in hydrophobic content and charge and examine whether they are suitable for drug delivery through the skin. I aim to use *m*-THPP which is a close congener of the approved photosensitizer *m*-THPC. The purpose of this study is to examine *in vitro* drug release under various conditions, as well as *ex vivo* skin penetration and drug release. In addition to confirming the formation of aggregates by measuring the critical aggregation concentration, TEM can also be used to gain an understanding of the behavior of the aggregates.

3 Publications

3.1 Graphene-Assisted Synthesis of 2D Polyglycerols as Innovative Platforms for Multivalent Virus Interactions

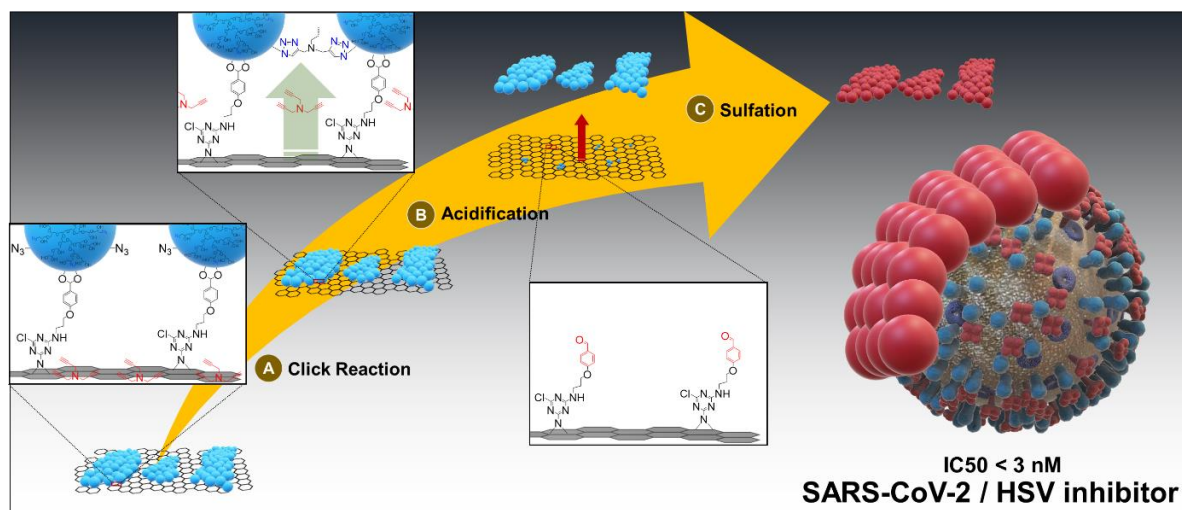


Figure 25. Reprinted with permission from Ref. [226]. Copyright 2021 John Wiley and Sons.

Ehsan Mohammadifar[‡], **Vahid Ahmadi**[‡], Mohammad Fardin Gholami, Alexander Oehrl, Oleksandr Kolyvushko, Chuanxiong Nie, Ievgen S. Donskyi, Svenja Herziger, Jörg Radnik, Kai Ludwig, Christoph Böttcher, Jürgen P. Rabe, Klaus Osterrieder, Walid Azab, Rainer Haag*, Mohsen Adeli*.

[‡]*These authors contributed equally to this work.*

Adv. Funct. Mater. **2021**, 31, 2009003.

<https://doi.org/10.1002/adfm.202009003>

Author contributions:

Vahid Ahmadi and Ehsan Mohammadifar contributed equally to the synthesis of the materials, the performance of the experiment, and the writing of the manuscript. Mohammad Fardin Gholami and Jürgen P. Rabe performed and analysis AFM characterization. Alexander Oehrl partially helped in the synthesis part of 3D nanogels. Oleksandr Kolyvushko, Chuanxiong Nie, Klaus Osterrieder, and Walid Azab supported the virology experiments. Ievgen S. Donski and Jörg Radnik performed the XPS analysis. Svenja Herziger, Kai Ludwig, and Christoph Böttcher performed the TEM experiments. Rainer Haag and Mohsen Adeli supervised the project and edited the manuscript.

Graphene-Assisted Synthesis of 2D Polyglycerols as Innovative Platforms for Multivalent Virus Interactions

Ehsan Mohammadifar, Vahid Ahmadi, Mohammad Fardin Gholami, Alexander Oehrl, Oleksandr Kolyvushko, Chuanxiong Nie, Ievgen S. Donskyi, Svenja Herziger, Jörg Radnik, Kai Ludwig, Christoph Böttcher, Jürgen P. Rabe, Klaus Osterrieder, Walid Azab, Rainer Haag,* and Mohsen Adeli*

2D nanomaterials have garnered widespread attention in biomedicine and bioengineering due to their unique physicochemical properties. However, poor functionality, low solubility, intrinsic toxicity, and nonspecific interactions at biointerfaces have hampered their application in vivo. Here, biocompatible polyglycerol units are crosslinked in two dimensions using a graphene-assisted strategy leading to highly functional and water-soluble polyglycerols nanosheets with 263 ± 53 nm and 2.7 ± 0.2 nm average lateral size and thickness, respectively. A single-layer hyperbranched polyglycerol containing azide functional groups is covalently conjugated to the surface of a functional graphene template through pH-sensitive linkers. Then, lateral crosslinking of polyglycerol units is carried out by loading tripropargylamine on the surface of graphene followed by lifting off this reagent for an on-face click reaction. Subsequently, the polyglycerol nanosheets are detached from the surface of graphene by slight acidification and centrifugation and is sulfated to mimic heparin sulfate proteoglycans. To highlight the impact of the two-dimensionality of the synthesized polyglycerol sulfate nanosheets at nanobiointerfaces, their efficiency with respect to herpes simplex virus type 1 and severe acute respiratory syndrome corona virus 2 inhibition is compared to their 3D nanogel analogs. Four times stronger in virus inhibition suggests that 2D polyglycerols are superior to their current 3D counterparts.

1. Introduction


Synthetic 2D nanomaterials (2DNs) have attracted wide attention in the past several years, due to the possibility of tuning their physicochemical and optoelectronic properties by manipulating their structure and functionality.^[1] They are emerging as new vectors for different biomedical applications because of their unique mechanical and physicochemical characteristics including mechanical strength, flexibility, high surface area, high loading capacity, and photothermal, photodynamic, and antimicrobial properties.^[2] However, major concerns regarding health risks, poor functionality, and solubility as well as nonspecific interactions at biointerfaces are serious challenges for their in vivo applications.^[3] The strong structure-property relationships of 2DNs open up new avenues to overcome the aforementioned challenges via controlled synthetic methods.^[4] In order to synthesize new 2DNs with

Dr. E. Mohammadifar, V. Ahmadi, Dr. A. Oehrl, Dr. C. Nie,

Dr. I. S. Donskyi, Prof. R. Haag
Institut für Chemie und Biochemie
Freie Universität Berlin
Takustrasse 3, 14195 Berlin, Germany
E-mail: haag@zedat.fu-berlin.de

M. F. Gholami, Prof. J. P. Rabe
Department of Physics and Integrative Research Institute
for the Sciences IRIS Adlershof
Humboldt-Universität zu Berlin
Newtonstrasse 15 and Zum Großen Windkanal 2, 12489 Berlin, Germany

O. Kolyvushko, Prof. K. Osterrieder, Dr. W. Azab
Institut für Virologie
Robert von Ostertag-Haus
Zentrum für Infektionsmedizin
Freie Universität Berlin
Robert-von-Ostertag-Str. 7-13, 14163 Berlin, Germany

 The ORCID identification number(s) for the author(s) of this article can be found under <https://doi.org/10.1002/adfm.202009003>.

© 2021 The Authors. Advanced Functional Materials published by Wiley-VCH GmbH. This is an open access article under the terms of the Creative Commons Attribution-NonCommercial License, which permits use, distribution and reproduction in any medium, provided the original work is properly cited and is not used for commercial purposes.

Dr. I. S. Donskyi, Dr. J. Radnik
BAM – Federal Institute for Material Science and Testing Division
of Surface Analysis, and Interfacial Chemistry
Unter den Eichen 44-46, 12205 Berlin, Germany

Dr. S. Herziger, Dr. K. Ludwig, Dr. C. Böttcher
Forschungszentrum für Elektronenmikroskopie und Core Facility
BioSupraMol
Institut für Chemie und Biochemie Freie Universität Berlin
Fabeckstrasse 36a, 14195 Berlin, Germany

Prof. K. Osterrieder
Department of Infectious Diseases and Public Health
Jockey Club College of Veterinary Medicine and Life Sciences
City University of Hong Kong
Kowloon Tong, Hong Kong

Prof. M. Adeli
Department of Chemistry
Faculty of Science
Lorestan University
Khorramabad, Iran
E-mail: adeli.m@lu.ac.ir

DOI: 10.1002/adfm.202009003

diverse atomic structure, configurations, and alluring structure-dependent properties, the mechanism of their synthetic route and reaction parameters should be fully understood. Examples of well-defined 2DNs obtained by known mechanisms were reported for special applications.^[5] The template-assisted synthetic strategies, including vat photopolymerization, electron beam lithography, nanocontact printing, dip-pen lithography, and photolithography, are well recognized as precise and reliable approaches to construct a wide range of 2DNs.^[6] In spite of their efficiency, such approaches are expensive and in the most cases cannot be used for the high scale production of 2DNs. On-surface reactions using colloidal templates, however, are straightforward, scalable, and cost-effective approaches by which a variety of 2DNs can be synthesized.^[7] The efficiency of this approach strongly depends on the interactions between monomers and the template.^[8] In this method, monomers are stabilized on the template by noncovalent interactions,^[9] and the mobility of monomers facilitates their self-rearrangement as well as formation of defects or cracks during polymerization.^[10] However, the monomers could also come off the template, which lead to side reactions in solution and by-products that are difficult to remove from the main product.^[11] With this approach the interactions between the template and monomers should be much stronger than between the solvent and monomers. This challenge limits the versatility of on-surface reactions using colloidal templates.

Covalent attachment of monomers on the surface of a template decreases the side reaction of template-desorbed monomers and results in more defined products with less impurity. This approach is, in particular, useful for functional (macro) monomers, which is difficult to deploy on the surface of a template. The critical point in the covalent approach is the attachment of monomers on the surface of the template by easily cleavable bonds, allowing for later detachment of the 2DNs from the template by external factors. Hyperbranched polyglycerol (hPG) is a polyfunctional, biocompatible, and water-soluble macromolecule with low non-specific interactions at biointerfaces. hPG is used for many biomedical applications ranging from drug delivery to pathogen interactions.^[12] According to a previous *in vivo* toxicology study of intravenous injection of hPG with a molecular weight of 10 kDa demonstrated a serum half-life of the compound of 12 days.^[13] Recently, it was shown that the attachment of this polymer on the surface of 2D templates resulted in functional 2D platforms with a high potential in biomedical applications.^[12c,14] For example, their sulfated analogs were used as extracellular matrix mimics for the efficient virus binding and inhibition.^[15]

They are 2D heparan-mimicking scaffolds with high surface area that attach to viral glycoproteins through electrostatic interactions and inhibit virus attachment, which is the first step of infection. Accordingly, heparan-mimicking compounds have been proposed as potential infection inhibitors against a number of pathogens, including SARS-CoV-2, which is currently causing a pandemic of historic proportions.^[16] The electrostatic interaction of angiotensin-converting enzyme 2 and heparan sulfate with a positively charged patch on the receptor binding domain of the SARS-CoV-2 spike glycoprotein lends support to this hypothesis.^[17] However, the toxicity of the graphene template on which polyglycerol branches are attached is a challenging issue which negates the advantages of these systems.^[15a]

Therefore, production of template-free 2D polyglycerols is a big step toward water soluble and highly functional 2DNs with high biocompatibility and great potential for virus inhibition.

In this work, graphene sheets were used as flexible templates to construct 2D polyglycerols in solution. In this synthetic strategy, polyglycerol branches with 10% azide groups (hPG-N₃(10%)) were conjugated to the surface of graphene sheets by pH sensitive linkers and they were laterally crosslinked by a copper-catalyzed click reaction. Tripropargylamine was adsorbed on the surface of polyglycerol-functionalized graphene sheets and used as a crosslinker. The association of tripropargylamine with the graphene surface and lifting off this reagent by a controlled heating diminished the risk of inter-sheet crosslinking and resulted in 2D polyglycerol upon acidification and centrifugation. Virus-nanosheet interactions showed that sulfated polyglycerol nanosheets are more active than their 3D nanogel analogs, which highlights the critical role of topology in virus inhibition and steric shielding. Sulfated polyglycerol nanosheets as heparan sulfate mimics were also able to strongly inhibit SARS-CoV-2.

2. Results and Discussion

Graphene sheets with polyglycerol coverage have recently shown great potential as antimicrobial and antitumor systems.^[15b,d,18] The toxicity of the graphene platform and related health risks are challenging issues for future developments. Accordingly, we have designed a synthetic strategy to produce graphene free 2D polyglycerol as a new class of 2D functional nanomaterials for future biomedical applications. In our current work, graphene was used as a platform for the synthesis of 2D polyglycerols due to the following rationale: i) graphene surfaces are inert against usual reactions under mild conditions and, therefore, do not interfere with the reactions in our study; ii) the loading and lifting-up of the cross-linker through which lateral crosslinking is performed in a controlled manner is based on structure and π -conjugated system of graphene; iii) graphene can be functionalized by straightforward organic reactions; and iv) graphene is a colloidal template and dispersible in solvents. Therefore, we can take advantage of both solution and solid states of graphene. Thermally reduced graphene oxide with a lateral size in the range of 500 nm to 2 μ m bearing dichlorotriazine functional groups (G-Trz) was synthesized^[19] and post-functionalized by 3-(4-(dimethoxymethyl)phenoxy)propan-1-amine (DMPA) to obtain a platform (G-linker) with the ability of covalent attachment to the diol groups of polyglycerol through acid cleavable acetal bonds (Figure 1).^[20] Then hPGol with 10% azide functionalization (hPG-N₃(10%)) was conjugated to the pH sensitive linkers to create a polyglycerol coverage on the surface of graphene sheets (G-hPG). Crosslinking of polyglycerol coverage by Cu-catalyzed azide/alkyne click reaction and separation of the crosslinked coverage by acidification resulted in graphene-free 2D hPG (2D-hPG). The key point in this synthetic strategy was to adsorb the crosslinker on the surface of hPG-functionalized graphene sheets and exclude any free tripropargylamine to avoid inter-template crosslinking (Figure 1).

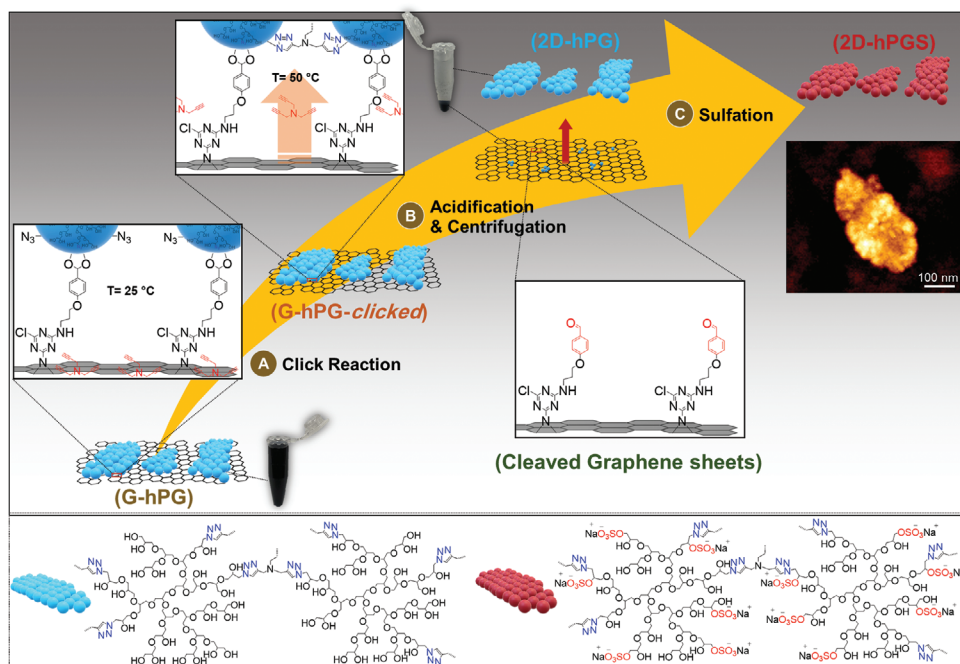


Figure 1. Schematic illustration and synthetic route for 2D hyperbranched polyglycerol. 2D-hPG can be formed on both sides of graphene but for simplification it is shown only on one side. Vial in the top-middle displays the aqueous solution after click reaction and acidification. While the graphene template is precipitated in the bottom of vial upon centrifugation, 2D polyglycerol remains in the supernatant. Finally, the 2D-hPG is sulfated and the inset shows an SFM image of the final multivalent 2D-hPGS nanosheets.

In order to synthesize a graphene template with pH-sensitive linkers, 2,4,6-trichloro-1,3,5-triazine was conjugated on the surface of thermally reduced graphene oxide (G) by a nitrene [2+1] cycloaddition reaction at ambient conditions.^[19] The ratio of dichlorotriazine functional groups to the number of carbon atoms of graphene, the so-called density of functional groups, was 1/45 and 1/49 according to elemental and thermogravimetric analysis, respectively (Equation S1, Supporting Information). These results are consistent with our previous data, indicating the reproducibility of this functionalization method. The peak components ranging from 285 to 289 eV in the highly resolved C1s X-ray photoelectron spectroscopy (XPS) spectrum of G-Trz were assigned to the contribution of C–N and C–Cl bonds of dichlorotriazine groups (Figure 2b).^[14b,15b,19b,21] In the IR spectrum of G-Trz, the absorbance bands at 1450–1550 cm⁻¹ are assigned to C=C and C=N bonds of dichlorotriazine rings, which is another indication for the functionalization of graphene (Figure S4c, Supporting Information).^[19b]

DMPA, as a pH-sensitive linker, was synthesized according to the reported method in literature with a slight modification (Scheme S1a, Supporting Information).^[20b] A nucleophilic reaction between DMPA and G-Trz resulted in the G-linker template with the ability to covalently attach to the hPG through acid cleavable bonds (Scheme S1b, Supporting Information). Survey XPS spectra showed that the G-linker was composed of carbon, nitrogen, and oxygen elements (Figure 2a). An increased oxygen/carbon ratio in the XPS survey spectrum and decreased C–C/C=C component in the C1s spectrum of the G-linker were indications for the attachment of DMPA to the surface of G-Trz. Elemental analysis showed a decrease in the nitrogen content

upon attachment of DMPA to the surface of G-Trz. Since the carbon content of DMPA is higher than its nitrogen content, this result is a further indication of the post-modification of G-Trz by DMPA (Table S1, Supporting Information). The infrared (IR) spectrum of G-linker showed absorbance bands at 1100 and 2900 cm⁻¹, which are assigned to the C–O and aliphatic C–H bonds of DMPA moieties, respectively, conjugated to the surface of G-Trz (Figure S4d, Supporting Information).

Then hPG-N₃(10%) units were conjugated to the surface of G-linker by benzacetal moieties in the presence of catalytic amount of PTSA and G-hPG with a polyglycerol coverage was obtained (Scheme S1b, Supporting Information).^[20a] The non-attached polyglycerols were removed by a 100 kDa ultrafiltration membrane to avoid undesired 3D crosslinking. An intense oxygen peak at 530.0 eV in the survey XPS spectra of G-hPG was due to the polyglycerol branches attached to the surface of the graphene template (Figure 2a). In the highly resolved C1s XPS spectrum, the peak components at 286.1 and 284.6 eV correspond to the C–O and C=C bonds of polyglycerol and graphene fragments (Figure 2d). Thermogravimetric analysis (TGA) and XPS showed 73% and 75% polyglycerol content for G-hPG, respectively (Figures 2d and 3a). The IR spectrum of G-hPG showed absorbance bands at 1100, 2100, 2900, and 3400 cm⁻¹, which are assigned to the C–O, azide, aliphatic C–H, and hydroxyl groups, respectively (Figure 3b). In the proton nuclear magnetic resonance (¹H NMR) spectrum of G-hPG, signals at 3.2–4.2, 7.3, and 7.8 ppm were assigned to the protons of backbone of polyglycerol and aromatic protons of DMPA, respectively (Figure 3e).

The reversibly linked polyglycerol-azide on G-hPG was then crosslinked via Cu^I-catalyzed click reaction between

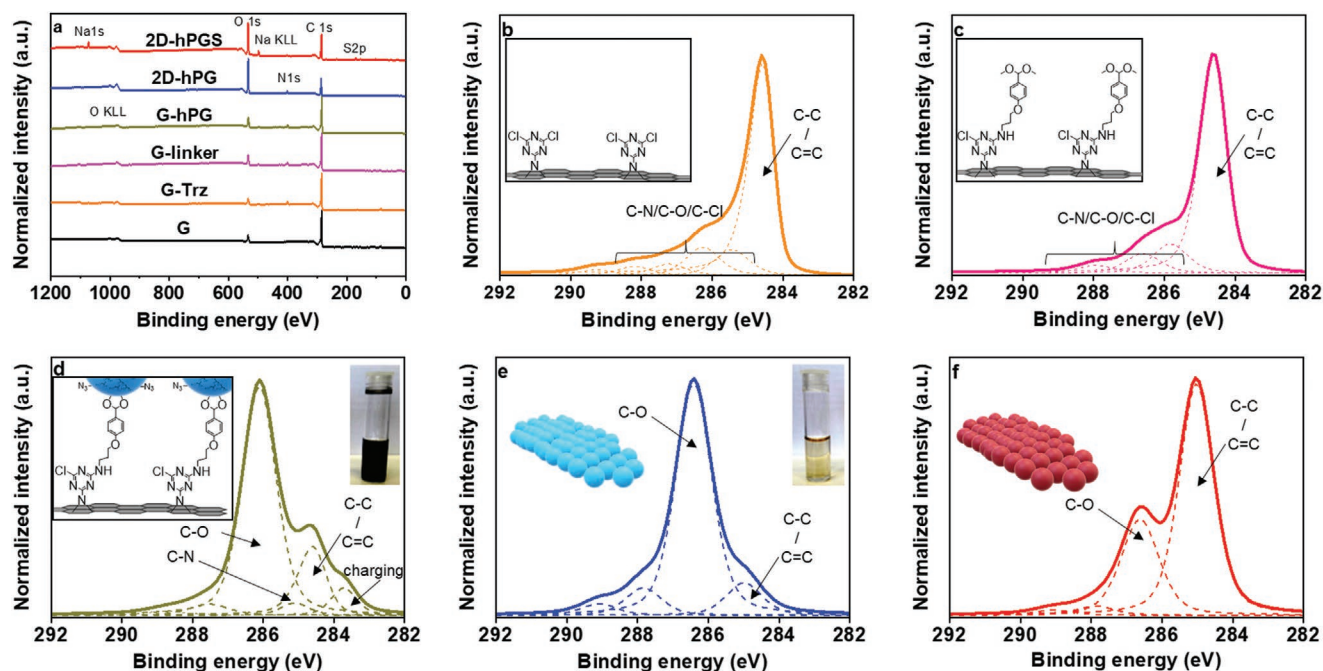


Figure 2. a) Survey XPS spectra of the synthesized materials. Highly resolved XPS C1s spectra of b) G-Trz, c) G-linker, d) G-hPG, e) 2D-hPG, and f) 2D-hPGS. The main components are denoted on each spectrum. For further details of the assigned components see Table S4, Supporting Information. Inset: (d and e) are photographs of aqueous solutions of G-hPG and 2D-hPG, respectively.

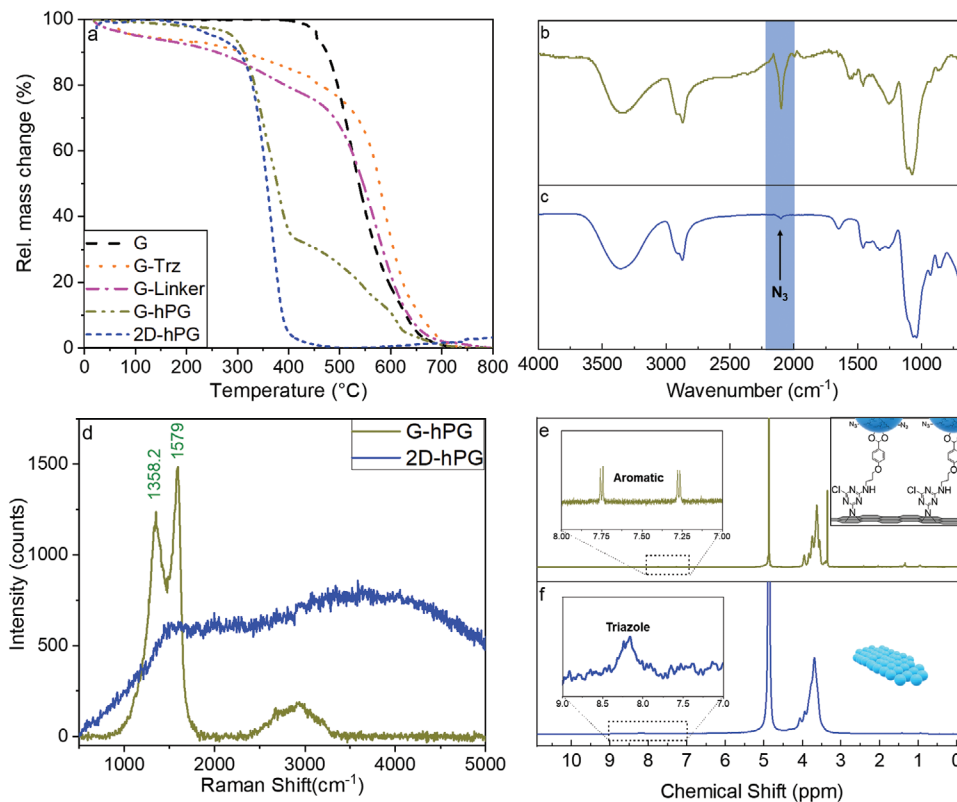


Figure 3. a) TGA thermograms of G, G-Trz, G-linker, G-hPG, and 2D-hPG. IR spectra of b) G-hPG and c) 2D-hPG. d) Raman spectra of G-hPG and 2D-hPG. $^1\text{H-NMR}$ spectra of e) G-hPG and f) 2D-hPG.

tripropargylamine and the azide groups selectively at the graphene interface. Tripropargylamine was loaded onto the surface of the graphene platform by π - π interactions. After loading, the product was purified to exclude free tripropargylamine that had not adsorbed onto the template. Confining tripropargylamine between the polyglycerol coverage and the graphene platform diminished the risk of inter-sheet crosslinking (Figure 1).

The click reaction was monitored by recording the IR spectra of the reaction mixture at intervals and checking the intensity of the azide band at 2100 cm^{-1} (Figure S5f, Supporting Information). The end point of reaction was realized by the disappearance of the azide band in the IR spectra. 2D polyglycerol (2D-hPG) sheets were subsequently detached from the graphene template by cleaving the acetal bonds in acidic solution (pH 4) and separated by subsequent centrifugation (Figure 1; Scheme S1, Supporting Information). Raman spectra of 2D-hPG did not show the D and G peaks of graphene, signifying the complete removal of template from the final product (Figure 3d). However, TGA showed $\approx 25\%$ of hPG left on the surface of graphene after acid cleavage of 2D polyglycerol (Figure S7, Supporting Information).

The composition, size, and the morphology of 2D-hPG were investigated by different spectroscopic and microscopic methods as well as elemental and thermal analysis. A change in the component corresponding to C-C/C=C bonds in the highly resolved C1s XPS spectrum of 2D-hPG confirmed successful detachment of the graphene template from the polyglycerol nanosheets (Figure 2e; Tables S3 and S4, Supporting Information). Moreover, the triazole proton signal at 8 ppm in the ^1H NMR spectrum of 2D-hPG is an indication for the crosslinking of polyglycerol branches via click reaction (Figure 3f). Next the 2D-hPG was sulfated to obtain 2D-hPG sulfate (2D-hPGS) as an extracellular matrix mimic for the pathogen interactions. Elemental analysis showed 7.9 wt%

sulfur content for 2D-hPGS, which had been correlated to the sulfation of 58% of the hydroxyl groups of its precursor. A S2p peak component in the XPS survey spectrum (Figure 2a) and a change in the highly resolved C1s XPS spectrum of 2D-hPGS (Figure 2f) as well as absorbance bands of S=O bonds at 1200 cm^{-1} in the IR spectrum of this compound (Figure S5g, Supporting Information) indicated the successful sulfation of 2D-hPG.^[15a,22] The negative surface charge of 2D-hPGS also corresponded to the sodium sulfate groups which are created upon sulfation (Figure 5h).

Scanning force microscopy in quantitative imaging mode (SFM-QI) and in tapping mode (TM-SFM) were used in order to investigate the lateral size, precise thickness, and morphology in addition to other properties of 2D-hPGS, such as stiffness and energy dissipation. We used freshly cleaved muscovite mica as a substrate of atomically flat and clean support for deposition of the 2D-hPGS. SFM-QI was used for precise height measurements and TM-SFM height images for lateral and morphological measurements at ambient conditions (22 – $25\text{ }^\circ\text{C}$ and 30 – 35% rH). Those SFM methodologies demonstrated sheet-like structures distributed on the substrate (Figure 4a–c). These islands showed a typical average height of $2.7 \pm 0.2\text{ nm}$ (Figure 5b,d) and $263 \pm 53\text{ nm}$ average lateral dimension (error being standard deviation) (Figure 4; Figure S7g, Supporting Information). Since the hydrodynamic diameter of a single hPG macromolecule, measured by dynamic light scattering in water, is $5.34 \pm 0.29\text{ nm}$ (Figure S8a, Supporting Information), we counted this thickness for a single layer 2D-hPG at ambient conditions. The observed average height for 2D-hPGS was assigned to the monolayer nanosheets at their partially compressed state due to lower water content at the mica surface compared to aqueous solution. To further quantify the two-dimensionality of the synthesized 2D-hPGS, their aspect ratio was calculated via dividing the maximum lateral length

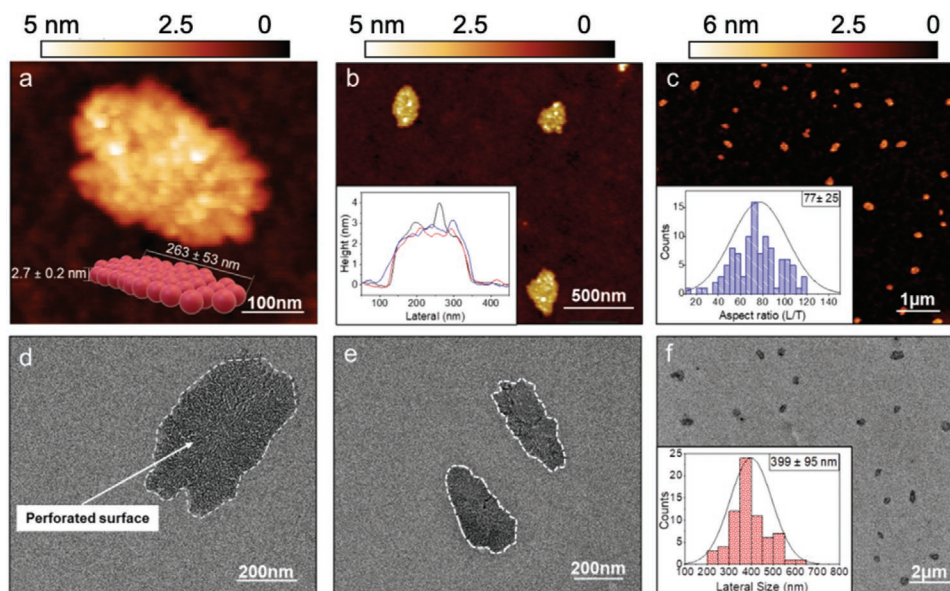


Figure 4. Characterization of polyglycerol nanosheets by different microscopic methods. a–c) SFM images of 2D-hPGS, deposited onto muscovite mica surface with different magnifications. Inset of Figure 4b,c is height profiles and aspect ratios of 2D-hPGS sheets, respectively. d–f) Transmission electron microscopy (TEM) images of 2D-hPGS. Inset of Figure 4f is lateral size of 2D-hPGS.

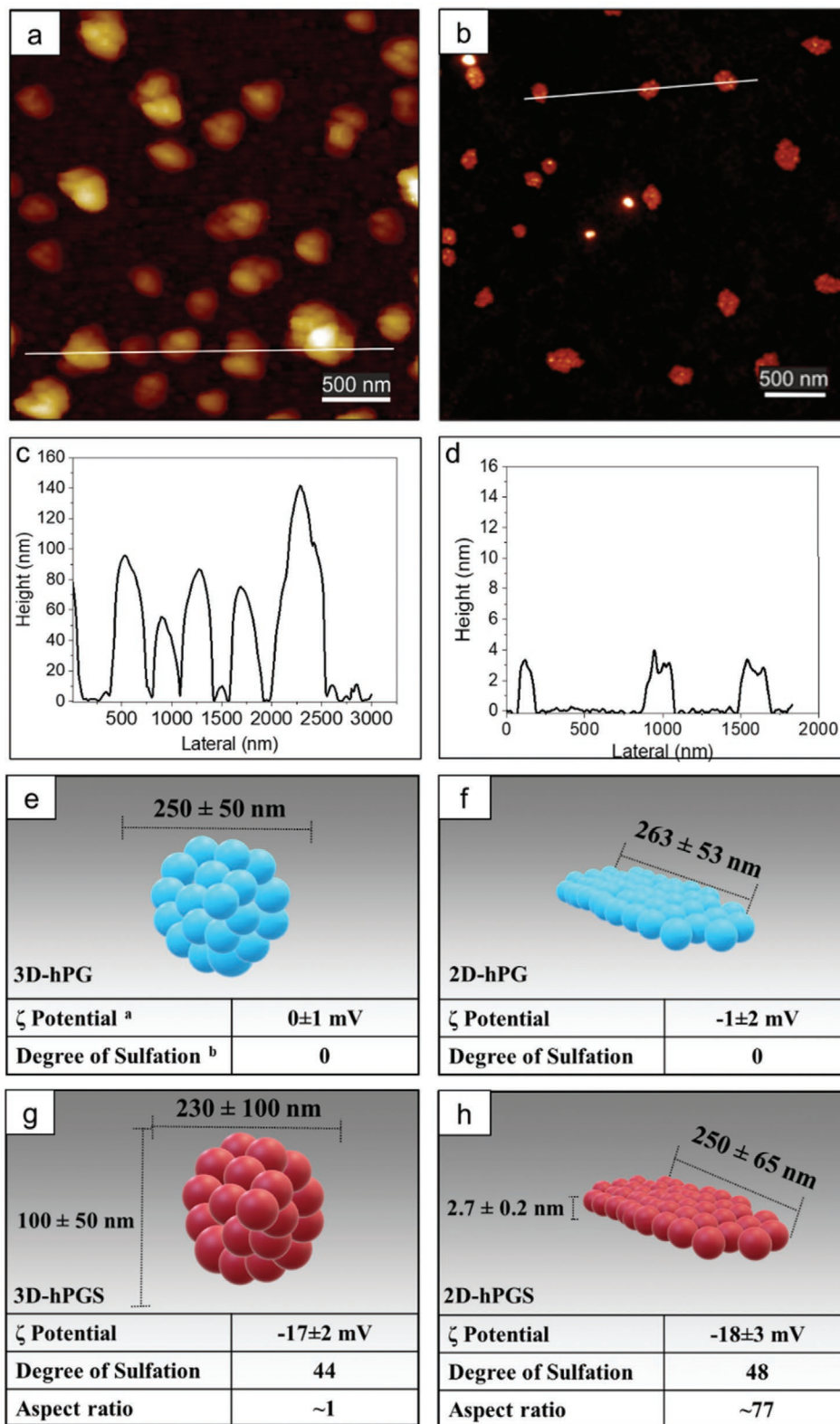


Figure 5. SFM and height profile of a,c) 3D-hPGS and b,d) 2D-hPGS. e–h) Comparison of the properties of sulfated and non-sulfated 2D and 3D polyglycerols in terms of lateral size, height, surface charge, and functional groups. In Figure 5e, ^athe surface charges were measured by Zetasizer. ^bThe percentage of hydroxyl groups, which were converted to sulfate groups, were calculated by elemental analysis based on the sulfur content.

by thickness. Considering the spherical or ellipsoidal structure and an aspect ratio close to one for hPG, a mean aspect ratio of 77 was achieved for the 2D-hPGS. (Figure 4c inset). Transmission electron microscopy showed sheet-like structures with clear edges and perforated surface for 2D-hPGS (Figure 4d–f). Additionally, scanning electron microscopy showed a bumpy surface with 250 ± 65 nm average lateral size for 2D-hPG (Figure S6, Supporting Information).

The successful production of 2D-hPG sheets by click reaction was further investigated by setting up a control experiment, where the G-hPG (without the crosslinking agent) was stirred in acidic solution at room temperature for 24 h and then

centrifuged. The supernatant was dialyzed by a 100 kDa membrane but no detectable compound was obtained. Because the cleaved polyglycerol branches were not crosslinked, they were small enough to leave the dialysis tube (Figure S3c, Supporting Information).

In order to highlight the role of graphene as the template in the synthesis of 2D-hPG, a control reaction was performed. In this reaction, hPG-N₃ (10%) units were crosslinked by tripropargylamine but in the absence of the graphene template (Figure S3d, Supporting Information). This control reaction resulted in small clusters of the hPG with random dimensions from 2 to 6 nm and aspect ratio close to unity, confirming the

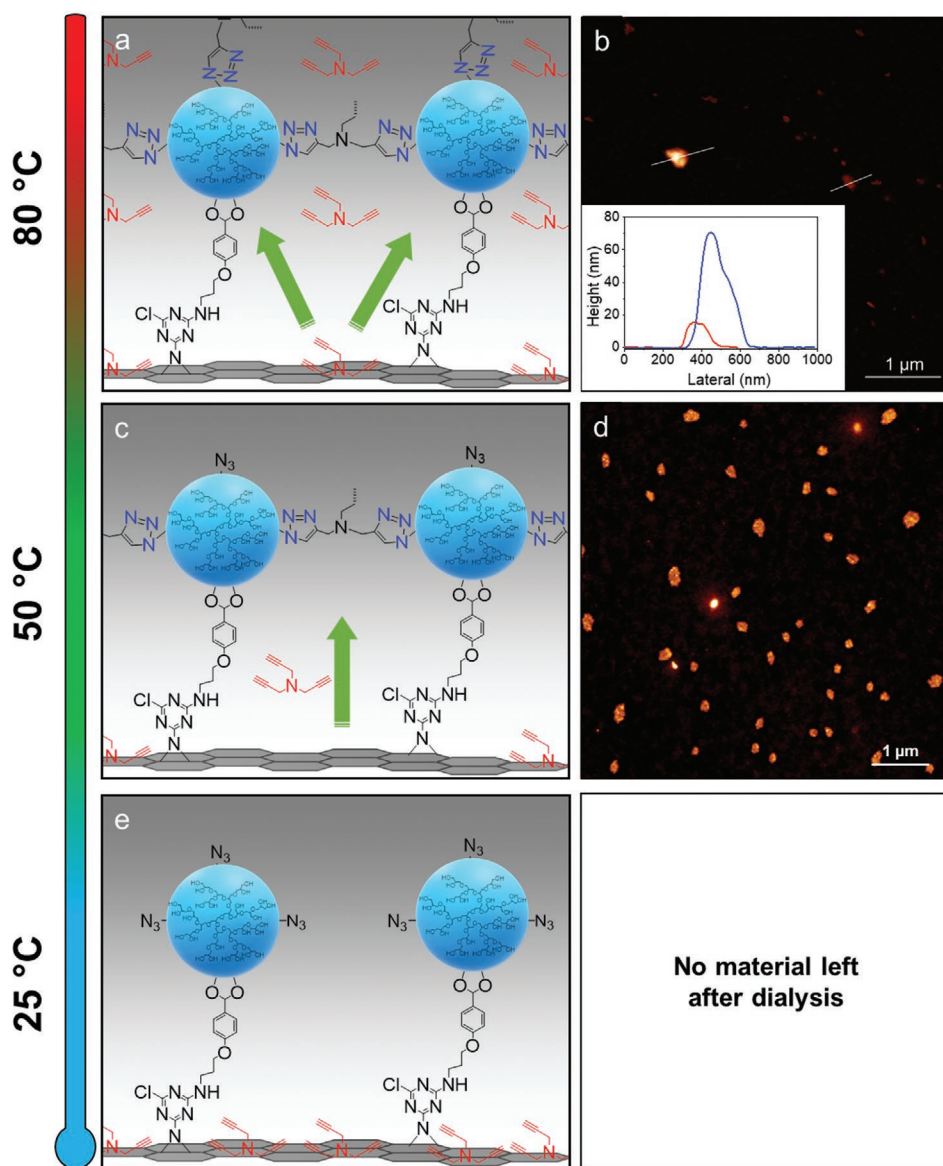


Figure 6. Representation of the key role of temperature in the synthesis of 2D-hPG. a) At 80 °C tripropargylamine molecules were able to leak from the polyglycerol coverage sublayers and inter-sheet crosslinking resulted in 3D structures. b) TM-SFM height images showed 3D objects with heights between 5 and 70 nm. c) The optimized temperature to produce 2D-hPG was 50 °C, where tripropargylamine molecules caused lateral crosslinking. d) SFM-QI height images showed successful crosslinking of polyglycerol macromolecules and production of 2D-hPG (height 2.7 nm). e) At 25 °C, the tripropargylamine molecules were not released from the graphene surface and crosslinking did not occur. SFM experiments did not show any detectable object after acidification, centrifugation, and dialyzing the supernatant of the reaction.

critical role of graphene template for the production of 2D-hPG (Figure S3e, Supporting Information).

In order to prove the key role of temperature in releasing tripropargylamine molecules from the graphene surface, two additional control reactions were performed at room temperature and 80 °C. In these reactions, G-hPG with the loaded tripropargylamine molecules were stirred at the above-mentioned temperatures and they were monitored by spectroscopy and microscopy methods. While no significant decrease of the azide band in the IR spectrum of reaction mixture was observed at room temperature, it completely disappeared at 80 °C after 6 h (Figure 6a,b; Figure S5b, Supporting Information). However, SFM measurements showed a non-regular 3D morphology for the reaction product at 80 °C with a particle height between 5 and 70 nm (Figure 6b and inset). These control reactions confirmed the key role of the temperature in the production of 2D-hPG. At room temperature, tripropargylamine molecules were not released from graphene template significantly. Therefore an efficient click reaction and lateral crosslinking did not occur (Figure 6e; Figure S5a, Supporting

Information). However, at 80 °C tripropargylamine molecules were able to leak from the polyglycerol coverage into the reaction environment, leading to inter-sheet crosslinking and 3D objects (Figure 6b). These results are supported by our previous reports, in which increasing the temperature to 50–60 °C triggered the release of small molecules from the surface of graphene sheets.^[14b]

In order to highlight the critical role of two dimensionality in bio-nano interactions, 3D analogs of 2D-hPG and 2D-hPGS (3D-hPG and 3D-hPGS, respectively) with similar average sizes were synthesized.^[23] The detailed synthetic procedure and characterization are explained in the Supporting Information. SFM-QI mode was used to investigate 3D-hPGS at their hydrated state by immobilizing them within DI water at the mica interface (coated with poly-l-lysine layer). The cross section images of the 3D-hPGS nanogels revealed structures with 100 ± 50 nm and 230 ± 100 nm average height and lateral sizes, respectively (Figure 5a,c; Figure S8, Supporting Information). The difference between the morphology of 2D-hPG and 3D-hPG can be visually and quantitatively understood by

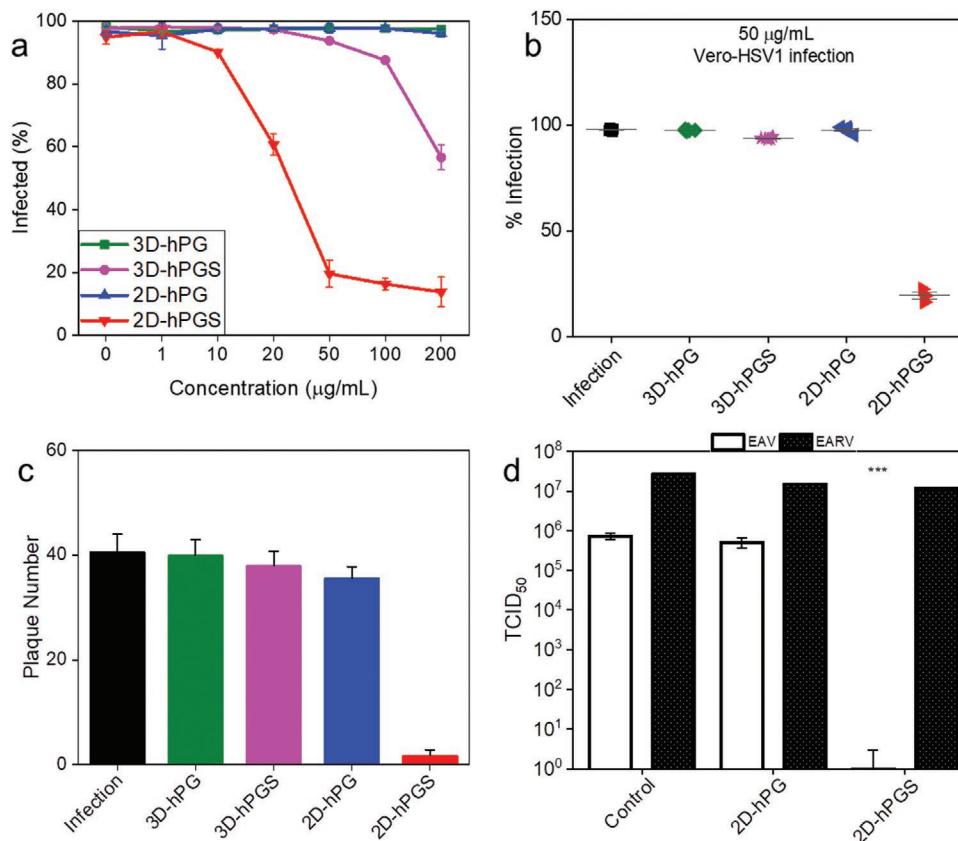


Figure 7. Comparative inhibition effects of 2D-hPG and their 3D analogs on viruses in susceptible cells. a) Concentration-dependent inhibition of HSV-1 infection on Vero E6 cells. Cells were infected with HSV-1 at MOI of 1 using different concentrations of the compounds as indicated. After 20 h of infection, the percentage of infected cells was analyzed by flow cytometry. b) Reduction of HSV-1 infection in Vero E6 cells at 50 µg mL⁻¹. HSV-1 (MOI = 1) was mixed with different compounds and added to cells. After 20 h of infection, the percentage of infected cells was analyzed by flow cytometry. c) Plaque reduction assay of HSV-1 with 3D-hPG, 3D-hPGS, 2D-hPG, and 3D-hPGS (concentration: 50 µg mL⁻¹) on Vero E6 cells. Vero E6 cells were grown in a 24-well plate and infected for 1 h with 50 PFU per well of HSV-1 in the presence or absence of 50 µg mL⁻¹ of 2D and 3D compounds. At 48 h after infection, the number of plaques was quantified with inverted fluorescence microscope. d) Inhibitory effects of 2D compounds on enveloped and non-enveloped viruses. Reduction of tissue culture infection dose 50 (TCID₅₀) was used to measure the effects of 2D-hPGS on two viruses, equine rhinitis A virus (ERAV) and equine arteritis virus (EAV). Serial tenfold dilution of ERAV or EAV was added to RK-13 or BD cells, respectively, in the presence or absence of 2D-hPG and 2D-hPGS (50 µg mL⁻¹). Virus titer was determined after 4 days as described in the Supporting Information and Experimental Section.

considering their aspect ratio and overall topography. While 2D-hPG showed a sheet-like structure with average height of 2.7 ± 0.2 , the average height of 3D-hPG was 100 ± 50 nm in the hydrated state.

2D-hPGS and 3D-hPGS as heparan sulfate mimics were expected to show low toxicity and efficient interactions with HS-binding domains on viral glycoproteins; particularly herpes virus gB and gC. Accordingly, the cytotoxicity of these nanomaterials and their ability for virus inhibition was investigated. While 2D-hPGS and 3D-hPGS did not show a significant cytotoxicity in vitro (Figure S9, Supporting Information), they efficiently inhibited infection of cells by enveloped viruses, including herpes simplex virus type 1 (HSV-1) on Vero E6 cells (Figure 7a–c) and equine arteritis virus (EAV) on bovine dermal (BD) cells (Figure 7d). Next, the efficiency of 2D-hPGS to inhibit HSV-1 infection on Vero E6 cells was determined. Different concentrations (ranging from 1 to 200 $\mu\text{g mL}^{-1}$) of 2D-hPGS were incubated with HSV-1 (at a multiplicity of infection (MOI) of 1) and applied to Vero E6 cells. After 24 h, infected cells were quantified using flow cytometry. A strong inhibition of infection at a concentration of 50 $\mu\text{g mL}^{-1}$ with a half-maximal inhibitory concentration (IC_{50}) of 20 $\mu\text{g mL}^{-1}$ (≈ 1.3 nm) (Figure 7a,b) against HSV-1 was observed for 2D-hPGS. In contrast, the 3D-hPGS did not cause a significant inhibition of infection at 50 $\mu\text{g mL}^{-1}$ and its IC_{50} was four times higher than the 2D analog (Figure 7a,b). Similar results of the inhibitory potential of the 2D-hPGS were determined by a plaque reduction assay. For a comparative

study all the candidates at a concentration of 50 $\mu\text{g mL}^{-1}$ were mixed with HSV-1 (50 PFU (plaque-forming units)) and incubated with Vero E6 cells. To restrict virus spread from cell-to-cell, the cell monolayer was overlaid with 0.5% carboxymethylcellulose medium. Only 2D-hPGS showed a strong and significant reduction in plaque numbers (Figure 7c). From this data, it can be clearly understood that the ability of 2D-hPGS to inhibit the infection is much higher than 3D-hPGS, highlighting the critical role of morphology and two-dimensionality in shielding this nano-biointerface. Interestingly, the 2D-hPGS did not inhibit infection of RK-13 cells by equine rhinitis A virus (EARV) a non-enveloped small RNA virus (Figure 7d). Although EARV has a heparan sulfate-binding motif, it seems that this virus enters into the cells through a sialic acid-mediated pathway rather than HS-binding domains.^[24] This may explain why the 2D-hPGS did not block EARV infection. Taken together, both 2D-hPGS and 3D-hPGS were able to specifically interact with HS-binding domains on viral proteins of enveloped viruses but 2D analogs showed stronger inhibitory effect than 3D-hPGS. This could be attributed to the 2D feature of 2D-hPGS, because, at a similar weight, they have a higher surface area than their 3D counterparts. In 2D-hPGS, more sulfate groups are accessible, which results in stronger interaction with the HS receptors on the surface of the virus. However, in 3D-hPGS, many of sulfate groups are hidden because they are present inside the gel and not accessible for interaction with virions. In addition to the large available surface area, energy

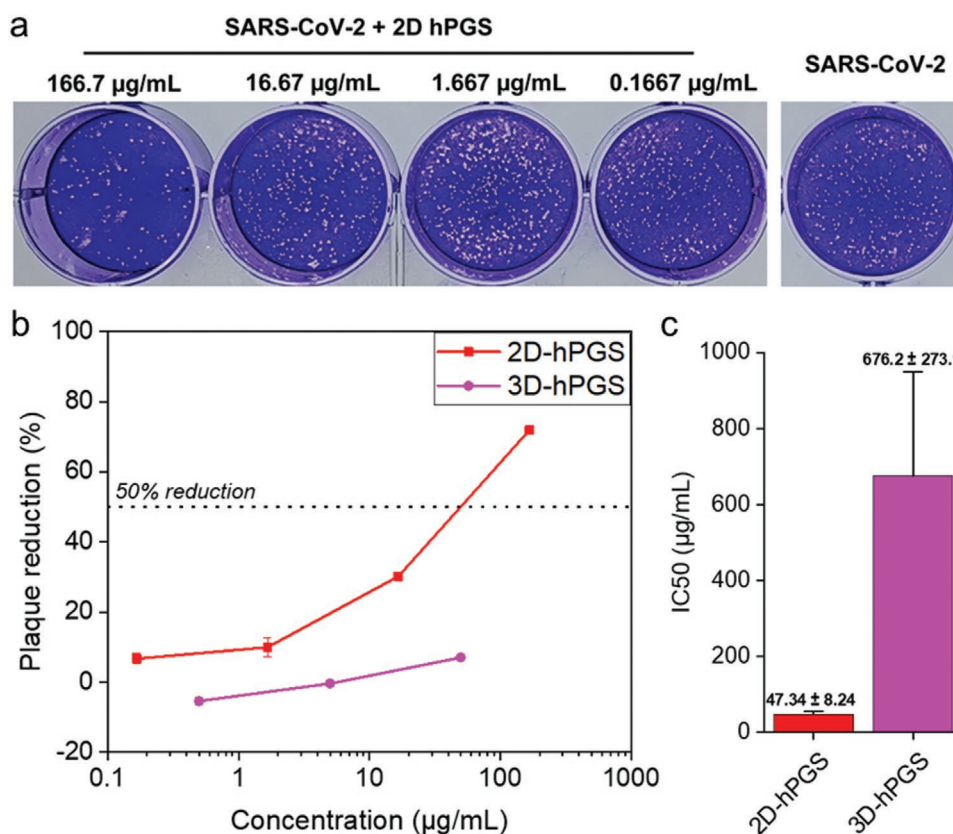


Figure 8. a) Representative images for the plaque reduction by 2D-hPGS. b) Plaque reduction ratios for the 2D-hPGS and 3D-hPGS at different concentrations. c) The obtained IC_{50} values from plaque reduction for 2D-hPGS and 3D-hPGS.

requirement in creating multivalent interactions are often much smaller in the case of lower dimensionality.^[15d,23,25]

The ability of the synthesized nanomaterials for coronavirus (SARS-CoV-2) inhibition was investigated by plaque reduction assay (Figure 8). Recently it was reported that heparin could inhibit the interaction of the spike glycoprotein (S) of SARS-CoV-2 with its cognate receptor.^[17b,26] Consistent with the HSV-1 inhibition data, 2D-hPGS showed an IC50 value of $47.34 \pm 8.24 \mu\text{g mL}^{-1}$ ($\approx 3 \text{ nM}$, Equation S7, Supporting Information). This is likely due to binding of negatively charged 2D-hPGS to the positively charged patch at the receptor-binding domain of the S protein of SARS-CoV-2. This positively charged patch facilitated virus binding to cell surface heparan sulfate and explain the higher infectivity of SARS-CoV-2.^[17b] Blocking the positively charged patch with a highly negative-charged inhibitor could decrease the binding of SARS-CoV-2 to the host cells surface and inhibit virus infection. The effective inhibition of SARS-CoV-2 by 3D-hPGS was much lower than 2D-hPGS, which again indicated the key role of two-dimensionality at this interface. 2D-hPGS showed no clear cellular toxicity at a concentration of $200 \mu\text{g mL}^{-1}$, which supports its potential application as an inhibitor for SARS-CoV-2 (Figure S9, Supporting Information).

3. Conclusion

We have developed a unique bottom-up approach to synthesize 2D-hPG using a graphene-assisted strategy. Sulfation of 2D-hPG resulted in an extracellular matrix mimic with the ability of blocking the infection with representative enveloped viruses, including HSV-1 and SARS-CoV-2. Controlling the lateral crosslinking of polyglycerol branches by noncovalent interactions between the crosslinker and the graphene template was the key point of this synthetic approach. A salient aspect of this approach is that versatile polyfunctional 2DNs can be readily fabricated using different crosslinkers or through accurate post-modification of the obtained 2D hPG. In addition, we showed how two-dimensionality plays a crucial role for virus interactions by mimicking the cellular surface due to the high aspect ratio and multivalent interactions of 2D-hPGS.

Supporting Information

Supporting Information is available from the Wiley Online Library or from the author.

Acknowledgements

E.M. and V.A. contributed equally to this work. The authors thank Cathleen Schlessner for hPG synthesis and measuring gel permeation, M Eng. J. Stockmann for performing XPS measurements, and Dr. Pamela Winchester for proofreading the manuscript. This study was supported by the SFB 765 and the core-facility BioSupraMol (www.biosupramol.de), both funded by the Deutsche Forschungsgemeinschaft (DFG). This study was also supported by the CoV pre-exploration project which is funded by Berlin University Alliance (BUA). M.F.G acknowledges the support of the Cluster of Excellence "Matters of Activity. Image Space Material" funded by the Deutsche Forschungsgemeinschaft (DFG, German Research Foundation) under Germany's Excellence Strategy – EXC 2025 – 390648296.

Open access funding enabled and organized by Projekt DEAL.

Conflict of Interest

The authors declare no conflict of interest.

Data Availability Statement

Research data are not shared.

Keywords

2D materials, graphene template, multivalency, polyglycerol, virus inhibition

Received: October 21, 2020

Revised: February 8, 2021

Published online: March 26, 2021

- [1] a) M. Xu, T. Liang, M. Shi, H. Chen, *Chem. Rev.* **2013**, *113*, 3766; b) K. Kang, S. Xie, L. Huang, Y. Han, P. Y. Huang, K. F. Mak, C.-J. Kim, D. Muller, J. Park, *Nature* **2015**, *520*, 656; c) H. Zhang, *ACS Nano* **2015**, *9*, 9451; d) G. Galeotti, F. De Marchi, E. Hamzehpoor, O. MacLean, M. Rajeswara Rao, Y. Chen, L. V. Besteiro, D. Dettmann, L. Ferrari, F. Frezza, P. M. Sheverdyayeva, R. Liu, A. K. Kundu, P. Moras, M. Ebrahimi, M. C. Gallagher, F. Rosei, D. F. Perepichka, G. Contini, *Nat. Mater.* **2020**, *19*, 874; e) K. Zhang, T. H. Lee, J. H. Cha, H. W. Jang, J.-W. Choi, M. Mahmoudi, M. Shokouhimehr, *Sci. Rep.* **2019**, *9*, 13739.
- [2] a) G. Liu, H. Qin, T. Amano, T. Murakami, N. Komatsu, *ACS Appl. Mater. Interfaces* **2015**, *7*, 23402; b) P. Payamyar, B. T. King, H. C. Öttinger, A. D. Schlüter, *Chem. Commun.* **2016**, *52*, 18; c) D. Wang, W. Zhou, R. Zhang, J. Zeng, Y. Du, S. Qi, C. Cong, C. Ding, X. Huang, G. Wen, T. Yu, *Adv. Mater.* **2018**, *30*, 1803569; d) M. Li, Z. Luo, Y. Zhao, *Sci. China: Chem.* **2018**, *61*, 1214.
- [3] a) L. M. Guiney, X. Wang, T. Xia, A. E. Nel, M. C. Hersam, *ACS Nano* **2018**, *12*, 6360; b) Z. Wang, W. Zhu, Y. Qiu, X. Yi, A. von dem Bussche, A. Kane, H. Gao, K. Koski, R. Hurt, *Chem. Soc. Rev.* **2016**, *45*, 1750; c) M. Fojtů, W. Z. Teo, M. Pumera, *Environ. Sci.: Nano* **2017**, *4*, 1617; d) H. Y. Mao, S. Laurent, W. Chen, O. Akhavan, M. Imani, A. A. Ashkarran, M. Mahmoudi, *Chem. Rev.* **2013**, *113*, 3407.
- [4] a) K. H. Lee, H. S. Yu, S.-I. Kim, S. P. Moon, J.-Y. Hwang, S. W. Kim, *J. Alloys Compd.* **2019**, *790*, 93; b) L. Zhang, W. Liang, *J. Phys. Chem. Lett.* **2017**, *8*, 1517.
- [5] a) X. Feng, A. D. Schlüter, *Angew. Chem., Int. Ed.* **2018**, *57*, 13748; b) I. Castano, A. M. Evans, H. Li, E. Vitaku, M. J. Strauss, J.-L. Brédas, N. C. Gianneschi, W. R. Dichtel, *ACS Cent. Sci.* **2019**, *5*, 1892; c) A. Faghani, M. F. Gholami, M. Trunk, J. Müller, P. Pachfule, S. Vogl, I. Donskyi, M. Li, P. Nickl, J. Shao, M. R. S. Huang, W. E. S. Unger, R. Arenal, C. T. Koch, B. Paulus, J. P. Rabe, A. Thomas, R. Haag, M. Adeli, *J. Am. Chem. Soc.* **2020**, *142*, 12976; d) S. Park, Z. Liao, B. Ibarlucea, H. Qi, H.-H. Lin, D. Becker, J. Melidonie, T. Zhang, H. Sahabudeen, L. Baraban, C.-K. Baek, Z. Zheng, E. Zschech, A. Fery, T. Heine, U. Kaiser, G. Cuniberti, R. Dong, X. Feng, *Angew. Chem., Int. Ed.* **2020**, *59*, 8218.
- [6] a) P. van Assenbergh, E. Meinders, J. Geraedts, D. Dodou, *Small* **2018**, *14*, 1703401; b) Y. Ke, S. Ye, P. Hu, H. Jiang, S. Wang, B. Yang, J. Zhang, Y. Long, *Mater. Horiz.* **2019**, *6*, 1380; c) M. Drost, F. Tu, L. Berger, C. Preischl, W. Zhou, H. Gliemann, C. Wöll, H. Marbach, *ACS Nano* **2018**, *12*, 3825.
- [7] a) D. Cui, M. Ebrahimi, J. M. Macleod, F. Rosei, *Nano Lett.* **2018**, *18*, 7570; b) C. Tan, H. Zhang, *Nat. Commun.* **2015**, *6*, 7873; c) R. Dong, T. Zhang, X. Feng, *Chem. Rev.* **2018**, *118*, 6189.

- [8] M. Lackinger, *Polym. Int.* **2015**, *64*, 1073.
- [9] a) S. Kang, J. Lee, S. Ryu, Y. Kwon, K.-H. Kim, D. H. Jeong, S. R. Paik, B.-S. Kim, *Chem. Mater.* **2017**, *29*, 3461; b) J. D. Cojal González, M. Iyoda, J. P. Rabe, *Nat. Commun.* **2017**, *8*, 14717; c) D. Cui, M. Ebrahimi, F. Rosei, J. M. Macleod, *J. Am. Chem. Soc.* **2017**, *139*, 16732; d) D. P. Goronzy, M. Ebrahimi, F. Rosei, Arramel, Y. F., S. De Feyter, S. L. Tait, C. Wang, P. H. Beton, A. T. S. Wee, P. S. Weiss, D. F. Perepichka, *ACS Nano* **2018**, *12*, 7445; e) A. D. Stroock, R. S. Kane, M. Weck, S. J. Metallo, G. M. Whitesides, *Langmuir* **2003**, *19*, 2466.
- [10] O. Ourdjini, R. Pawlak, M. Abel, S. Clair, L. Chen, N. Bergeon, M. Sassi, V. Oison, J.-M. Debierre, R. Coratger, L. Porte, *Phys. Rev. B* **2011**, *84*, 125421.
- [11] a) G. Wei, Y. Zhang, S. Steckbeck, Z. Su, Z. Li, *J. Mater. Chem.* **2012**, *22*, 17190; b) J. Wang, Z. Ouyang, Z. Ren, J. Li, P. Zhang, G. Wei, Z. Su, *Carbon* **2015**, *89*, 20.
- [12] a) S. Abbina, S. Vappala, P. Kumar, E. M. J. Siren, C. C. La, U. Abbasi, D. E. Brooks, J. N. Kizhakkedathu, *J. Mater. Chem. B* **2017**, *5*, 9249; b) M. Calderón, M. A. Quadir, S. K. Sharma, R. Haag, *Adv. Mater.* **2010**, *22*, 190; c) H. Frey, R. Haag, *Rev. Mol. Biotechnol.* **2002**, *90*, 257.
- [13] C. Holzhausen, D. Gröger, L. Mundhenk, C. K. Donat, J. Schnorr, R. Haag, A. D. Gruber, *J. Nanopart. Res.* **2015**, *17*, 116.
- [14] a) Z. Tu, G. Guday, M. Adeli, R. Haag, *Adv. Mater.* **2018**, *30*, 1706709; b) Z. Tu, H. Qiao, Y. Yan, G. Guday, W. Chen, M. Adeli, R. Haag, *Angew. Chem., Int. Ed.* **2018**, *57*, 11198; c) Z. Tu, K. Achazi, A. Schulz, R. Mülhaupt, S. Thierbach, E. Rühl, M. Adeli, R. Haag, *Adv. Funct. Mater.* **2017**, *27*, 1701837.
- [15] a) I. S. Donskyi, W. Azab, J. L. Cuellar-Camacho, G. Guday, A. Lippitz, W. E. S. Unger, K. Osterrieder, M. Adeli, R. Haag, *Nanoscale* **2019**, *11*, 15804; b) M. F. Gholami, D. Lauster, K. Ludwig, J. Storm, B. Ziem, N. Severin, C. Böttcher, J. P. Rabe, A. Herrmann, M. Adeli, R. Haag, *Adv. Funct. Mater.* **2017**, *27*, 1606477; c) B. Ziem, J. Rahn, I. Donskyi, K. Silberreis, L. Cuellar, J. Dervede, G. Keil, T. C. Mettenleiter, R. Haag, *Macromol. Biosci.* **2017**, *17*, 1600499; d) B. Ziem, W. Azab, M. F. Gholami, J. P. Rabe, N. Osterrieder, R. Haag, *Nanoscale* **2017**, *9*, 3774; e) B. Ziem, H. Thien, K. Achazi, C. Yue, D. Stern, K. Silberreis, M. F. Gholami, F. Beckert, D. Gröger, R. Mülhaupt, J. P. Rabe, A. Nitsche, R. Haag, *Adv. Healthcare Mater.* **2016**, *5*, 2922.
- [16] a) V. Palmieri, M. Papi, *Nano Today* **2020**, *33*, 100883; b) C. Weiss, M. Carriere, L. Fusco, I. Capua, J. A. Regla-Nava, M. Pasquali, J. A. Scott, F. Vitale, M. A. Unal, C. Mattevi, D. Bedognetti, A. Merkoçi, E. Tasciotti, A. Yilmazer, Y. Gogotsi, F. Stellacci, L. G. Delogu, *ACS Nano* **2020**, *14*, 6383; c) S. Talebian, G. G. Wallace, A. Schroeder, F. Stellacci, J. Conde, *Nat. Nanotechnol.* **2020**, *15*, 618.
- [17] a) J. Lan, J. Ge, J. Yu, S. Shan, H. Zhou, S. Fan, Q. Zhang, X. Shi, Q. Wang, L. Zhang, X. Wang, *Nature* **2020**, *581*, 215; b) T. M. Clausen, D. R. Sandoval, C. B. Spliid, J. Pihl, C. D. Painter, B. E. Thacker, C. A. Glass, A. Narayanan, S. A. Majowicz, Y. Zhang, J. L. Torres, G. J. Golden, R. Porell, A. F. Garretson, L. Laubach, J. Feldman, X. Yin, Y. Pu, B. Hauser, T. M. Caradonna, B. P. Kellman, C. Martino, P. L. S. M. Gordts, S. L. Leibel, S. K. Chanda, A. G. Schmidt, K. Godula, J. Jose, K. D. Corbett, A. B. Ward, A. F. Carlin, J. D. Esko, *Biorxiv: the Preprint Server for Biology* **2020**, *183*, 1043.
- [18] Z. Tu, V. Wycisk, C. Cheng, W. Chen, M. Adeli, R. Haag, *Nanoscale* **2017**, *9*, 18931.
- [19] a) A. Setaro, M. Adeli, M. Glaeske, D. Przyrembel, T. Bisswanger, G. Gordeev, F. Maschietto, A. Faghani, B. Paulus, M. Weinelt, R. Arenal, R. Haag, S. Reich, *Nat. Commun.* **2017**, *8*, 14281; b) A. Faghani, I. S. Donskyi, M. Fardin Gholami, B. Ziem, A. Lippitz, W. E. S. Unger, C. Böttcher, J. P. Rabe, R. Haag, M. Adeli, *Angew. Chem., Int. Ed.* **2017**, *56*, 2675.
- [20] a) M. Dimde, D. Steinhilber, F. Neumann, Y. Li, F. Paulus, N. Ma, R. Haag, *Macromol. Biosci.* **2017**, *17*, 1600190; b) D. Steinhilber, T. Rossow, S. Wedepohl, F. Paulus, S. Seiffert, R. Haag, *Angew. Chem., Int. Ed.* **2013**, *52*, 13538.
- [21] G. Guday, I. S. Donskyi, M. F. Gholami, G. Algara-Siller, F. Witte, A. Lippitz, W. E. S. Unger, B. Paulus, J. P. Rabe, M. Adeli, R. Haag, *Small* **2019**, *15*, 1805430.
- [22] a) C. S. Campelo, P. Chevallier, J. M. Vaz, R. S. Vieira, D. Mantovani, *Mater. Sci. Eng. C* **2017**, *72*, 682; b) I. Donskyi, M. Drüke, K. Silberreis, D. Lauster, K. Ludwig, C. Kühne, W. Unger, C. Böttcher, A. Herrmann, J. Dervede, M. Adeli, R. Haag, *Small* **2018**, *14*, 1800189; c) M. Ferraro, K. Silberreis, E. Mohammadifar, F. Neumann, J. Dervede, R. Haag, *Biomacromolecules* **2018**, *19*, 4524.
- [23] P. Dey, T. Bergmann, J. L. Cuellar-Camacho, S. Ehrmann, M. S. Chowdhury, M. Zhang, I. Dahmani, R. Haag, W. Azab, *ACS Nano* **2018**, *12*, 6429.
- [24] a) S. Warner, C. A. Hartley, R. A. Stevenson, N. Ficorilli, A. Varrasso, M. J. Studdert, B. S. Crabb, *J. Virol.* **2001**, *75*, 9274; b) E. E. Fry, T. J. Tuthill, K. Harlos, T. S. Walter, D. J. Rowlands, D. I. Stuart, *J. Gen. Virol.* **2010**, *91*, 1971.
- [25] B. J. Reynwar, G. Illya, V. A. Harmandaris, M. M. Müller, K. Kremer, M. Deserno, *Nature* **2007**, *447*, 461.
- [26] S. Y. Kim, W. Jin, A. Sood, D. W. Montgomery, O. C. Grant, M. M. Fuster, L. Fu, J. S. Dordick, R. J. Woods, F. Zhang, R. J. Linhardt, *Antiviral Res.* **2020**, *181*, 104873.

ADVANCED FUNCTIONAL MATERIALS

Supporting Information

for *Adv. Funct. Mater.*, DOI: 10.1002/adfm.202009003

Graphene-Assisted Synthesis of 2D Polyglycerols as
Innovative Platforms for Multivalent Virus Interactions

*Ehsan Mohammadifar, Vahid Ahmadi, Mohammad
Fardin Gholami, Alexander Oehrl, Oleksandr
Kolyvushko, Chuanxiong Nie, Ievgen S. Donskyi, Svenja
Herziger, Jörg Radnik, Kai Ludwig, Christoph Böttcher,
Jürgen P. Rabe, Klaus Osterrieder, Walid Azab, Rainer
Haag,* and Mohsen Adeli**

Supporting Information

Graphene-Assisted Synthesis of Two-Dimensional Polyglycerols as Innovative Platforms for Multivalent Virus Interactions

*Ehsan Mohammadifar,^{1, †} Vahid Ahmadi,^{1, †} Mohammad Fardin Gholami,² Alexander Oehrl,¹ Oleksandr Kolyvushko,³ Chuanxiong Nie,¹ Ievgen S. Donskyi,^{1, 4} Svenja Herziger,⁵ Jörg Radnik,⁴ Kai Ludwig,⁵ Christoph Böttcher,⁵ Jürgen P. Rabe,² Klaus Osterrieder,^{3, 6} Walid Azab,³ Rainer Haag^{1, *}, Mohsen Adeli^{7, *}*

¹ Institut für Chemie und Biochemie, Freie Universität Berlin, Takustrasse 3, 14195 Berlin, Germany

² Department of Physics & Integrative Research Institute for the Sciences IRIS Adlershof, Humboldt-Universität zu Berlin, Newtonstrasse 15 & Zum Großen Windkanal 2, 12489 Berlin, Germany

³ Institut für Virologie, Robert von Ostertag-Haus, Zentrum für Infektionsmedizin, Freie Universität Berlin, Robert-von-Ostertag-Str. 7-13, 14163 Berlin, Germany

⁴ BAM–Federal Institute for Material Science and Testing Division of Surface Analysis and Interfacial Chemistry Unter den Eichen 44–46, 12205 Berlin, Germany

⁵ Forschungszentrum für Elektronenmikroskopie and Core Facility BioSupraMol, Institut für Chemie und Biochemie Freie Universität Berlin, Fabeckstrasse 36a, 14195 Berlin, Germany

⁶ Department of Infectious Diseases and Public Health, Jockey Club College of Veterinary Medicine and Life Sciences, City University of Hong Kong, Kowloon Tong, Hong Kong

⁷ Department of Chemistry, Faculty of Science, Lorestan University, Khorramabad, Iran

[†] E. M. and V. A. contributed equally.

Contents

1	Experimental	3
1.1	Materials	3
1.2	Methods and Instrumentations	3
2	Synthetic procedures	7
2.1	Synthesis of 3-(4-(dimethoxymethyl)phenoxy)propan-1-amine) DMPA(5)	7
2.1.1	Azidopropanol.....	7
2.1.2	Synthesis of 3-azidopropyltoluenesulfonate.....	8
2.1.3	4-(3-azidopropoxy)benzaldehyde.....	8
2.1.4	1-(3-azidopropoxy)-4-(dimethoxymethyl)benzene	9
2.1.5	3-(4-(dimethoxymethyl)phenoxy)propan-1-amine (DMPA)	9
2.2	Synthetic approach to 2D-hPGS	10
2.2.1	Synthesis of triazine-functionalized TRGO (G-Trz).....	10
2.2.2	G-linker	10
2.2.3	Synthesis of 10% azide-functionalized hPG (hPG-N ₃ (10%))	10
2.2.4	Synthesis of G-hPG	12
2.2.5	Synthesis of two-dimensional polyglycerol (2D-hPG).....	12
2.2.6	Control reaction (to prove the role of graphene template).....	12
2.2.7	Control reactions to prove the role of temperature to forward tripropargylamine molecules from graphene template to azide groups of hPG.....	14
2.3	Synthesis of three-dimensional Polyglycerol and three-dimensional sulfated Polyglycerol nanogels (3D-hPG and 3D-hPGS).....	14
3	Characterization	16
4	Calculation of IC ₅₀ in molarity	23
5	References.....	24

1 Experimental

1.1 Materials

Thermally reduced graphene oxide (TRGO) was prepared by Mülhaupt et al. according to areported method in literature.¹ Hyperbranched polyglycerol (hPG), $\bar{M}_n \approx 10$ KDa and PDI= 1.4, was synthesized by ring-opening anionic polymerization according to literature.² Cyanuric chloride, triethylamine (TEA), sodium azide, palladium on activated carbon (Pd/C), sulfur trioxide pyridine complex, tetrabutylammonium hydrogensulfate (TBAHSO₄), 4-toluenesulfonyl chloride (TsCl), p-hydroxybenzaldehyde (pHBA), trimethyl orthoformate (TMOF), cyanuric chloride, tripropargylamine, sodium ascorbate, sulfur trioxide pyridine complex (SO₃Py), N-methyl-2-pyrrolidon (NMP), N,N-dimethylformamide (DMF), tetrahydrofuran (THF), p-toluenesulfonic acid (PTSA), tripropargylamine, sodium ascorbate, copper (II) sulfate pentahydrate (CuSO₄·5H₂O) were purchased from Sigma-Aldrich and used directly without further purification.

1.2 Methods and Instrumentations

¹H NMR and ¹³C NMR spectra were recorded on a Jeol Eclipse 400 MHz in deuterated solvent peak at 295 K. The chemical shifts were reported in ppm. FTIR spectra data were collected on a Jasco FT/IR-4100 Spectrometer from 4000 to 650 cm⁻¹. TGA was recorded on Linseis STA PT 1600 and evaluated with Linseis Data Acquisition software. The measurements conducted at temperatures ranging from 25 °C to 800 °C with 10 K/min heating rate under argon gas. Zeta potential data were obtained by NANO ZSPO (Malvern) in PBS solution. Elemental analysis (EA) was measured using ELEMENTAR apparatus with three columns and detector for carbon, nitrogen, hydrogen, and sulfur elements. For TEM measurements, droplets of the sample solution (5 µL) were applied on hydrophilized Formvar®-supported carbon-coated copper grids (400 mesh) for 30 s. Hydrophilization was achieved beforehand by 60 s glow discharging in a BALTEC MED 020 (BALTEC, Liechtenstein) at 8 W. The supernatant fluid was removed by blotting with a filter paper. Measurements were carried out using a TALOS L120C electron microscope (Thermo Fisher Scientific Inc., Waltham, Massachusetts, USA). The microscope was equipped with a LaB6 cathode and operated at 120 kV accelerating voltage. Micrographs were acquired on a FEI Ceta CMOS camera (Thermo Fisher Scientific Inc., Waltham, Massachusetts,

USA) at a nominal magnification of either 4300x (overviews) or 36,000x, corresponding to a calibrated pixel size of 4.09 Å/pixel in the latter case.

For X-ray photoelectron spectroscopy (XPS) experiments, gold substrates for XPS analysis were cleaned in a piranha solution (1:4) 30% H₂O₂ / 98% H₂SO₄ (v/v) during ultrasonication at room temperature for 10 min. Then they were washed with the DI water 5 times and with acetone 2 times. After drying overnight, the studied compounds were dispersed in methanol and evenly distributed dropwise across the surface of gold substrates. XPS spectra were recorded using a Kratos Axis Ultra DLD spectrometer equipped with a monochromatized Al K α X-ray source (1486.69 eV) using an analyzer pass energy of 80 eV for survey spectra that were used for quantification. High-resolution, core-level O1s, C1s, and N1s spectra were recorded in FAT (fixed analyzer transmission) mode at a pass energy of 20 eV. The electron emission angle was 0° and the source-to-analyzer angle was 60°. The binding energy scale of the instrument was calibrated following a Kratos analytical procedure that used ISO 15472 binding energy data. Spectra were recorded by setting the instrument to the hybrid lens mode and the slot mode providing approximately a 300 x 700 μm^2 analysis area and using charge neutralization. All XPS spectra were processed with the UNIFIT program (version 2017). A Gaussian/Lorentzian product function peak shape model GL (30) was used in combination with a Shirley background. If not otherwise denoted, the L-G mixing for component peaks in all spectra were constrained to the value of 0.39. Peak fitting of C1s spectra was performed by using an asymmetric peak shape model for the graphene C1s component peak and a symmetric peak shape model for all other component peaks. In the case of polymer samples, the symmetric peak shape model was used for all component peaks. After peak fitting of the C1s spectra, all binding energies were calibrated in reference to the graphene C1s component at a binding energy of 284.6 eV (285.0 eV in the case of polymer samples).

In order to record SEM images, samples were dissolved in distilled H₂O and cast on clean silica surface and then imaged by HR-SEM (Hitachi SU8030, Japan).

Scanning force microscopy (SFM) was carried out using two modes, namely, Quantitative Imaging Mode (SFM-QI) and Tapping Mode (TM-SFM). SFM-QI was mainly used to characterize the height of the 2D-hPGS and 3D-hPGS. TM-SFM in combination with SFM-QI was used for determining the lateral size distributions of the particles. Samples were prepared by depositing a 10 μl droplet of an aqueous 2D-hPGS solution (0.1 to 0.5 mg/ml) onto a freshly

cleaved mica surface and casting it for 5 minutes along with spinning it until complete removal of excess solution.

To evaluate the sheet size two SFMs had been used, a Nanowizard III (JPK GmbH) and a Multimode 8, Nanoscope V (Bruker Corporation). Multimode 8 was operated with an E-scanner in tapping mode at a typical rate of 5 min per image and an image resolution of 512×512 pixels. Nanowizard III was operated in quantitative imaging mode (QI) at a typical rate of 10–17 min per image and an image resolution of 128×128 pixels. The contact, i.e., zero force point on extension curves in QI mode, was assigned to the topography. Silicon tips on silicon nitride cantilevers with a tetrahedral base were used with a typical resonance frequency of 70 kHz and a spring constant of 2 N m^{-1} . The tips exhibited a typical apex radius of 7 nm with an upper limit of 10 nm, having a tip cone half angle of 18° , as specified by the manufacturer (Olympus Corporation). Experiments were carried out under ambient conditions. Deflection sensitivity was calibrated by acquiring force–distance curves on a sapphire surface (Bruker Corporation). Cantilever spring constants were calibrated using the thermal noise method. Set points in the range of 0.5–2 nN were used. TM-SFM images were processed and analyzed with SPIP (Image Metrology A/S) and JPK image processing software. Topography images were line flattened with a first order polynomial.

Raman spectroscopy was carried out as a characterization method to ensure removal of TRGO content after cleaving the 2D-hPG from templates. 2D-hPG bulk quantity was surveyed in addition to the TRGO sheets at more than 50 spots after its deposition onto freshly cleaved mica surface. Spectra were measured using a 10X objective (Olympus) at 532 nm, with an Xplora one (Horiba) Raman spectrometer with $\sim 1.7 \text{ cm}^{-1}$ spectral resolution and power well lower than $\sim 1 \text{ mW}$. Gratings of 1800 and 2400 grooves/mm were used in the setup. Special care was taken to assure that the accumulation times and laser power used, improve the signal to noise ratio, but do not adversely affect the graphene flakes, i.e. preventing from thermally induced effects.³

Cells and Viruses

African green monkey kidney cells (Vero E6), rabbit kidney cells (RK-13), and bovine dermal cells (BD) were used as competent cells for Herpes simplex virus type 1 (HSV-1), equine rhinitis A virus (ERAV) and equine arteritis virus (EAV), respectively. HSV-1 bacterial artificial

chromosome⁴ was kindly provided by Dr. Yasushi Kawaguchi, Institute of Medical Science, The University of Tokyo. The virus was reconstituted on Vero E6 cells using Lipofectamine 2000 (Invitrogen). The enhanced green fluorescent protein (EGFP) gene is integrated into the virus genome to facilitate detection of virus replication in infected cells. Each cell line was grown in MEM (PAN Biotech P04-08050), with 10% (v/v) of fetal calf serum (FCS, PAN Biotech P30-1402), 100 U/mL penicillin (Roth CN28.3) and 100 µg/mL streptomycin (Alfa Aesar J61299) at 37 °C and 5% CO₂ atmosphere.

Cell Viability Assay

Cytotoxic effects of nanosheets (in concentrations of 10, 50, 100, and 200 µg/mL on Vero E6 cells) was measured using WTS-1 assay after 24 hours. In short, confluent cells in 96-well plate were overlaid with media containing nanosheets. EMEM was used as a negative control. To generate positive control, cells were treated with 30% solution of hydrogen peroxide (Sigma No. H1009) for 1 minute. After 24 hours of incubation, WTS-1 reagent (Cayman Chemicals No. 10008883) was added to the media of each well. After 2 hours, absorbance at 450 nm was measured for each sample using a microplate reader.

Flow Cytometry

The cells were infected by HSV-1 (MOI 1) in the presence of nanosheets and nanogels. Range of concentration of 1, 10, 20, 50, 100, and 200 µg/mL were used to infect confluent Vero E6 cells in a 96 well plate with an MOI of 1. After 20 hours, infected cells were trypsinized and washed with cold PBS. Total 20 000 cells resuspend in PBS were analyzed with CytoFLEX flow cytometer (Beckman Coulter) to measure the proportion of infected cells by fluorescent emission. Flow cytometry reading was analyzed with FlowJo software, where the identical gates were applied for all the samples.

Plaque Reduction Assay for HSV-1

Vero E6 cells were grown to in 24-well plate and infected for 1 hour with 50 PFU per well of HSV-1 in media or media containing 50 µg/mL of sulfated nanosheets or non-sulfated nanosheets. Subsequently the cell monolayer was washed with PBS. Low pH treatment was used to eliminate all free virus particles, followed by PBS washing, and finally MEM with 0.5%

methylcellulose (Sigma M0262) was overlaid on cells. At 48 h post infection, the number of plaques was quantified with inverted fluorescence microscope (Zeiss Axiovert 100). Three independent experiments were performed, with 4 wells for each treatment.

TCID50 of EAV and ERAV

Serial 10-fold dilutions of each virus were prepared in media or media containing 50 µg/mL of nanosheets and added to the competent cell line. After 4 days cells were fixed with 4% PFA, stained with crystal violet to detect cytopathic effect. Titer of the virus (TCID50/mL) was calculated with the Spearman-Kärber algorithm. Results are averages of 3 independent experiments; 8 wells were infected with each dilution.

Plaque Reduction Assay for SARS-CoV-2

SARS-CoV-2 München (SARS-CoV2M; BetaCoV/Germany/BavPat1/2020) was propagated in Vero E6 cells and titrated via plaque assay.⁵ For a plaque reduction assay, Vero E6 cells were grown into 24-well plate and infected for 1 hour with 300 PFU per well of SARS-CoV-2 in media in the presence of 2D-hPGS and 3D-hPGS. The cells were washed with PBS and cultured in DMEM media with MEM with 0.5% methylcellulose for 2 days. After being fixed by 2.5% formaldehyde, the cells were stained by 1% crystal violet. The experiment was performed within the BSL3 lab in Institut für Virologie, Freie Universität Berlin.

Statistical Analysis

Cell viability, TCID50, plaque assay, and flow-cytometry-based studies were analyzed with GraphPad software. ANOVA analysis was done, all values were compared to the control and Duntett's correction for multiple comparisons was used. Significance value was set to $p=0.05$.

2 Synthetic procedures

2.1 Synthesis of 3-(4-(dimethoxymethyl)phenoxy)propan-1-amine) DMPA(5)

2.1.1 Azidopropanol

Azidopropanol was synthesized according to reported procedure in literature.⁶ In a 100 mL round-bottom flask TBAHSO₄ (350 mg, 1.04 mmol) and sodium azide (18 g, 276 mmol, 2 eq) were dissolved in 30 mL of deionized water and heated to 80 °C. 3-chloropropanol (14 g, 148

mmol, 1 eq.) was then added to this reaction flask and the mixture was stirred at 80 °C for 24 h. The reaction was then cooled to room temperature and transferred to a separation funnel. The combined organic phases of 3 extractions with each 100 mL diethyl ether were dried over Na₂SO₄. After filtration the solvent was removed under reduced pressure and the crude product was purified via vacuum distillation (50 °C, ~ 10⁻¹ mbar). The product was obtained as a colorless liquid (12.87 g, 127 mmol, 86%).

¹H-NMR (400 MHz, CDCl₃): δ = 3.75 (dd, *J* = 7.2, 4.7 Hz, 2 H, -CH₂-OH), 3.45 (t, *J* = 6.6 Hz, 2 H, -CH₂-N₃), 1.92 – 1.78 (m, 2 H, OHCH₂-CH₂-CH₂N₃) ppm.

2.1.2 Synthesis of 3-azidopropyltoluenesulfonate

3-azidopropyltoluenesulfonate was synthesized according to reported procedures in literature ⁷. In a 100 mL round bottom flask azidopropanol (3 g, 29.7 mmol, 1 eq.) together with triethylamine (9.1 mL, 65.3 mmol, 2.2 eq.) were dissolved in dichloromethane (DCM) (30 mL). The solution was then cooled in an ice bath to 0 °C and TsCl (6.2 g, 32.6 mmol, 1.1 eq) dissolved in DCM (30 mL) was added dropwise over 15 min. The reaction was then stirred at ambient temperature for 22 h and quenched with saturated NH₄Cl aqueous solution (40 mL). The organic phase was washed twice with saturated NH₄Cl aqueous solution (40 mL) and twice with deionized water (40 mL). After separation the organic phase was dried using MgSO₄, filtered and the solvent was removed under reduced pressure. Purification of the crude product was performed using column chromatography with hexane and ethyl acetate (6:1) as the eluent. The product was obtained as a pale-yellow oil (4.98 g, 67%).

¹H-NMR (400 MHz, CDCl₃): δ = 7.84 – 7.70 (m, 2 H, H_{ar}), 7.36 (dt, *J* = 8.0, 0.7 Hz, 2 H, H_{ar}), 4.10 (t, *J* = 6.0 Hz, 2 H, -CH₂-OSO₃R), 3.37 (t, *J* = 6.5 Hz, 2 H, N₃CH₂-R), 2.45 (s, 3 H, R-CH₃), 1.99 – 1.77 (m, 2 H, N₃CH₂-CH₂-CH₂OSO₃R) ppm.

2.1.3 4-(3-azidopropoxy)benzaldehyde

4-(3-azidopropoxy)benzaldehyde was synthesized according to reported procedure in literature ⁷. In a 100 mL round-bottom flask pHBA (1.7 g, 14.1 mmol, 1.2 eq.) and 3-azidopropyltoluenesulfonate (3.0 g, 11.8 mmol, 1 eq.) were dissolved in acetone (40 mL). K₂CO₃

(9.7 g, 70.5 mmol, 6 eq.) was added to the mixture and the suspension was refluxed for 20 h. Then mixture was filtered and solvent was removed under reduced pressure. The remaining oil was dissolved in DCM (100 mL) and washed three times with deionized water (30 mL each). The organic phase was then dried over MgSO₄, filtered, and concentrated under reduced pressure. After purification with column chromatography (hexanes/ethylacetate 2:1, R_f = 0.6) the product was obtained as a pale-yellow liquid (1.5 g, 7.3 mmol, 62%).

¹H-NMR (400 MHz, chloroform-*d*): δ = 9.88 (s, 1 H, R-CHO), 7.83 (d, *J* = 8.8 Hz, 2H), 7.10 – 6.86 (m, 2H), 4.13 (dd, *J* = 7.5, 4.3 Hz, 2H), 3.53 (t, *J* = 6.5 Hz, 2H), 2.22 – 2.01 (m, 3H).

2.1.4 1-(3-azidopropoxy)-4-(dimethoxymethyl)benzene

1-(3-azidopropoxy)-4-(dimethoxymethyl)benzene was synthesized according to reported procedures in literature.⁷ In a 25 mL round-bottom flask 4-(3-azidopropoxy)benzaldehyde (1.37 g, 6.7 mmol, 1 eq.) and TMOF (3.7 mL, 30.4 mmol, 5 eq.) were dissolved in dry MeOH (15 mL). The solution was degassed three times using freeze-pump-thaw cycles. Upon addition of pTSA (120 mg, 0.7 mmol, 0.1 eq.) under argon atmosphere, the solution turned pink. The reaction mixture was then refluxed for 22 h until the solution turned orange. After cooling to room temperature, the reaction was quenched with 7 N NH₃ solution in MeOH (1.5 mL). The solvent was removed under reduced pressure and the remaining solid was re-dissolved in EtOAc (100 mL), washed three times with 50 mL water each, and dried over MgSO₄. After filtration and removal of EtOAc, the product was obtained as a red liquid (1.62 g, 94 %). Mass-ESI: [M+Na⁺] = 274.11 (cal.: [M+Na⁺] = 274.12).

¹H-NMR (400 MHz, methanol-*d*₄): δ = 7.50 – 7.19 (m, 2 H, H_{ar}), 6.92 (d, *J* = 8.8 Hz, 2 H, H_{ar}), 5.32 (s, 1 H, RCH(OMe)₂), 4.06 (t, *J* = 6.0 Hz, 2 H, -CH₂-O-C₆H₅-R), 3.51 (t, *J* = 6.7 Hz, 2 H, N₃-CH₂-R), 3.29 (s, 6 H, R-O-CH₃), 2.12 – 1.93 (m, 2 H, N₃-CH₂-CH₂-CH₂-O-C₆H₅-R).

2.1.5 3-(4-(dimethoxymethyl)phenoxy)propan-1-amine (DMPA)

In a 30 mL glass vial, 1-(3-azidopropoxy)-4-(dimethoxymethyl)benzene (1 g, 6.7 mmol, 1 eq.) was dissolved in cyclohexane (20 mL). Catalytic amounts of Pd/C were added and the solution was stirred in a hydrogen reactor at room temperature at a hydrogen overpressure of 4 bar. The reaction was monitored with TLC and stopped after full conversion. After syringe filtration

(PTFE 0.45 μm) the solvent was evaporated and the product was obtained without further purification as a yellow liquid. Mass-ESI: $[\text{M}+\text{Na}^+] = 248.12$ (cal.: $[\text{M}+\text{Na}^+] = 248.13$).

$^1\text{H-NMR}$ (400 MHz, chloroform-*d*): $\delta = 7.36 - 7.27$ (m, 2H), 6.90 – 6.79 (m, 2H), 5.30 (s, 1H), 4.00 (td, $J = 6.1, 2.6$ Hz, 2H), 3.26 (s, 6H), 2.93 – 2.77 (m, 2H), 1.99 – 1.80 (m, 2H), 1.68 (s, 2H).

2.2 Synthetic approach to 2D-hPGS

2.2.1 Synthesis of triazine-functionalized TRGO (G-Trz)

G-Trz was prepared according to our previous reported procedure.⁸ Cyanuric chloride 10 g (54 mmol) was dissolved in NMP (10 mL) and subsequently sodium azide (3.5 g, 54 mmol), dispersed in the same solvent (30 mL), was added to this solution at 0 °C. The mixture was stirred for 45 minutes and added to TRGO (0.280 g), dispersed in NMP (100 mL). Mixture was stirred at 0 °C and 80 °C for 2 h and 24 h, respectively. Meantime, the solution was sonicated several times and argon was bubbled into it in the intervening time. Following centrifuging at 10,000 rpm for 10 min, the precipitated product was washed four times with THF, acetone, and water, respectively. Finally, the compound was dried by lyophilizer. Yield (62%).

2.2.2 G-linker

In a 250 mL round-bottom flask, G-Trz (30 mg) was dispersed in dry DMF (30 mL). Argon was bubbled in the solution for 20 minutes. Then flask was sealed and fixed in a sonication bath for 30 minutes. Afterwards, DMPA (230 mg, 1.02 mmol) dissolved in dry DMF and 100 μL of TEA were added to the solution. The mixture was stirred for 48 h at room temperature. Product was obtained after 2 days dialysis against methanol.

2.2.3 Synthesis of 10% azide-functionalized hPG (hPG-N₃(10%))

hPG-N₃(10%) was synthesized according to reported procedure in literature.⁹ Briefly, hPG (Mn = 10 kDa) was first mesylated and then converted to azide using sodium azide. (Mn=10 kDa, PDI=1.4).

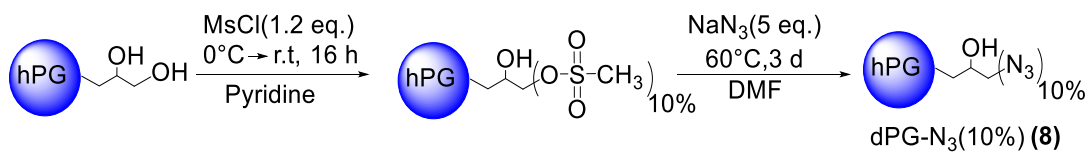


Figure S1. Synthetic route for the preparation of hPG-N₃(10%)

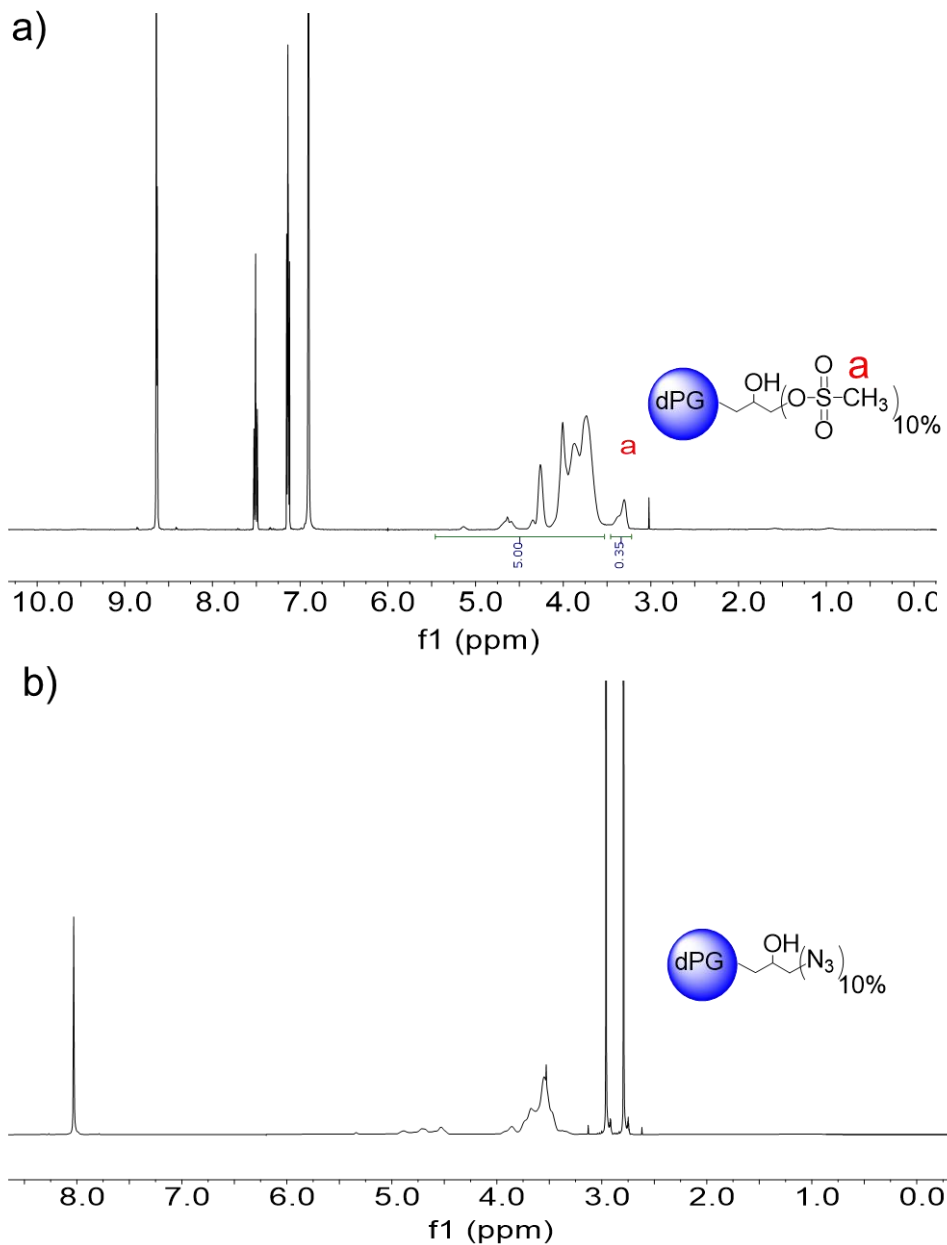


Figure S2. The ¹H NMR spectra of (a) hPG-OMS (10%) and (b) hPG-N₃(10%)

2.2.4 *Synthesis of G-hPG*

G-linker (50 mg) was dispersed in dry DMF (90 mL) and stirred overnight. Then mixture was sonicated for 15 minutes and hPG-N₃ (10%) (450 mg, 0.045 mmol) dissolved in dry DMF (20 mL) and PTSA (67 mg, 0.39 mmol) were added to the mixture and stirred for 6 h at room temperature. Vacuum was applied every 30 minutes to remove the produced methanol. Thereafter, the dried compound was obtained by lyophilizing after 2 days dialysis (100 KDa cut-off) against water: methanol (1:2). During dialysis, the pH of the medium was kept around 8-9 by adding ammonium.

2.2.5 *Synthesis of two-dimensional polyglycerol (2D-hPG)*

G-hPG (380 mg) was suspended in a mixture of DMF:water (1:1) (250 mL). Then mixture was sonicated and bubbled with argon for 15 minutes. Tripropargylamine (1.0 ml, 0.007 mmol), sodium ascorbate (72 mg, 0.36 mmol), and CuSO₄·5H₂O (48 mg, 0.19 mmol) were added to the reaction and stirred at 50 °C overnight. Later, the same amount of sodium ascorbate and CuSO₄·5H₂O were added to the reaction again and stirred for two more days. Every 12 h, the mixture was sonicated for 15 minutes. Then, the pH of solution was adjusted at 3 and stirred for three more days. Finally, the mixture was centrifuged 3 times at 10,000 rpm for 45 minutes to separate the cleaved graphene. The supernatant was dialyzed (100 KDa cutoff) against water for 2 days and stored in the fridge.

2.2.6 *Control reaction (to prove the role of graphene template)*

The same reaction, as for preparation of 2D-hPG, was repeated but without graphene template. This was a control reaction for the investigation of role of graphene template in the preparation of 2D-hPG. Briefly, hPG-N₃ (10%) (350 mg, 0.035 mmol) was dissolved in a mixture of DMF:water (1:1) (250 mL). The mixture was sonicated and bubbled with argon for 15 minutes. Tripropargylamine (1.0 ml, 0.007 mmol), sodium ascorbate (72 mg, 0.36 mmol), and CuSO₄·5H₂O (48 mg, 0.19 mmol) were added to the reaction and stirred at 50 °C overnight. Later, the same amount of sodium ascorbate and CuSO₄·5H₂O were added to the reaction again and stirred for two more days. Every 12 h, the mixture was sonicated for 15 minutes. Then, the pH of solution was adjusted at 3 and stirred for three more days. Finally, the mixture was centrifuged 3 times at 10,000 rpm for 45 minutes to separate the cleaved graphene. The

supernatant was dialyzed (100 KDa cutoff) against water for 2 days and tested with SFM. No object was found with aspect ratio compared to nanosheets (see **Figure S3**).

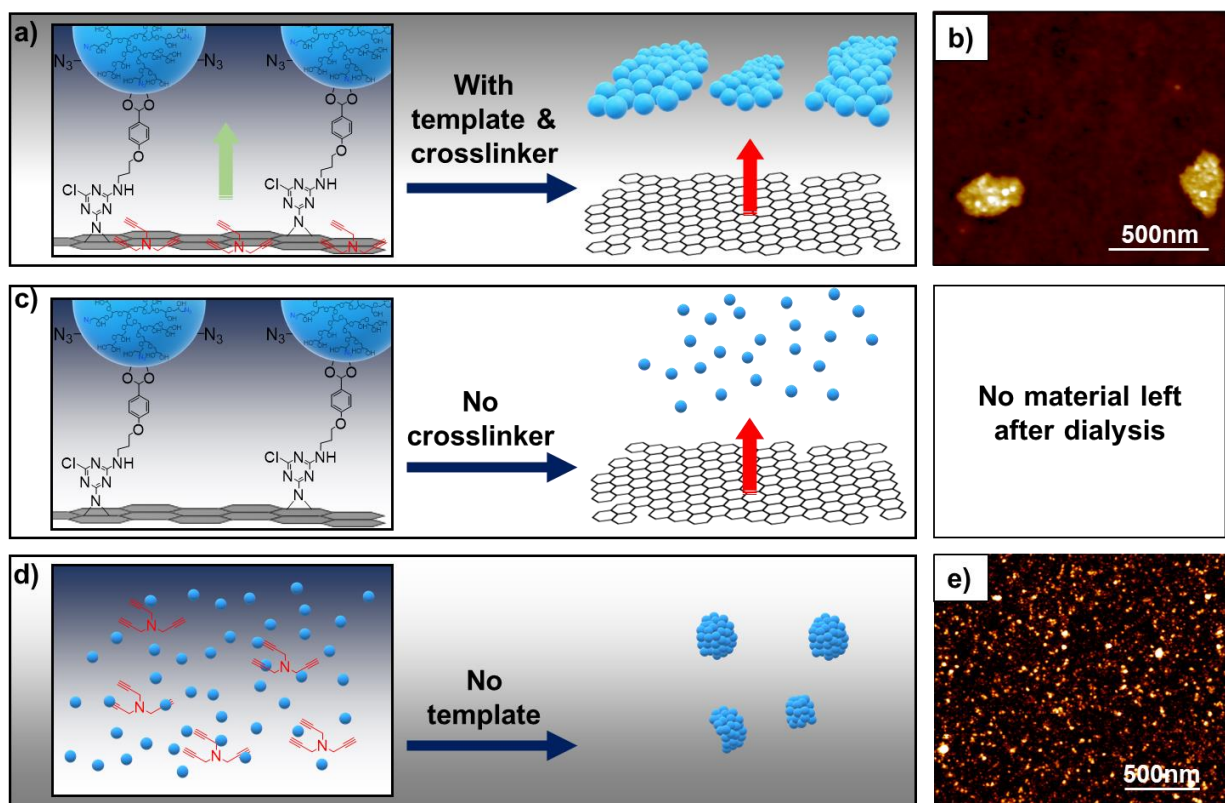


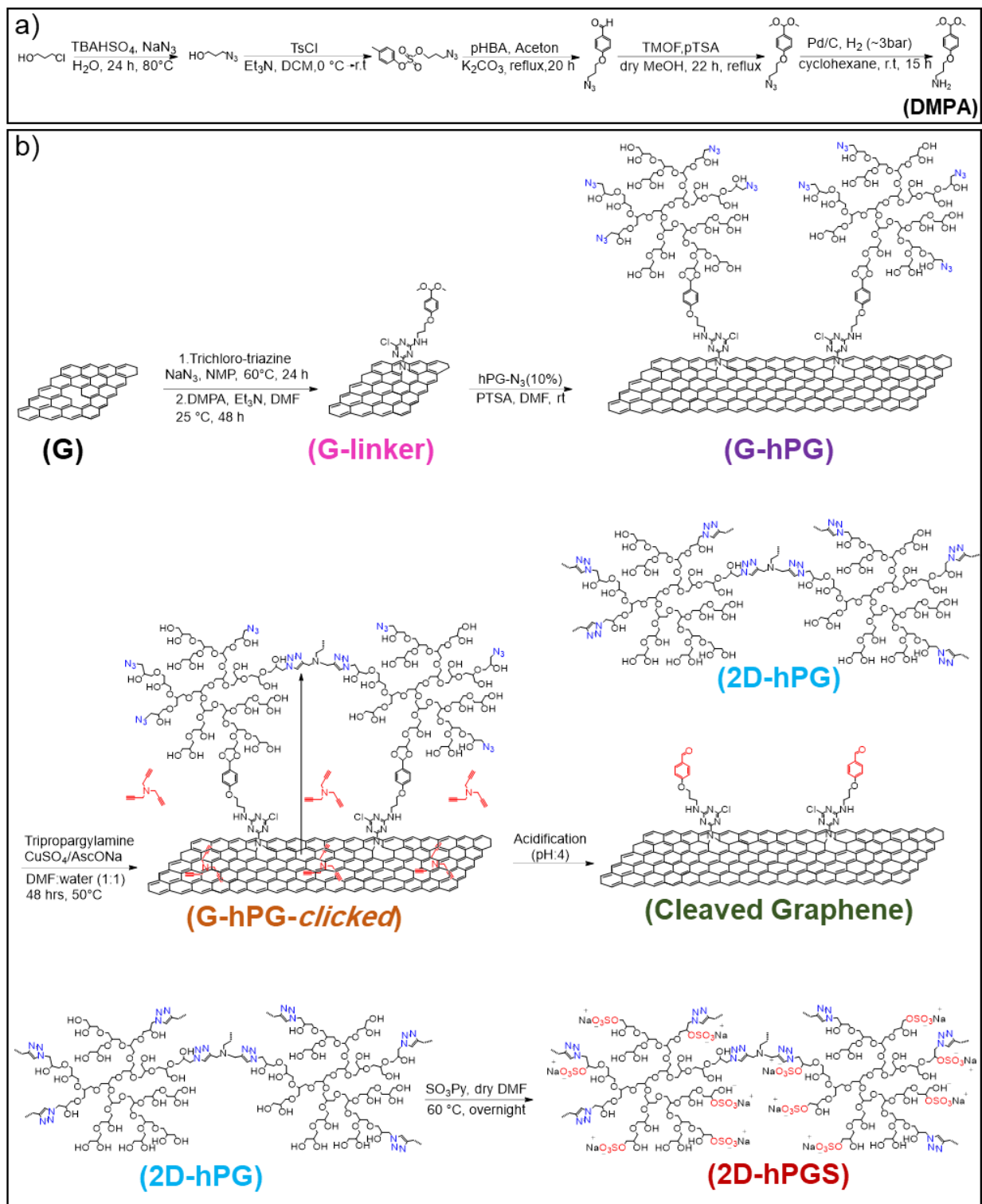
Figure S3. Schematic representation of the role of crosslinker and template in the synthesis of 2D-hPG. (a) Crosslinking of polyglycerol branches that are conjugated to the surface of graphene platform by tripropargylamine resulted in 2D-hPG. Loading of tripropargylamine on the surface of graphene by π - π interactions and releasing this reagent toward azide groups of polyglycerol branches by increasing the temperature is the key point in the synthesizing of 2D-hPG. (b) SFM image of 2D-hPG deposited onto muscovite mica surface. (c) Elimination of the crosslinker in this process and cleaving polyglycerol coverage did not result in any detectable polyglycerol nanostructure. (d) Elimination of graphene platform resulted in unregularly three-dimensional objects.

2.2.7 Control reactions to prove the role of temperature to forward tripropargylamine molecules from graphene template to azide groups of hPG

In order to check the role of temperature to forward tripropargylamine molecules loaded on the surface of graphene to azide groups of hPG branches the same reaction, as for preparation of 2D-hPG, was performed at room temperature and 80 °C (see **Figure 6**).

2.3 Synthesis of three-dimensional Polyglycerol and three-dimensional sulfated Polyglycerol nanogels (3D-hPG and 3D-hPGS)

3D-hPG and 3D-hPGS were synthesized as described in literature.¹⁰ Briefly, hPG-macromonomers were separately dissolved in water to obtain stock solutions. A ratio of 1:1.5 azide:BCN and a total macromonomer concentration of 5 mg/mL in water were used. Prior to the inverse nanoprecipitation, the solutions were cooled to 4 °C. Aliquots of hPG-BCN and hPG-azide (or hPGS-azide/hPG-BCN; hPG-benzacetal-BCN/hPG-azide; hPGS-azide/hPG-benzacetal-BCN) were diluted to a total volume of 3.5 mL with one macromonomer dissolved in x mL water and the other macromonomer dissolved in 3.5 – x mL. Both solutions were then combined, shortly vortexed for 3 s and added fast via syringe to magnetically (1200 rpm) stirred acetone (800 mL). After stirring for another 3 s, the dispersion was kept still for 2 hours and then quenched with azido glycerol (100 µL). After another 12 hours, water was added (200 mL) and the acetone was removed under reduced pressure. The gels were purified via centrifugal filtration with a molecular weight cut-off of 1 MDa at 234 rcf and obtained as stable aqueous dispersions.



Scheme S1. (a) Synthesis of pH-sensitive linker (DMPA) and (b) synthetic route for the production of 2D-hPG and 2D-hPGS.

3 Characterization

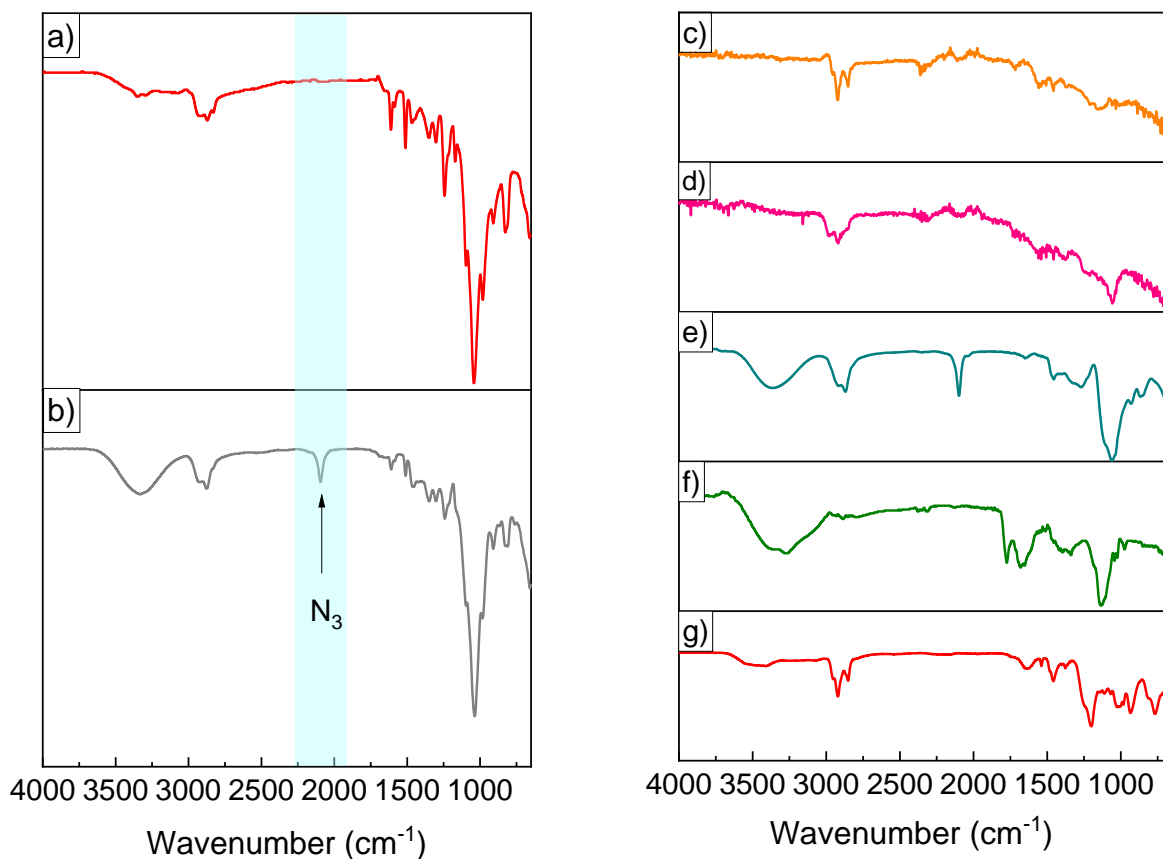


Figure S4. IR spectra of (a) DMPA, (b) 1-(3-azidopropoxy)-4-(dimethoxymethyl)benzene, (c) G-Trz, (d) G-linker, (e) hPG-N₃(10%), (f) G-hPG-*clicked*, and (g) 2D-hPGS.

Table S1. Elemental analysis of Graphene and G-Trz.

Compound	C (%)	H (%)	N (%)	S (%)
G	80.5	1.9	0.0	0
G-Trz	77.6	2.6	7.0	0
G-linker	77.4	2.7	4.4	0

- Degree of functionalization of triazine (DF) based on nitrogen content measured by EA:

$$(\text{DF}) = \frac{\text{N}(\%)}{\text{N}(\%) + \text{C}(\%)} \times 100$$

Equation S 1

*. indicated by nitrogen content in EA.

** indicated by carbon content in EA.

Mass of a building block of G-Trz (X):

$$(X) = \text{-----} \quad \text{Equation S 2}$$

$$(DF) = \text{-----} \quad \text{Equation S 3}$$

- Degree of functionalization of triazine (DF) based on mass loss measured by TGA:

X 163.5 (Mass of the one triazine group on the graphene surface)

100 21.7 (Mass loss of the G-Trz)

X= 753.4 (Mass of a building block of G-Trz)

753.4-163.5=589.9

DF=589.9/12=49.2

Table S2. Elemental analysis of G-hPG, 2D-hPG and 2D-hPGS.

Compound	C (%)	H (%)	N (%)	S (%)
G-hPG	50.5	6.9	5.1	N/A
2D-hPG	46.3	6.7	5.0	N/A
2D-hPGS	30.6	6.3	3.7	8.6

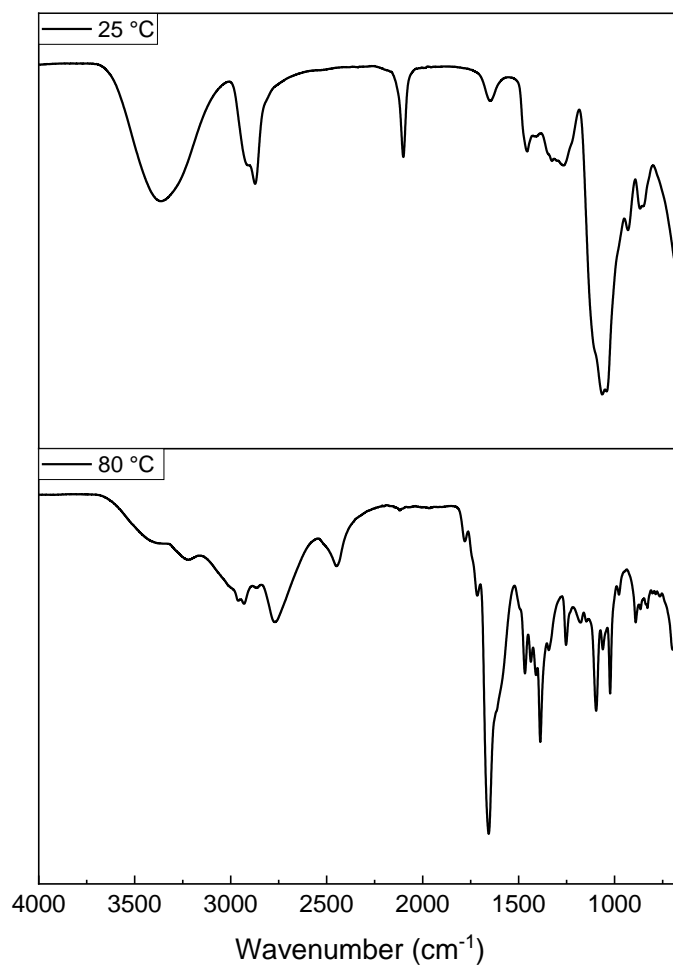


Figure S5. IR spectra of control reaction at 25 °C and 80 °C.

Table S3. Atomic ratios of the elements in the XPS survey spectra.

Sample	O/C ratio	N/C ratio	C at%
G	0.08	n.d.	92.0
G-Trz	0.08	0.06	87.2
G-linker	0.12	0.05	84.7
G-hPG	0.43	0.05	67.1
2D-hPG	0.53	0.08	61.9
2D-hPGS	0.34	0.03	69.1

Table S4. Fitting parameters of XPS spectra of G, G-Trz, G-linker, G-hPG, 2D-hPG, and 2D-hPGS.

Sample	Spectrum	Binding energy	L-G Mixing	FWHM M	Interpretation	Abs. Area	Relat. Area
G	C1s	284.6	0.39	0.8	C-C/C=C	29348	0.80
		285.4	0.39	1.0	C-O-C	3521	0.10
		286.3	0.39	1.0	C-O-H	2851	0.08
		291.3	0.39	1.0	$\pi-\pi^*$ shake ups	312	0.01
G-Trz	C1s	284.6	0.39	0.8	C-C/C=C	22738	0.82
		286.0	0.39	1.1	C-N	2886	0.10
		286.9	0.39	1.1	C-O, C-Cl	1017	0.04
		288.1	0.39	1.1	C=O	693	0.03
		291.1	0.39	1.1	$\pi-\pi^*$ shake ups	184	0.01
G-linker	C1s	284.6	0.39	0.9	C-C/C=C	29563	0.75
		285.8	0.39	1.2	C-N	5001	0.13
		286.6	0.39	1.2	C-O	3390	0.09
		287.9	0.39	1.2	C=O	1317	0.03
G-hPG	C1s	284.6	0.39	0.9	C-C/C=C	4413	0.17
		283.7	0.39	0.8	C-C ^{sp2} diff. charged	1534	0.06
		285.1	0.39	0.9	C-N	761	0.03
		286.1	0.39	1.1	C-O	17157	0.68
		287.5	0.39	1.3	C=O	964	0.04
2D-hPG	C1s	288.7	0.39	1.3	O=C-O	350	0.01
		285.0	0.39	1.2	C-C/C=C	1396	0.11
		286.4	0.39	1.2	C-O-C	10059	0.76
		287.8	0.39	1.2	C=O	1190	0.09
2D-hPGS	C1s	289.1	0.39	1.2	O=C-O	499	0.04
		285.0	0.39	1.2	C-C/C=C	13881	0.65
		286.6	0.39	1.3	C-O-C, C-O-S	6363	0.30
		287.9	0.39	1.3	C=O	598	0.03
		289.0	0.39	1.3	O=C-O	339	0.02

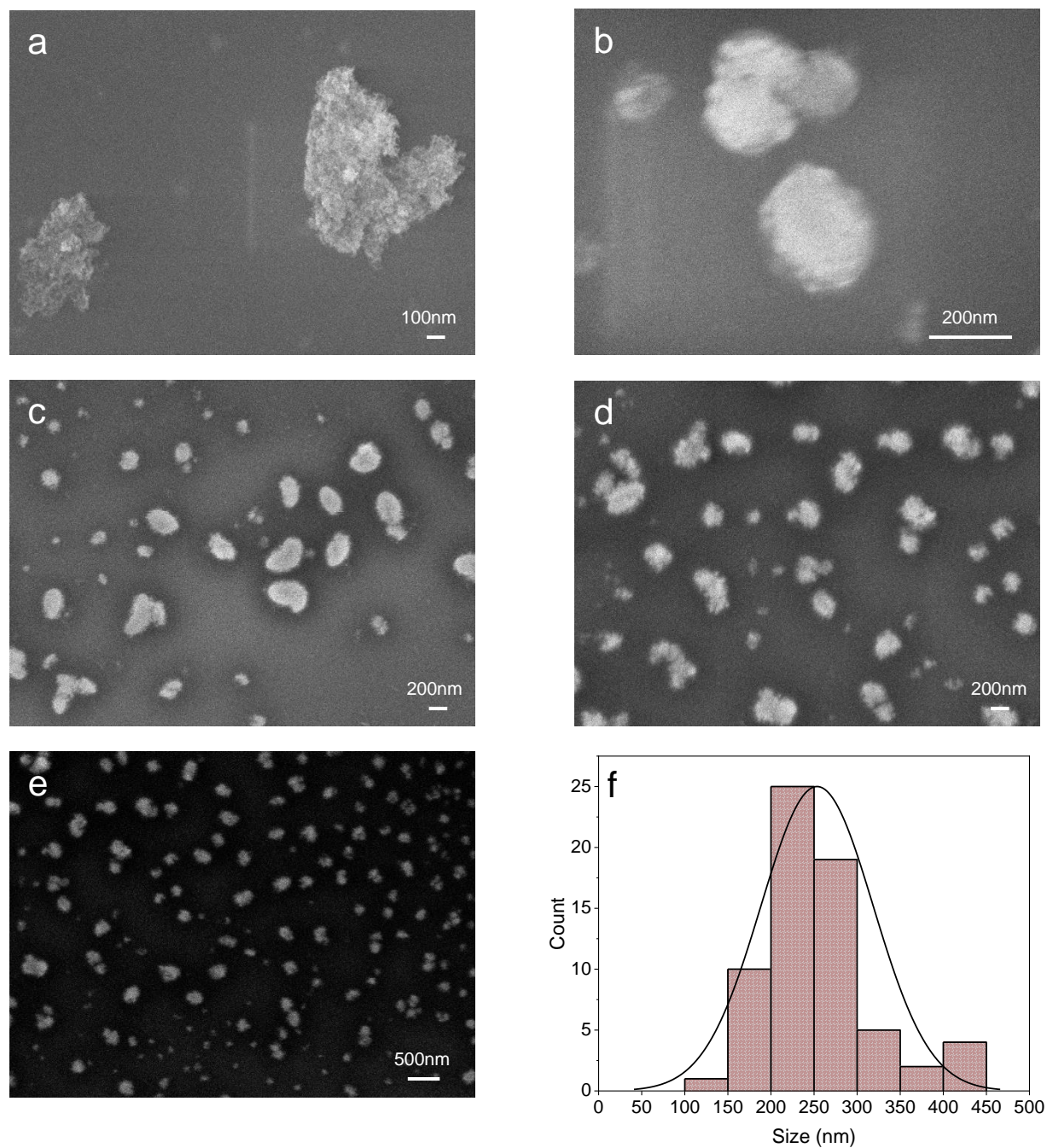


Figure S6. (a-e) SEM images and (f) size distribution histogram of 2D-hPG.

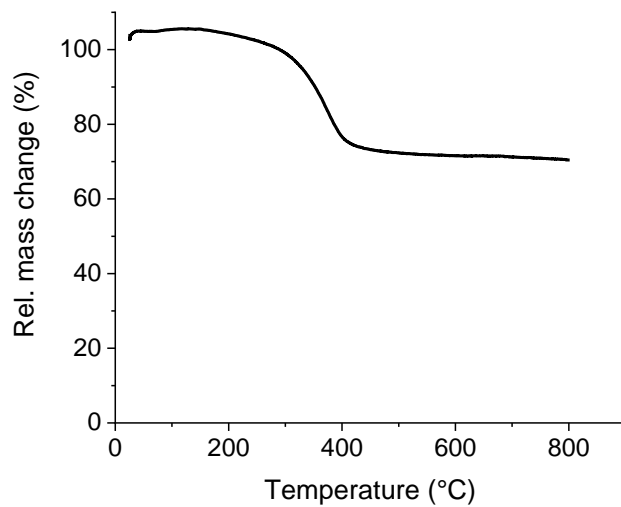


Figure S7. TGA thermograms of the cleaved TRGO measured under an argon atmosphere. The weight decrease shows ~25 wt% of hPG content in the cleaved TRGO.

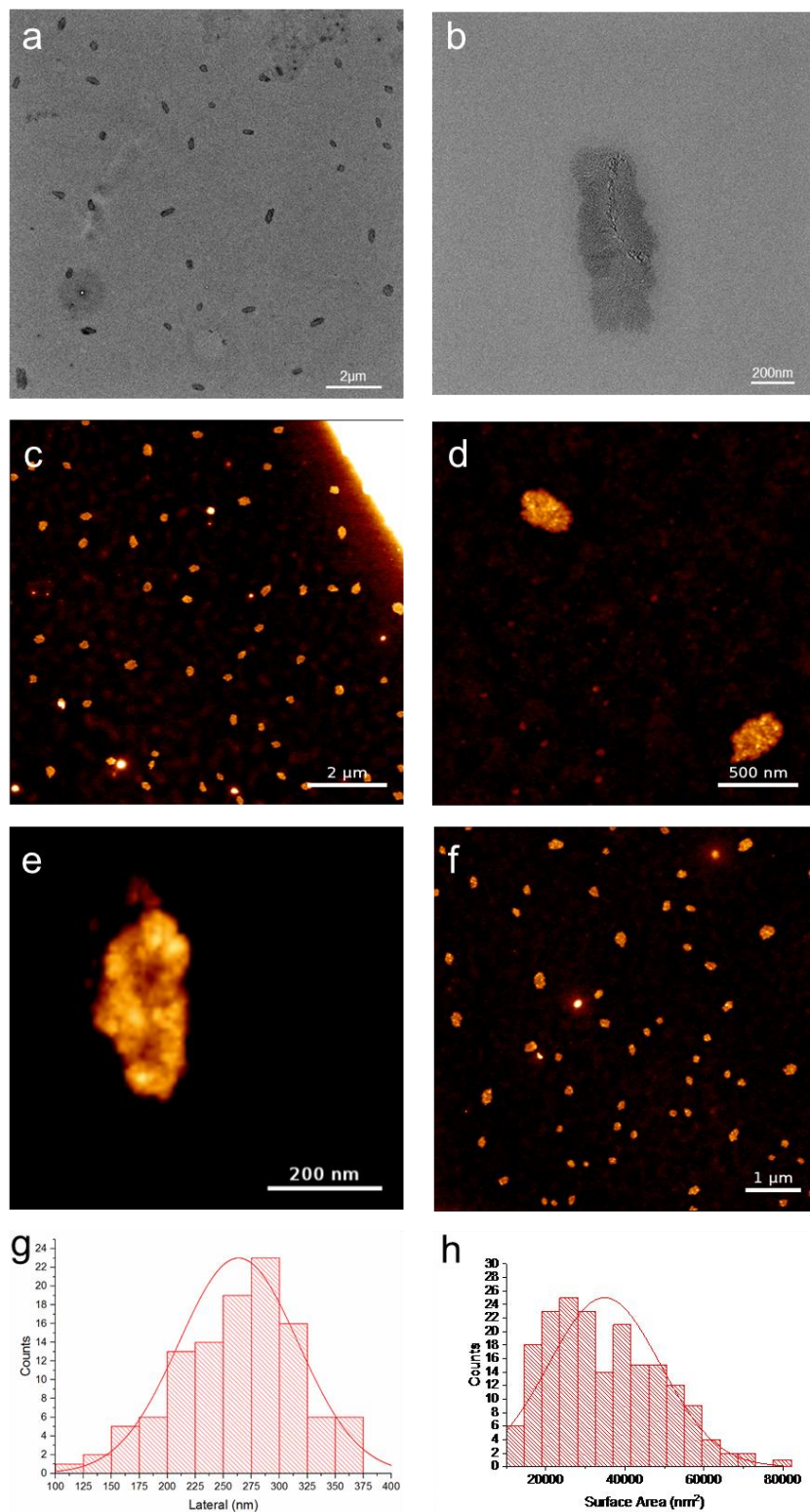


Figure S8. (a, b) TEM images, (c-f) SFM images, (g) size distribution histogram, and (h) surface area distribution of 2D-hPGS measured by TM-SFM ($n=192$), $34814 \pm 14118 \text{ nm}^2$.

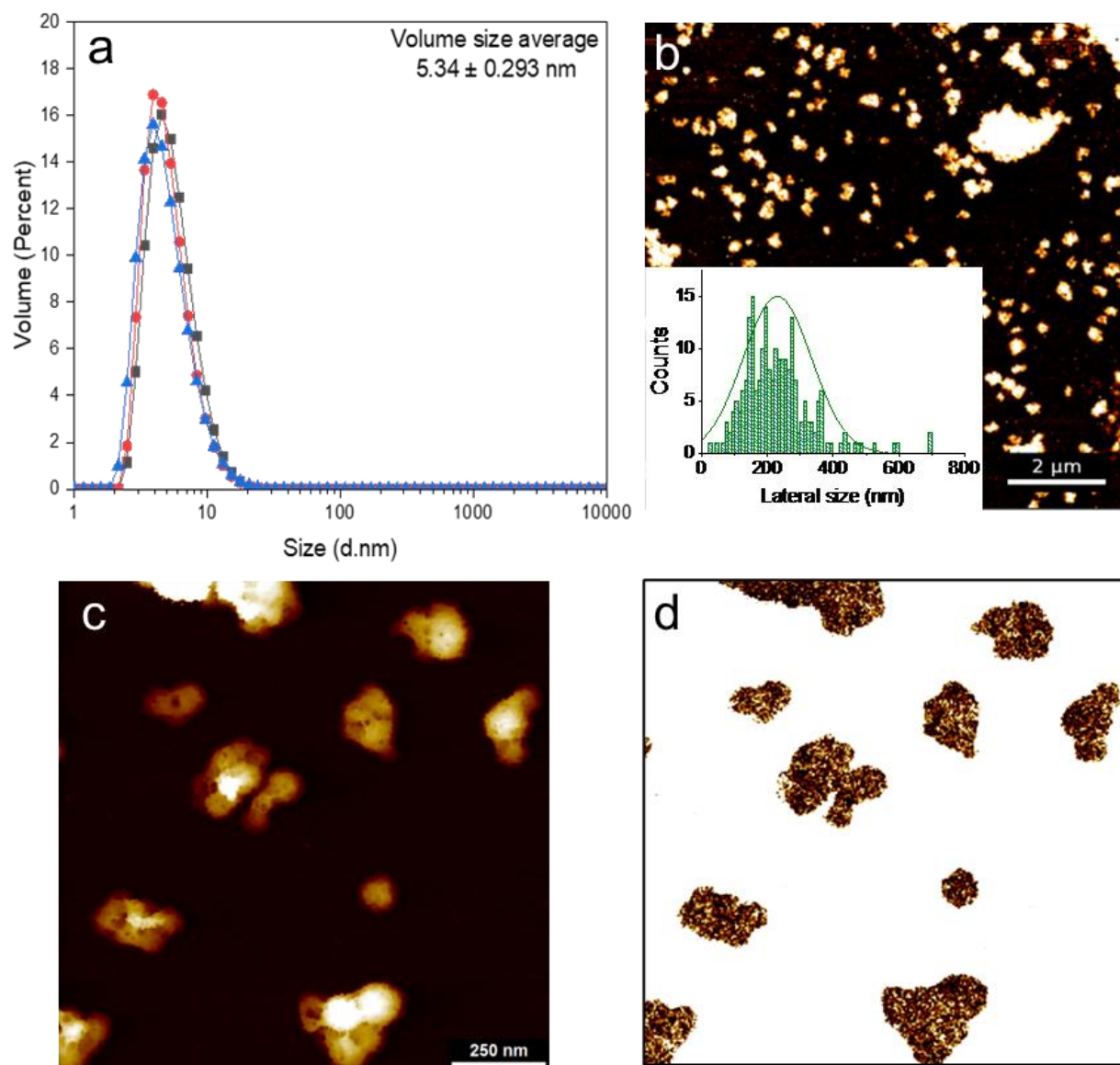


Figure S9. (a) Size distribution of hPG with 10 KDa molecular weight in water measured by DLS and (b-c) SFM-QI height images of 3D-hPGS. Inset figure S8b is a size distribution histogram of 3D-hPGS. (d) SFM-QI stiffness image demonstrating very low stiffness (dark regions) for 3D-hPGS in their hydrated state and immobilized on top of the very stiff mica substrate (saturated white region).

4 Calculation of IC50 in molarity

Average surface area of one 2D-hPGS measured by TM-SFM [nm^2]

$$A[2D\text{-hPGS}] \approx 35000 \text{ nm}^2$$

Average surface size of one hPG (10 KDa):

$$A [\text{hPG}] = \pi \cdot \left(\frac{5.34 \text{ nm}}{2} \right)^2 = 22.4 \text{ nm}^2 \quad \text{Equation S 4}$$

Theoretically number of hPG (10KDa) per sheet:

$$\text{Molecular weight of one 2D-hPGS sheet} = n [\text{hPG}] \times 10\text{KDa} = 15.63 \text{ (MDa)} \quad \text{Equation S 5}$$

$$\text{IC}_{50} \text{ value of 2D-hPGS against HSV-1 [nM]} = \text{—————} = 1.28 \text{ nM} \quad \text{Equation S 6}$$

$$\text{IC}_{50} \text{ value of 2D-hPGS against SARS-CoV-2 [nM]} = \text{—————} = 3.02 \text{ nM} \quad \text{Equation S 7}$$

* measured by DLS (Figure S8a).

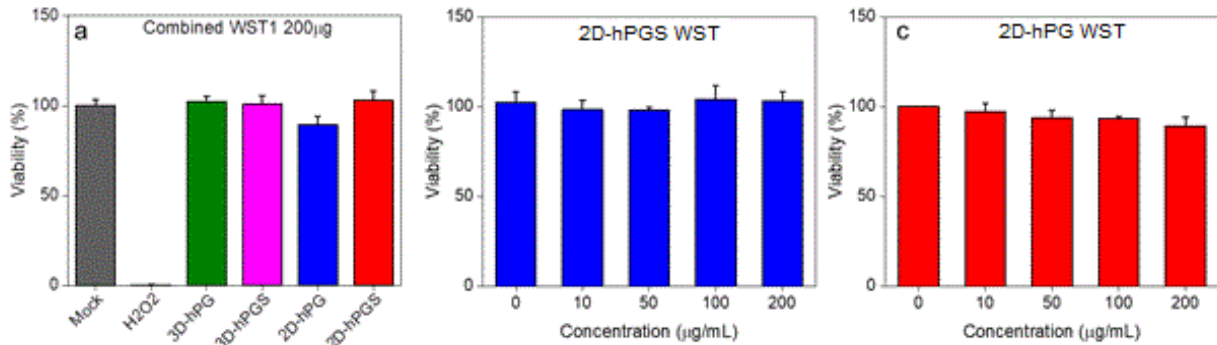


Figure S10. Cell viability of polyglycerol nanosheets and three-dimensional polyglycerol nanogels against Vero E6 cells. (a) Cell viability assay (WST-1) for 3D-hPG, 3D-hPGS, 2D-hPG, and 2D-hPGS (200 $\mu\text{g}/\text{mL}$ each), Mock and treatment with 30% solution of hydrogen peroxide used as baseline and positive control correspondingly. Cell viability assay (WST-1) for 2D-hPGS (b), 2D-hPG (c). Cells were cultured in presence of different concentrations of the synthesized nanomaterials for 24 h. Then cell viability was measured by WST kit.

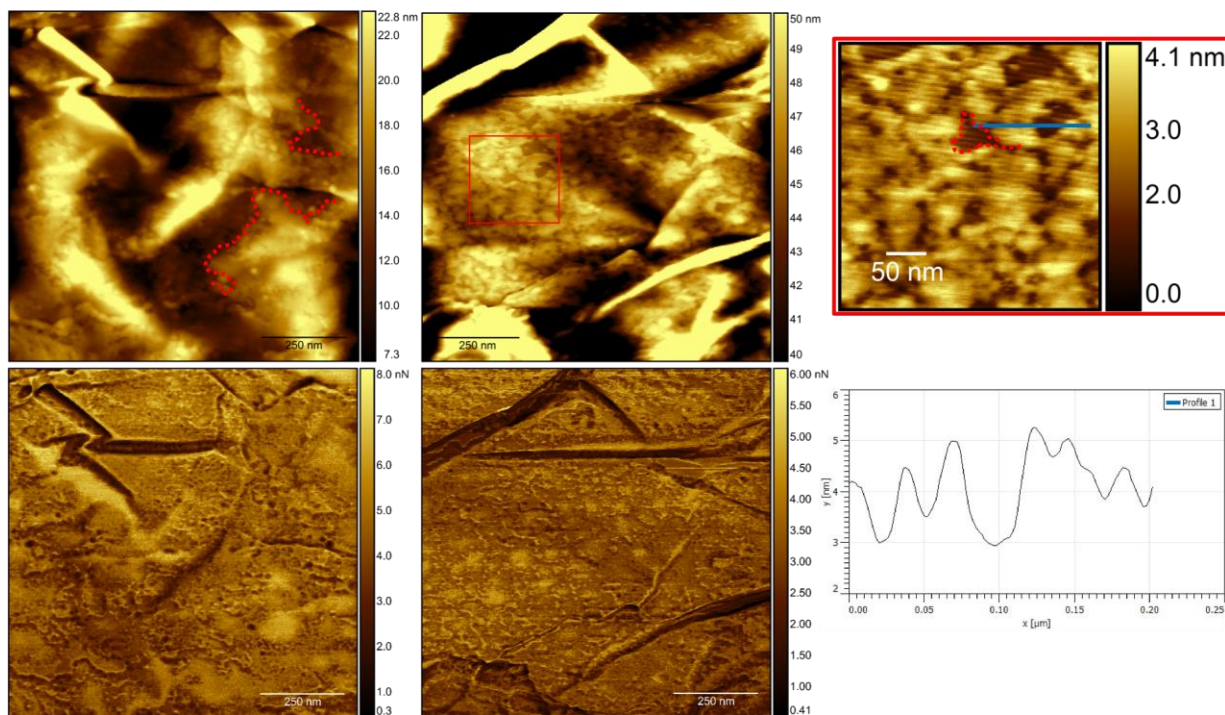


Figure S11. Top row demonstrates the typical SFM-QI height image of wrinkled TRGO-linker-hPG sheets. Bottom row demonstrates the SFM-QI pull off force images of the corresponding height images in top row. Dotted red lines show the visually recognizable borders of the hPG layer attached to the TRGO-Linker structure. Line profile demonstrates the height variation of observed hPG layer attached to the TRGO-linker-hPG surface. Pull off force images imply chemical and adhesion differences experienced by the SFM tip during interaction with the surfaces.

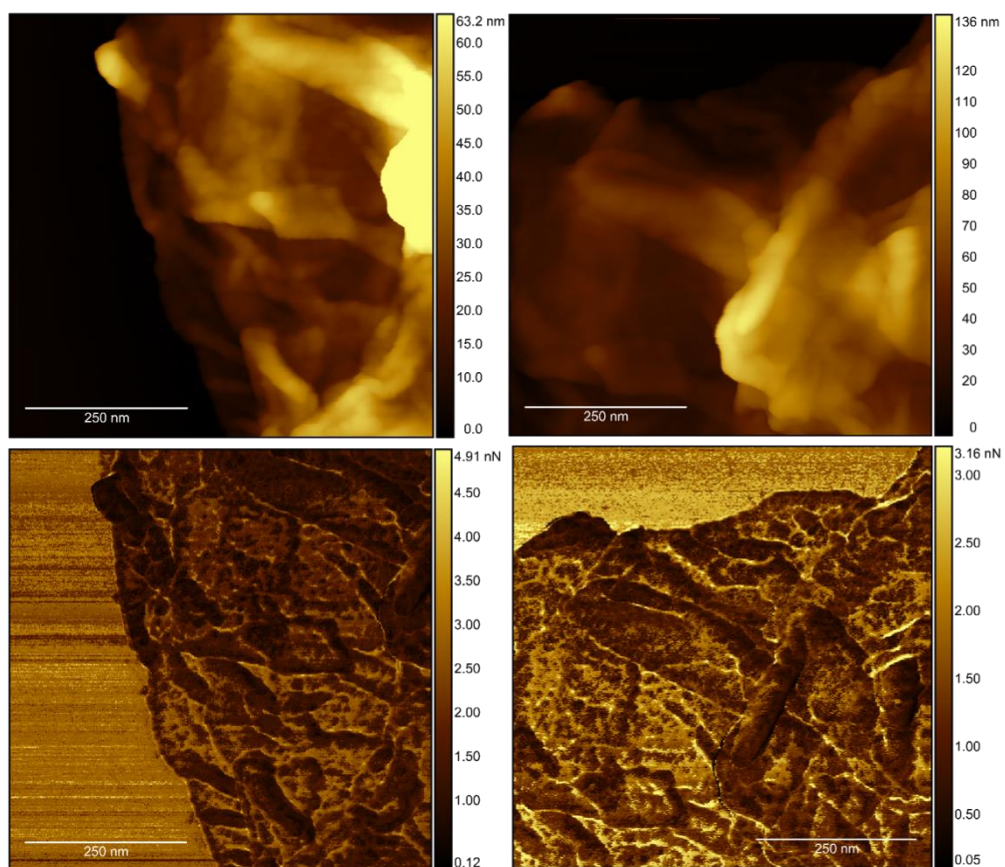


Figure S12. Top row demonstrates the typical SFM-QI height image of wrinkled TRGO-cleaved (after cleaving hPG layer). Bottom row demonstrates the SFM-QI pull off force images of the corresponding height images in top row. Due to the highly crumbled and wrinkled nature of these structures, visual confirmation of the hPG layer remaining if any was difficult.

References

- (1) Schlüter, B.; Mülhaupt, R.; Kailer, A. J. T. L., Synthesis and Tribological Characterization of Stable Dispersions of Thermally Reduced Graphite Oxide. **2014**, *53* (1), 353.
- (2) Sunder, A.; Hanselmann, R.; Frey, H.; Mülhaupt, R., Controlled synthesis of hyperbranched polyglycerols by ring-opening multibranching polymerization. *Macromolecules* **1999**, *32* (13), 4240.
- (3) Calizo, I.; Balandin, A. A.; Bao, W.; Miao, F.; Lau, C. N., Temperature Dependence of the Raman Spectra of Graphene and Graphene Multilayers. *Nano Letters* **2007**, *7* (9), 2645.
- (4) Tanaka, M.; Kagawa, H.; Yamanashi, Y.; Sata, T.; Kawaguchi, Y., Construction of an Excisable Bacterial Artificial Chromosome Containing a Full-Length Infectious Clone of Herpes Simplex Virus Type 1: Viruses Reconstituted from the Clone Exhibit Wild-Type Properties In Vitro and In Vivo. *Journal of Virology* **2003**, *77* (2), 1382.
- (5) Wölfel, R.; Corman, V. M.; Guggemos, W.; Seilmaier, M.; Zange, S.; Müller, M. A.; Niemeyer, D.; Jones, T. C.; Vollmar, P.; Rothe, C.; Hoelscher, M.; Bleicker, T.; Brünink, S.; Schneider, J.; Ehmman, R.; Zwirgmaier, K.; Drosten, C.; Wendtner, C., Virological assessment of hospitalized patients with COVID-2019. *Nature* **2020**, *581* (7809), 465.
- (6) Zhang, J.; Li, C.; Wang, Y.; Zhuo, R.-X.; Zhang, X.-Z., Controllable exploding microcapsules as drug carriers. *Chemical Communications* **2011**, *47* (15), 4457.
- (7) Steinhilber, D.; Rossow, T.; Wedepohl, S.; Paulus, F.; Seiffert, S.; Haag, R., A Microgel Construction Kit for Bioorthogonal Encapsulation and pH-Controlled Release of Living Cells. *Angewandte Chemie International Edition* **2013**, *52* (51), 13538.
- (8) Faghani, A.; Donskyi, I. S.; Gholami, M. F.; Ziem, B.; Lippitz, A.; Unger, W. E. S.; Bottcher, C.; Rabe, J. P.; Haag, R.; Adeli, M., Controlled Covalent Functionalization of

Thermally Reduced Graphene Oxide To Generate Defined Bifunctional 2D Nanomaterials. *Angewandte Chemie-International Edition* **2017**, *56* (10), 2675.

(9) Roller, S.; Zhou, H. X.; Haag, R., High-loading polyglycerol supported reagents for Mitsunobu- and acylation-reactions and other useful polyglycerol derivatives. *Mol. Divers.* **2005**, *9* (4), 305.

(10) Dey, P.; Bergmann, T.; Cuellar-Camacho, J. L.; Ehrmann, S.; Chowdhury, M. S.; Zhang, M.; Dahmani, I.; Haag, R.; Azab, W., Multivalent Flexible Nanogels Exhibit Broad-Spectrum Antiviral Activity by Blocking Virus Entry. *ACS Nano* **2018**, *12* (7), 6429.

3.2 One-pot Gram-scale Synthesis of Virucidal Heparin-mimicking Polymers as HSV-1 Inhibitors

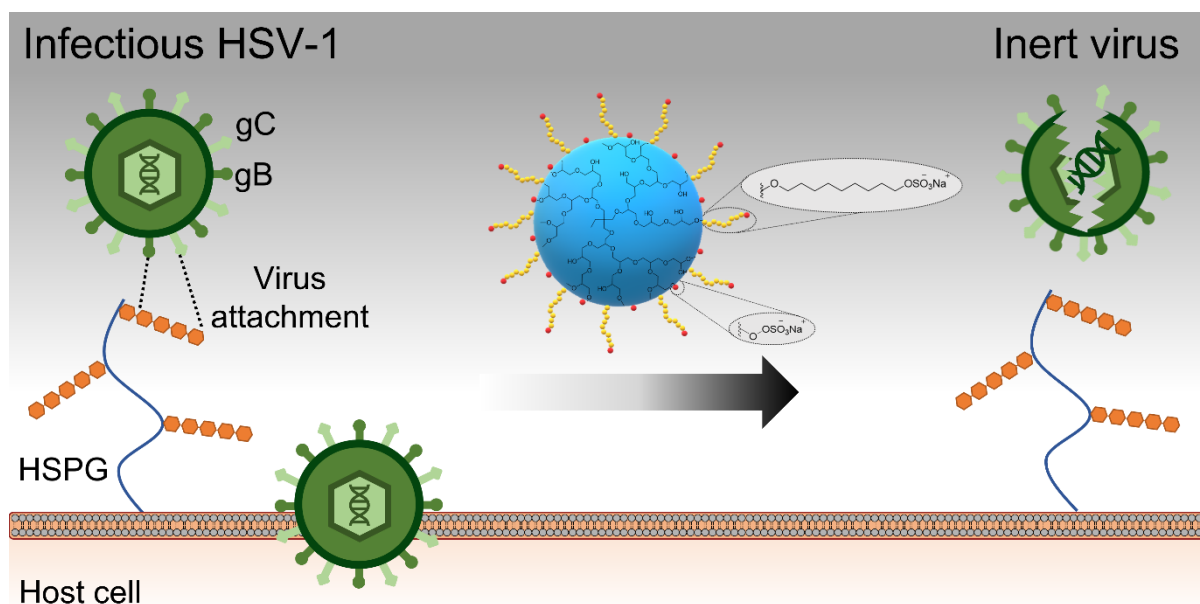


Figure 26. Reprinted with permission from Ref. [227]. Copyright 2021 Royal Society of Chemistry.

Vahid Ahmadi,* Chuanxiong Nie, Ehsan Mohammadifar, Katharina Achazi, Stefanie Wedepohl, Yannic Kerkhoff, Stephan Block, Klaus Osterrieder, and Rainer Haag*

Chem. Commun., **2021**, 57, 11948-11951

<https://doi.org/10.1039/D1CC04703E>

Authors contribution:

Vahid Ahmadi designed the concept, performed the synthesis, characterization, as well as wrote the manuscript. Chuanxiong Nie and Klaus Osterrieder supported the virology experiments. Katharina Achazi and Stefanie Wedepohl helped with the biological studies. Yannic Kerkhoff and Stephan Block performed statistical analysis. Rainer Haag supervised the project and edited the manuscript.

ChemComm

Chemical Communications

rsc.li/chemcomm



ISSN 1359-7345

COMMUNICATION

Vahid Ahmadi, Rainer Haag *et al.*
One-pot gram-scale synthesis of virucidal
heparin-mimicking polymers as HSV-1 inhibitors



One-pot gram-scale synthesis of virucidal heparin-mimicking polymers as HSV-1 inhibitors†

Vahid Ahmadi,^{ib *a} Chuanxiong Nie,^{ib a} Ehsan Mohammadifar,^a Katharina Achazi,^a Stefanie Wedepohl,^{ib a} Yannic Kerkhoff,^{ib a} Stephan Block,^{ib a} Klaus Osterrieder^{ib bc} and Rainer Haag^{ib *a}

Cite this: *Chem. Commun.*, 2021, 57, 11948

Received 24th August 2021,
Accepted 8th October 2021

DOI: 10.1039/d1cc04703e

rsc.li/chemcomm

A straightforward and gram-scale synthesis method was developed to engineer highly sulfated hyperbranched polyglycerol bearing sulfated alkyl chains. The compounds with shorter alkyl chains showed multivalent virustatic inhibition against herpes simplex virus type 1 (HSV-1), similar to heparin. In contrast, the compound with the longest alkyl chains irreversibly inhibited the virus.

Herpes simplex virus type 1 (HSV-1) infections are common and affect approximately 70–90% of the adult population worldwide.¹ Although HSV-1 is a well-studied virus, it remains a major public health concern because vaccines are unavailable and common antiviral drugs such as acyclovir, the most commonly prescribed medication, show limited efficacy.² HSV-1 entry into the host cell is initiated by electrostatic interaction between negatively charged heparan sulfates (HSs) located on the host cell surface, and positively charged domains of the viral envelope glycoprotein B (gB) and glycoprotein C (gC).³ Protein-polyelectrolyte interactions are dominated by counterion release, *i.e.*, the positively charged patches become multivalent counterions of the polyelectrolyte, resulting in counterions being released from the polyelectrolyte (driving force), a process that increases entropy.⁴ The finding that heparin, which is a soluble derivative of HS, shows an inhibitory effect for a variety of viruses by interacting with their surface, has led to the development of numerous heparin-mimetic compounds.^{5–9} Despite many trials, researchers have encountered limitations that are inherent to these compounds, such as their high anticoagulant activity, their complicated synthesis, and their mechanism of virus inhibition, which is virustatic rather than virucidal.¹⁰ The compounds reversibly bind to the virus, which

prevents viral attachment and, consequently, entry into the host cell. However, the dilution effect *in vivo* causes dissociation of the binding complexes, reversing the binding and ultimately leading to virus infection.¹¹ Virucidal compounds, on the other hand, interact with viruses and physically render them non-infectious, for example by disrupting their envelope, thus preventing infection even upon dilution in body fluids. Development of new antiviral compounds that address these challenges is of major interest, and one must strive to design antiviral materials that are biocompatible, virucidal, and easily scalable. One way to develop a virucidal compound is to combine electrostatic and hydrophobic interactions while minimizing the potential toxicity that can be caused by increasing hydrophobicity.¹² By developing gold-based nanoparticles containing 11-mercapto-undecansulfonate moieties, Stellacci *et al.*¹⁰ first developed the virucidal effect of hydrophobic sulfonated gold nanoparticles. As part of our approach, we are using polymeric cores to address issues concerning gold nanoparticle health risks, synthetic challenges, and economic aspects.

Current antiviral therapies are less effective over time due to virus mutations, which obviously calls for the development of broad-spectrum antiviral alternatives.¹³ Furthermore, due to the difference in how viruses replicate, there is little hope of developing broad-spectrum drugs with intracellular approaches. Thus, extracellular antivirals – which usually come in the form of entry inhibitors – are of importance. To inhibit viruses effectively, virus–inhibitor interactions must be stronger than those between viruses and cells.¹⁴ Monovalent inhibitors are therefore ineffective since they do not completely block receptor sites and are unable to compete with viral proteins for binding. As a result, for designing potent inhibitors, it is important to consider multivalent interactions. Utilizing polymers is then of great interest and have been used in the development of antiviral compounds over the past decades.¹⁵ Hyperbranched polyglycerol (hPG) offers a multifunctional scaffold with high biocompatibility and hydrophilicity that can be used in numerous biomedical applications, ranging from drug delivery to pathogen inhibition.¹⁶ Having found that sulfated hPG (hPGS) exhibits similar bioactivity to heparin,¹⁷ our group developed various antiviral compounds with

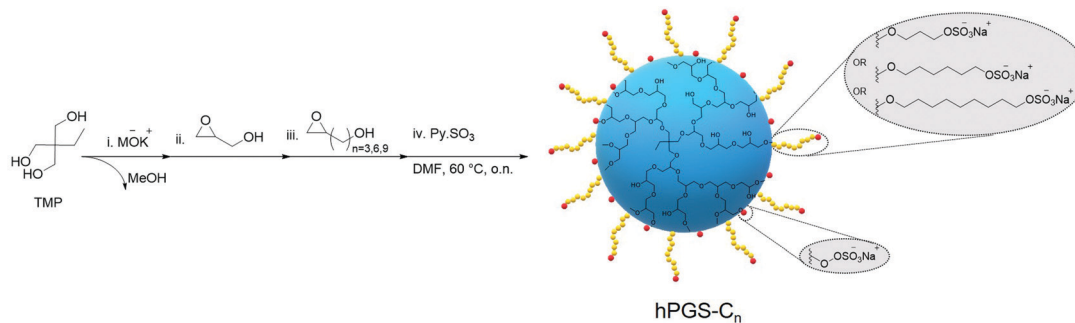
^a Institut für Chemie und Biochemie, Freie Universität Berlin, Takustrasse 3, 14195 Berlin, Germany. E-mail: haag@chemie.fu-berlin.de

^b Institut für Virologie, Robert von Ostertag-Haus, Zentrum für Infektionsmedizin Freie Universität Berlin, Robert-von-Ostertag-Str. 7-13, 14163 Berlin, Germany

^c Department of Infectious Diseases and Public Health, Jockey Club College of Veterinary Medicine and Life Sciences, City University of Hong Kong, Kowloon Tong, Hong Kong

† Electronic supplementary information (ESI) available. See DOI: 10.1039/d1cc04703e



Scheme 1 One-pot synthesis route of hPGS-C_n.

different architectures.^{8,9,18} Although all of these compounds exhibit impressive antiviral properties including inhibition of HSV at picomolar concentrations,⁹ none are virucidal.

Here, we rationally designed a novel class of virucidal compounds based on a one-pot approach towards hPGS-bearing alkyl chains. These compounds irreversibly inhibit HSV-1 infection, and we highlight their ease of synthesis as well as their robust activity. In a one-pot, four-step synthesis approach, we used anionic ring-opening polymerization to synthesize hPG, which we functionalized with a hydrophobic alkyl chain and finally sulfated for the electrostatic interaction with the virus (Scheme 1 and Scheme S2, ESI[†]). It has been demonstrated that hPG is more effectively functionalized in a one-pot reaction when a glycidol derivative is used.¹⁹ We, therefore, synthesized, and characterized separately, glycidols containing hydrophobic alkyl chains of different lengths (Scheme S1, ESI[†]).

Briefly, the hydrophilic core of hPG was first synthesized solvent-free from the trimethylolpropane (TMP) initiator *via* anionic ring-opening polymerization of glycidol, following previously described procedures.²⁰ Monomer-to-initiator ratios were adjusted for all polymerizations to yield an hPG core of approximately 5 kDa (Table S1 and Fig. S1, ESI[†]). However, no quenching was performed after addition of the monomer, and the reaction continued until all of the glycidol was consumed as evidenced by the disappearance of the corresponding peaks at 2.6 ppm and 3.7 ppm in ¹H-NMR spectra (Fig. S2, ESI[†]). The hPG cores were then functionalized by adding glycidol derivatives of varying alkyl chain length to form hPG-C₃, hPG-C₆, and hPG-C₉. Using the integral peak ratio of alkyl chain protons in ¹H-NMR at 1.2–2.1 ppm to hPG backbone protons at 3.6–4.6 ppm, the degree

of functionalization was calculated to be around 40% for all compounds (Fig. S3 and eqn S2–S4, ESI[†]). Then, in the same reactor, dimethylformamide was added, and a reaction with sulfur trioxide pyridine complex was performed to convert the hydroxyl groups to sulfate groups following a previously described protocol.²¹ In a previous study,²² we had found that the degree of sulfation (DS) affects inhibitory effects; therefore, the ratios were adjusted in order to obtain highly sulfated compounds. The final products were purified using tangential flow filtration (TFF) followed by freeze-drying, resulting in hPGS-C₃, hPGS-C₆, and hPGS-C₉ with over 90% DS as calculated by elemental analysis (Table S2 and eqn S5, S6, ESI[†]). As a control, a sulfated hPG without an alkyl chain, namely hPGS-C₀, with the same degree of sulfation and molecular weight was synthesized according to available protocols.^{21,23} Table 1 provides a summary of the results.

Using two human lung cell lines, A549 and 16HBE140, as well as a standard cell line for HSV-1 propagation, Vero E6, we performed CCK-8 assays to determine the viability of the cells after treatment with the sulfated polymers (Fig. 1 and Fig. S4, ESI[†]). The half-maximal cytotoxic concentration (CC₅₀) for each compound was calculated for each cell line (Table 1). At concentrations of up to 1000 μg mL⁻¹, none of the compounds showed discernable cytotoxicity (Fig. 1 and Fig. S4, ESI[†]), with the exception of 16HBE140-cells. For this cell line, the compound with the longest alkyl chain, hPGS-C₉, exerted an effect on viability at a concentration of 1000 μg mL⁻¹. At the highest concentration tested (10 000 μg mL⁻¹), cell viability was reduced in all cell lines for all tested compounds, with hPGS-C₉ impairing viability most. Taking the CC₅₀ values (Table 1) into account, alkyl chains have a small effect on the toxic properties of the synthesized compounds, and, as

Table 1 Summary of the characteristics of the synthesized inhibitors

Compound	M _n ^a [kDa]	PDI	Degree of functionalization [%]	M _n ^b [kDa]	M _n ^c [kDa]	Degree of sulfation [%]	Zeta potential in 10 mM PB buffer [mV]	CC ₅₀ [mg mL ⁻¹]			IC ₅₀ [μg mL ⁻¹]	IC ₅₀ [nM]	SI	Inhibition mechanism
								A549	VeroE6	HBE				
hPGS-C ₉	3.8	1.7	38	6.7	12.1	97	-35.5 ± 2.3	3.90	4.76	1.49	0.189 ± 0.054	15.6	25200	Virucidal
hPGS-C ₆	3.9	1.8	39	6.6	11.5	93	-35.6 ± 1.2	12.68	23.93	20.19	0.256 ± 0.089	22.2	93500	Virustatic
hPGS-C ₃	3.9	1.8	39	6.7	10.6	96	-33.1 ± 2.1	25.93	13.31	37.68	5.098 ± 1.048	480.9	2600	Virustatic
hPGS-C ₀	4.6	1.7	0	—	11.3	91	-32.4 ± 1.4	13.93	6.97	10.47	2.297 ± 0.695	203.3	3000	Virustatic

^a Molecular weight of polymeric core obtained by GPC. ^b Molecular weight after functionalization obtained by GPC. ^c Molecular weight after sulfation calculated by elemental analysis and ¹H NMR. ^d Selectivity index (SI = CC₅₀/IC₅₀) calculated for VeroE6 cells.



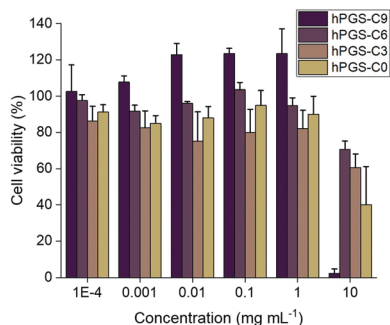


Fig. 1 Cytotoxicity profile of the synthesized inhibitors determined by a CCK-8 assay using Vero E6 cells. The cell viability of compound treated cells is normalized to the cell viability of non-treated cells that was set to 100% cell viability.

predicted, cells are more sensitive to compounds with longer alkyl chains.

Plaque reduction assays using Vero E6 cells were used to determine the compounds' antiviral activity against HSV-1. Herein, virions were pre-incubated with the compounds at different concentrations and then titrated on Vero cells to determine the ratio of inhibited virions. The dose-response curves obtained from the experiment are shown in Fig. 2a, and the respective half-maximal inhibitory concentrations (IC_{50}) are shown in Table 1. As expected, the synthesized heparan-mimetic compounds exhibited considerable antiviral activity, with IC_{50} values in the nanomolar range. We found that the IC_{50} value decreases with increasing alkyl chain length. hPGS-C₉ exhibited the strongest inhibitory effect (IC_{50} = 15.6 nM), while hPGS-C₆, hPGS-C₃, and hPGS-C₀ showed IC_{50} values of 22.2, 480.9, and 203.3 nM, respectively. Hydrophobicity therefore seems to play an important role in the inhibition of HSV-1. The compounds were then evaluated for their inhibition mechanism. For this purpose, we used a virucidal assay in

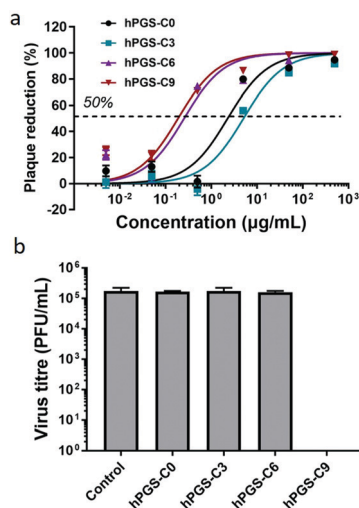


Fig. 2 (a) Concentration-dependent inhibition of HSV-1 infection on Vero E6 cells. (b) Virucidal potency of the synthesized inhibitors against HSV-1. Data are expressed as mean \pm SD (n = 4).

which compounds with a concentration of 1 mg mL^{-1} were pre-incubated with virus (approx. 10^5 PFU). The solutions were then diluted five times by a factor of 10 and each dilution was titrated by plaque assay to determine the number of active virions present. When the inhibition is remained even after dilution below its IC_{50} , it is considered as virucidal inhibition, implying that the virus was irreversibly inactivated.¹⁰ Otherwise, it is considered as virustatic inhibition, which refers to reversible inhibition of the virus. We found that the compounds with shorter alkyl chains, hPGS-C₆ and hPGS-C₃, as well as the one without an alkyl chain, hPGS-C₀, are solely virustatic, whereas hPGS-C₉ showed virucidal properties (Fig. 2b). Therefore, an increase in alkyl chain length and therefore in hydrophobicity induce a strong virucidal effect, suggesting that sufficient alkyl chain length is causing rupture of the viral envelope. It should be noted that longer alkyl chains ($>C_9$), despite their possibly higher inhibitory activities, were not considered in this study, due to reports indicating that longer chains ($\geq C_{10}$) exert a significantly toxic effect on eukaryotic cells, including Vero E6 cells.⁵ Next, cellular infection assays were performed to examine the inhibitory activity of viral replication (Fig. 3). In a pre-infection assay, the cells were treated with the compounds at different concentrations for 45 minutes and then infected for 48 hours with HSV-1 expressing green fluorescent protein (GFP). To evaluate if the compounds still have an effect when cells are already infected, a post-infection assay was carried out. For the post-infection assay, cells were first infected for 1h prior to addition of the compounds. The total time of infection with GFP-tagged HSV-1 in this post-infection assay was 48 hours as well. The results of the pre- and post-infection experiments indicate that all compounds are highly effective as an inhibitor (Fig. S5b and c, ESI[†]). Nevertheless, the pre-infection assays also revealed a clear decrease in the number of infected cells for all compounds with a concentration higher than $10 \text{ } \mu\text{g mL}^{-1}$ (Fig. S5b, ESI[†]), probably because the compounds are capable of inhibiting the infection by progeny viruses, thereby reducing viral transmission between the cells. This also explains why the antiviral activity was lower in the post-infection when compared

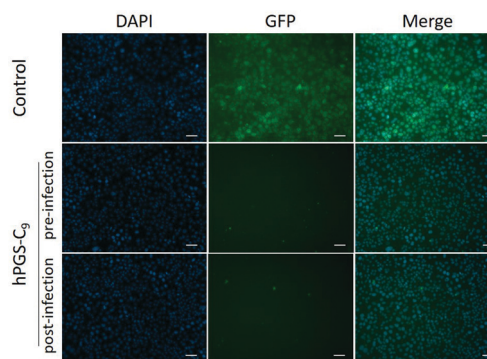


Fig. 3 Fluorescent microscopy images of HSV-1 infected cells treated with hPGS-C₉ ($100 \text{ } \mu\text{g mL}^{-1}$). Images from cells treated with other compounds are shown in Fig. S4 (ESI[†]). Scale bar: $20 \text{ } \mu\text{m}$. Cell nuclei are marked in blue, and infected cells in green.



to the pre-infection assay: after the first cycle of infection, large amounts of virions were produced, resulting in a higher viral load compared to that in the pre-infection assay. Furthermore, the selectivity index (SI) of each compound was calculated by dividing the CC_{50} and IC_{50} values (Table 1). hPGS-C₉, for example, demonstrated a remarkable SI of 25 200, which made it effective at blocking and destroying viruses without causing serious damage to host cells. This means that it only ruptures the membranes of the virus, not the cells. Observations regarding the high SI value of the compound suggest that the surface curvature of biosystems could account for its selective rapture of the viral membrane rather than that of the cell. As HSV-1 viruses are about 200 nm in size, their curvature and strain are higher than cells, which are about micrometres in size. More importantly, unlike viruses that contain only genetic information, cells have self-repairing mechanisms that can tolerate and repair damaged membranes.²⁴ HS-mimetic compounds, such as heparin and other sulfated polymers, have inherent anticoagulant properties. Due to their ability to activate antithrombin and turn it into a blood-clotting proteinase inhibitor, these compounds prolong blood clotting and are thus limited in concentration as virus inhibitors in clinical use.²⁵ We therefore determined *ex vivo* clotting times by measuring the activated partial thromboplastin time (APTT) of plasma treated with our inhibitors at concentrations ranging from 0.5 to 1000 $\mu\text{g mL}^{-1}$.

As a control we used commercially available heparin (Fig. S6, ESI†). Comparing the APTT of untreated human plasma with a mean of 31 seconds to the inhibitor-treated plasma, no changes were observed up to a concentration of 5 $\mu\text{g mL}^{-1}$. A similar concentration of heparin, however, led to a significant increase in the APTT of more than 500 seconds. At a concentration of 25 $\mu\text{g mL}^{-1}$, hPGS-C₉, hPGS-C₆, and hPGS-C₃ started to show mild effects on the APTT, whereas hPGS-C₀ increased the APTT more than fivefold. Considering the results for the alkyl-chain-functionalized polymers, hPGS-C₉, hPGS-C₆, and hPGS-C₃, one can observe that the length of the alkyl chain interferes with coagulation, as anticoagulant activity decreases with the length of the alkyl chain. This effect can be explained by a less dense distribution of sulfate groups in the longest-chained polymer, hPGS-C₉, when compared to hPGS-C₆ and hPGS-C₃ with their shorter chains and to hPGS-C₀ that does not carry side chains at all.

In conclusion, we have developed a method to synthesize antiviral compounds in a one-pot reaction at gram scale. Our approach was to rationally design the compounds in a synergistic approach by using alkyl chains for hydrophobic interactions and sulfate groups for electrostatic interactions. In studies against HSV-1, compounds with shorter chain lengths showed virustatic inhibition similar to that of heparin, while the compound with the longest chain length, hPGS-C₉, showed an irreversible virucidal effect. These compounds may also be used against other heparan sulfate-binding viruses. Furthermore, future studies into adapting the same one-pot approach, but with other comonomers with different functional groups, may allow this technique to produce gram-scale hPG-based virucidal compounds that are effective against other viruses as well.

This work was supported by SFB 1449. We thank Elisa Quaas for performing cell viability assays. We gratefully acknowledge assistance from the Core Facility BioSupraMol funded by DFG and from Ben Allen, who assisted us with the language polishing of the manuscript.

Conflicts of interest

There are no conflicts to declare.

Notes and references

- 1 *Human Herpesviruses: Biology, Therapy, and Immunoprophylaxis*, ed. A. Arvin, G. Campadelli-Fiume, E. Mocarski, P. S. Moore, B. Roizman, R. Whitley and K. Yamanishi, Cambridge University Press Copyright © Cambridge University Press, Cambridge, 2007.
- 2 K. Klysiak, A. Pietraszek, A. Karczewska and M. Nowakowska, *Curr. Med. Chem.*, 2020, **27**, 4118–4137.
- 3 A. M. Agelidis and D. Shukla, *Future Virol.*, 2015, **10**, 1145–1154.
- 4 K. Achazi, R. Haag, M. Ballauff, J. Dornedde, J. N. Kizhakkedathu, D. Maysinger and G. Multhaupt, *Angew. Chem., Int. Ed.*, 2021, **60**, 3882–3904.
- 5 I. S. Donskyi, W. Azab, J. L. Cuellar-Camacho, G. Guday, A. Lippitz, W. E. S. Unger, K. Osterrieder, M. Adeli and R. Haag, *Nanoscale*, 2019, **11**, 15804–15809.
- 6 E. Lee, M. Pavy, N. Young, C. Freeman and M. Lobigs, *Antiviral Res.*, 2006, **69**, 31–38.
- 7 P. Dey, T. Bergmann, J. L. Cuellar-Camacho, S. Ehrmann, M. S. Chowdhury, M. Zhang, I. Dahmani, R. Haag and W. Azab, *ACS Nano*, 2018, **12**, 6429–6442.
- 8 E. Mohammadifar, V. Ahmadi, M. F. Gholami, A. Oehrl, O. Kolyvushko, C. Nie, I. S. Donskyi, S. Herziger, J. Radnik, K. Ludwig, C. Bötcher, J. P. Rabe, K. Osterrieder, W. Azab, R. Haag and M. Adeli, *Adv. Funct. Mater.*, 2021, **31**, 2009003.
- 9 P. Pouyan, C. Nie, S. Bhatia, S. Wedepohl, K. Achazi, N. Osterrieder and R. Haag, *Biomacromolecules*, 2021, **22**, 1545–1554.
- 10 V. Cagno, P. Andreozzi, M. D'Alicarnasso, P. Jacob Silva, M. Mueller, M. Galloux, R. Le Goffic, S. T. Jones, M. Vallino, J. Hodek, J. Weber, S. Sen, E.-R. Janeček, A. Bekdemir, B. Sanavio, C. Martinelli, M. Donalisio, M.-A. Rameix Welti, J.-F. Eleouet, Y. Han, L. Kaiser, L. Vukovic, C. Tapparel, P. Král, S. Krol, D. Lembo and F. Stellacci, *Nat. Mater.*, 2018, **17**, 195–203.
- 11 B. Shogan, L. Kruse, G. B. Mulamba, A. Hu and D. M. Coen, *J. Virol.*, 2006, **80**, 4740–4747.
- 12 J. Said, E. Trybala, E. Andersson, K. Johnstone, L. Liu, N. Wimmer, V. Ferro and T. Bergström, *Antiviral Res.*, 2010, **86**, 286–295.
- 13 X. Huang, W. Xu, M. Li, P. Zhang, Y. S. Zhang, J. Ding and X. Chen, *Matter*, 2021, **4**, 1892–1918.
- 14 S. T. Jones, *J. Mater. Sci.*, 2020, **55**, 9148–9151.
- 15 R. H. Bianculli, J. D. Mase and M. D. Schulz, *Macromolecules*, 2020, **53**, 9158–9186.
- 16 H. Frey and R. Haag, *Rev. Mol. Biotechnol.*, 2002, **90**, 257–267.
- 17 J. Dornedde, A. Rausch, M. Weinhart, S. Enders, R. Tauber, K. Licha, M. Schirner, U. Zügel, A. von Bonin and R. Haag, *Proc. Natl. Acad. Sci. U. S. A.*, 2010, **107**, 19679–19684.
- 18 C. Nie, P. Pouyan, D. Lauster, J. Trimpert, Y. Kerkhoff, G. P. Szekeres, M. Wallert, S. Block, A. K. Sahoo, J. Dornedde, K. Pagel, B. B. Kaufer, R. R. Netz, M. Ballauff and R. Haag, *Angew. Chem., Int. Ed.*, 2021, **60**, 15870–15878.
- 19 F. Paulus, D. Steinhilber, P. Welker, D. Mangoldt, K. Licha, H. Depner, S. Sigrist and R. Haag, *Polym. Chem.*, 2014, **5**, 5020–5028.
- 20 M. Wallert, J. Plaschke, M. Dimde, V. Ahmadi, S. Block and R. Haag, *Macromol. Mater. Eng.*, 2021, **306**, 2000688.
- 21 H. Türk, R. Haag and S. Alban, *Bioconjugate Chem.*, 2004, **15**, 162–167.
- 22 B. Ziem, W. Azab, M. F. Gholami, J. P. Rabe, N. Osterrieder and R. Haag, *Nanoscale*, 2017, **9**, 3774–3783.
- 23 A. Sunder, R. Hanselmann, H. Frey and R. Mülhaupt, *Macromolecules*, 1999, **32**, 4240–4246.
- 24 S. K. Y. Tang and W. F. Marshall, *Science*, 2017, **356**, 1022–1025.
- 25 S. T. Olson, B. Richard, G. Izaguirre, S. Schedin-Weiss and P. G. W. Gettins, *Biochimie*, 2010, **92**, 1587–1596.



Supporting Information

One-pot gram-scale synthesis of virucidal heparin-mimicking polymers as HSV1 inhibitors

Vahid Ahmadi,^{*a} Chuanxiong Nie,^a Ehsan Mohammadifar,^a Katharina Achazi,^a Stefanie Wedepohl,^a Yannic Kerkhoff,
^a Stephan Block,^a Klaus Osterrieder,^{b,c} and Rainer Haag^{*a}

^a Institut für Chemie und Biochemie, Freie Universität Berlin, Takustrasse 3, 14195 Berlin, Germany

^b Institut für Virologie, Robert von Ostertag-Haus, Zentrum für Infektionsmedizin, Freie Universität Berlin, Robert-von-Ostertag-Str. 7-13, 14163 Berlin, Germany

^c Department of Infectious Diseases and Public Health, Jockey Club College of Veterinary Medicine and Life Sciences, City University of Hong Kong, Kowloon Tong, Hong Kong

Table of contents

1	Experimental.....	3
1.1	Materials	3
2	Method and Instrumentations	3
2.1.1	Gel permeation chromatography (GPC)	3
2.1.2	Zeta potential	3
2.1.3	Nuclear magnetic resonance (NMR).....	3
2.1.4	Tangential Flow Filtration (TFF)	3
2.1.5	Cell viability assay CCK-8.....	3
2.1.6	Virus propagation and inhibition study	4
2.1.6.1	Virus propagation and virus titer determination by plaque assay	4
2.1.6.2	Plaque reduction assay	4
2.1.6.3	Virucidal assay	4
2.1.6.4	Pre and post cellular infection assays.....	4
2.1.7	Statistical Analysis.....	4
2.1.8	Fluorescent microscopy image analysis.....	4
2.1.9	Activated partial thromboplastin time (APTT).....	5
3	Synthetic procedures.....	6
3.1	Synthesis of comonomers	6
3.1.1	9-(oxiran-2-yl)nonan-1-ol	6
3.1.2	6-(oxiran-2-yl)hexan-1-ol.....	6
3.1.3	3-(oxiran-2-yl)propan-1-ol	6
3.2	One-pot synthesis approach to hPGS-C _n	7
3.2.1	Degree of functionalization (DF).....	9
3.2.2	Degree of sulfation (DS).....	10
3.2.3	Molecular weight.....	10
4	References	14

1 Experimental

1.1 Materials

Meta-chloroperoxybenzoic acid (*m*CPBA) ($\leq 77\%$), 1,1,1-trimethylolpropane (TMP) ($\geq 98\%$), glycidol (96%) was purified by vacuum distillation, and sulfur trioxide pyridine complex (97%) were purchased from Sigma Aldrich (Darmstadt, Germany). 4-Penten-1-ol (99 %) and anhydrous dimethylformamide (DMF) purchased from Acros (Part of Thermo Fischer Scientific, Geel – Belgium). 7-Octen-1-ol (96%) was purchased from abcr. GmbH (Karlsruhe, Germany). The hyperbranched polyglycerol (hPG), M_n 5 kDa, and $D = 1.7$, was synthesized through ring-opening anionic polymerization followed by sulfation to yield hPGS- C_0 as a control according to literatures.^{1,2}

2 Method and Instrumentations

2.1.1 Gel permeation chromatography (GPC)

GPC measurements were carried out using a Shimadzu Prominence-I LC-2030 equipped with an internal UV absorption detector and a Shimadzu RID-29A refractive index detector. Columns were held at 40 degrees Celsius and flow rates of the mobile phase (DMF) were set to 1 mL/min. 100 μ L of a sample with a concentration of 5 mg/mL were injected for each measurement. GPC measurements were conducted using polystyrene as the standard.

2.1.2 Zeta potential

Nano ZSPO (Malvern) was used to measure the zeta potential in PB solution.

2.1.3 Nuclear magnetic resonance (NMR).

A Jeol Eclipse 600 MHz spectrometer was used to record NMR spectra at 300 K. Spectra were recorded in parts per million for ^1H and ^{13}C . The coupling constants are expressed in Hz. The solvent peaks were used as a reference for the spectra.

2.1.4 Tangential Flow Filtration (TFF)

TFF was performed using an ultrafiltration cassette (Millipore Pellicon, MWCO 2 kDa) in a cassette holder (Sartorius). Using a peristaltic pump (Gibson), the solution was pumped through the system. Rotor speed was maintained at maximum operating.

2.1.5 Cell viability assay CCK-8

The cell viability assay “Cell Counting Kit 8” (CCK-8) from Sigma-Aldrich Chemie GmbH (Taufkirchen, Germany) was used to analyze the effect of the sulfated polymers on three different cell lines: A549 human lung carcinoma cells (DSMZ ACC 107), 16HBE14o- human bronchial epithelial cells (Millipore SCC150) and Vero E6 African green monkey kidney epithelial cells (ATCC CRL-1586). A549 and Vero E6 cells were cultured in Dulbecco’s Modified Eagle Medium (DMEM) and 16HBE14o- cells in Minimum Essential Media (MEM) supplemented with 10% fetal bovine serum, penicillin/streptomycin and GlutaMAX or Glutamine (all from Gibco BRL, Eggenstein, Germany). The cells were passaged every 3 to 4 days after reaching 70% to 90% confluency. The cell viability assay was done according to the manufactures’ instructions. In short, one day prior to the test cells were seeded in a 96 well plate (5*10⁵ cells in 90 μ l cell culture medium per well) and incubated over night at 37°C and 5% CO₂. 90 μ l of only cell culture medium without cells was added to the outer wells of the 96-well plates for later background subtraction. On the next day, serial dilutions of the compounds were prepared with water (MilliQ grade) and each concentration was added to three wells containing cells (each 10 μ l) and additionally to one outer well without cells. SDS (1%), solvent treated (MilliQ water) and non-treated cells served as controls. The well plates was incubated for another day at 37 °C before CCK-8 solution was added to each well (10 μ l). After approximately 3 hours absorbance was measured at a measurement wavelength of 450 nm and a reference wavelength of 650 nm with a plate reader (Infinite pro200, TECAN-reader Tecan Group Ltd., Männedorf, Switzerland). The assay was repeated three times. For

calculating the cell viability, the corrected absorbance (absorbance at measurement wavelength 450nm subtracted by the absorbance at reference wavelength 650nm) was used. For each control compound and concentration, the background was subtracted by using the respective corrected absorbance values of the wells without cells and subtracted this from the corrected absorbance of each of the three replicates. The cell viability was calculated by regarding the corrected and background subtracted absorbance of the non-treated control to 100% cell viability. The results are represented in a bar chart using the mean cell viability of the three repetitions with standard deviation.

2.1.6 Virus propagation and inhibition study

2.1.6.1 Virus propagation and virus titer determination by plaque assay

The GFP-tagged HSV-1 (provided by the Osterrieder Group, Institut für Virologie, Freie Universität Berlin), was propagated on Vero cells (ATCC CRL-81) and the supernatant containing GFP-tagged HSV-1 virions was collected. The virus titer was assessed using a plaque assay. For the plaque assay, Vero cells were pre-seeded in a 12-well plate for two days until confluency before adding 200 µl of virus containing solution for 45 minutes. Afterwards, 1 ml of 0.5% methylcellulose (Sigma M0262) was added as overlay medium. The infected cells were cultured for 2 days for plaque formation. The number of plaques per well was assessed using an epifluorescence microscope (Zeiss Axiovert 100) using the GFP channel. The titer of the initially added solution was calculated and expressed as plaque forming units (PFU)/mL.

2.1.6.2 Plaque reduction assay

The plaque reduction assay was performed according to our former reports.³ Vero cells were seeded in a 12-well plate until a confluent cell layer was formed. For the incubation, the compounds were diluted in 100 µL DMEM and then incubated with 100 µL of GFP-tagged HSV-1 solution (approx. 2000 PFU/mL) for 45 minutes at 37 °C. Afterwards, the infectivity of the mixture was titrated by a plaque assay using Vero cells as described above. The inhibition of the HSV-1 infection is calculated as follows:

$$Inhibition(\%) = \left(1 - \frac{Plaque\ number\ (sample)}{Plaque\ number\ (virus\ control)}\right) \times 100\%$$

S 1

Equation

The respective half maximal inhibitory concentration (IC₅₀) of each compound was estimated by using the software GraphPad Prism 7 and applying the dose-response model. The tests were done three times with individual experiments.

2.1.6.3 Virucidal assay

The compounds (1 mg/mL) were incubated with HSV-1 suspension containing approximately 1 × 10⁵ PFU for 1 h at 37 °C. Afterwards, the mixture was diluted 5 times 10-fold in DMEM to an endpoint of no active virions. The number of active virions was determined by plaque assay and virus titers were calculated back by the respective dilutions.

2.1.6.4 Pre and post cellular infection assays

Vero cells were seed in a 24 well-plate till 80% confluency. For pre infection assay, the cells were pre-incubated with DMEM containing inhibitors for 45min and then were infected by GFP-tagged HSV-1 at a multiplicity of infection (MOI) of 0.1. For post infection assay, the cells were firstly infected by GFP-tagged HSV-1 at an MOI of 0.1 for 1 hour, and then the compounds were added into the cell culture medium. After 48 hours, the cells were fixed by 2.5% formaldehyde and stained by DAPI to study the cellular infection using an epifluorescence microscope (Zeiss Axiovert 100).

2.1.7 Statistical Analysis

GraphPad 7 was used to analyze cell viability, plaque assay, virucidal assay and cellular infection assays. All values were compared to the control using an ANOVA analysis with Dunnett's multiple comparison correction. The significance value was set to $p=0.05$.

2.1.8 Fluorescent microscopy image analysis

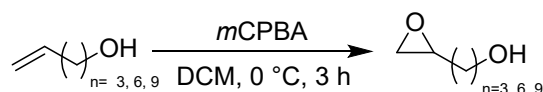
Image analysis was performed using self-written scripts in Fiji⁴ and MatLab (MathWorks, Natick, MA, USA). Cells were identified by nuclei staining, segmented by watershed transformation,⁵ and infection status was determined by GFP signal. The proportion of infected cells was calculated for four to five images per condition (Figure S4b and c).

2.1.9 Activated partial thromboplastin time (APTT)

The activated partial thromboplastin time (APTT) was determined on a STart Max coagulometer (Stago). Test samples were diluted to different concentrations in H₂O and 2 μ L of these solutions were added to 50 μ L of standard human plasma (Siemens Healthcare #ORKL175) mixed with 50 μ L of Actin FS (Siemens Healthcare #B4218-20) in a cuvette containing a steel ball. After incubation for 180s at 37°C, the cuvette was transferred to the measurement area of the device and the reaction was started by adding 50 μ L of CaCl₂ solution (Siemens Healthcare #ORH0375). The time until clot formation was recorded in seconds and each test was repeated three times. Different concentrations of heparin (Sigma-Aldrich/Merck # H3393-500kU, 201 USP units/ml) diluted in H₂O was used as a reference. Concentrations given refer to the final concentration of the sample in the Plasma+Actin solution (1:50).

3 Synthetic procedures

3.1 Synthesis of comonomers



Scheme S 1. Synthesis of 9-(oxiran-2-yl)nonan-1-ol, 6-(oxiran-2-yl)hexan-1-ol, and 3-(oxiran-2-yl)propan-1-ol through epoxidation using *m*CPBA.

The epoxidation of the substrates was carried out with *meta*-chloroperbenzoic acid (*m*CPBA) using Prilezhaev reaction with some modifications. Briefly, *m*CPBA (77%) was dissolved in DCM, dried over MgSO₄, and then filtered before it was used in the reactions. Then, 1.5 eq of the dried *m*CPBA solution in DCM (21.38 g, 123.8 mmol, 6.86 g, 39.78 mmol, and 10 g, 58.16 mmol) was added dropwise to the solutions of undec-10-en-1-ol (14 g, 82.58 mmol, 1 eq.), oct-7-en-1-ol (3.4 g, 26.52 mmol, 1 eq.), and pent-4-en-1-ol (3.34 g, 38.78 mmol, 1 eq.) in DCM, respectively. The reactions were stirred in 0 °C until the disappearance of the starting material (monitored by TLC). Afterward, the reactions were treated with 10 % aqueous sodium bisulfite followed by extraction from water (3 times), and finally brine. The combined organic phases were then dried over MgSO₄, filtered, and concentrated under reduced pressure. The crude products were finally purified using column chromatography on silica gel (5-30 % EtOAc-Cy). 9-(oxiran-2-yl)nonan-1-ol (11.8 g, 77 %), 6-(oxiran-2-yl)hexan-1-ol (3.1 g, 81 %), and 3-(oxiran-2-yl)propan-1-ol (1.9 g, 48 %) were obtained as colorless oils.

3.1.1 9-(oxiran-2-yl)nonan-1-ol

¹H NMR (500 MHz, CDCl₃) δ 3.65 – 3.55 (t, *J* = 6.6 Hz, 2H), 2.91 – 2.83 (p, *J* = 5.6, 3.0 Hz, 1H), 2.74 – 2.67 (t, *J* = 4.5 Hz, 1H), 2.46 – 2.39 (dd, *J* = 5.1, 2.7 Hz, 1H), 1.76 – 1.67 (s, 1H), 1.56 – 1.47 (m, 4H), 1.46 – 1.37 (dtd, *J* = 18.5, 7.2, 2.1 Hz, 2H), 1.35 – 1.23 (m, 10H). ¹³C NMR (126 MHz, CDCl₃) δ 62.88, 47.02, 32.75, 32.41, 29.42, 29.40, 29.35, 29.33, 25.89, 25.70. MS (ESI⁺): C₁₁H₂₂O₂ [Na⁺]: Calculated: 209.1492 *m/z*. Measured: 209.1516 *m/z*.

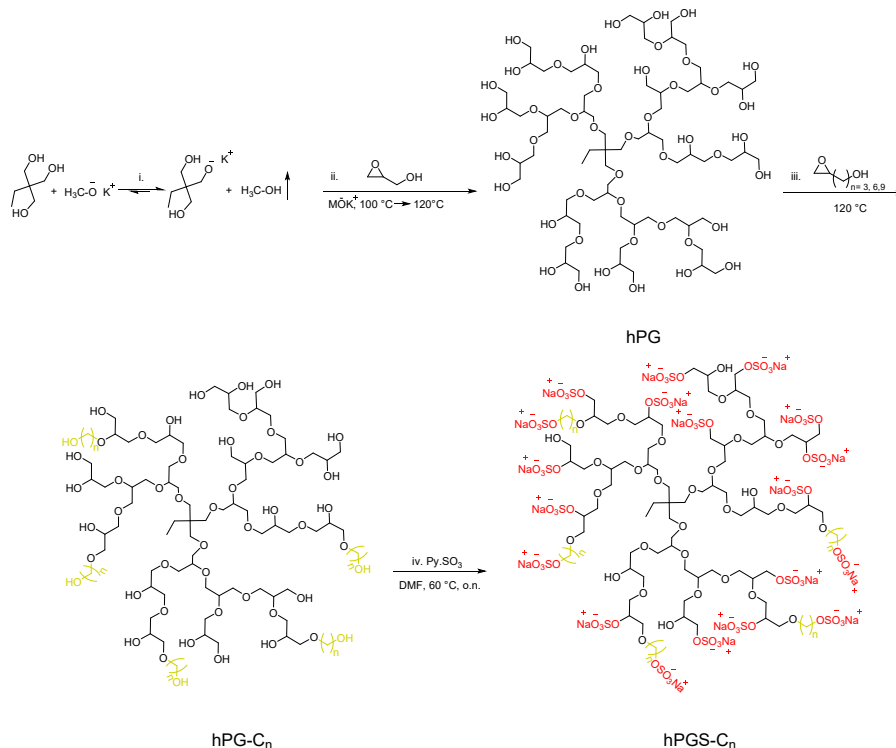
3.1.2 6-(oxiran-2-yl)hexan-1-ol

¹H NMR (600 MHz, CDCl₃) δ 3.53 – 3.41 (t, *J* = 6.7 Hz, 2H), 3.07 – 2.92 (s, 1H), 2.84 – 2.75 (p, *J* = 4.3 Hz, 1H), 2.68 – 2.59 (t, *J* = 4.6 Hz, 1H), 2.41 – 2.30 (m, 1H), 1.51 – 1.30 (m, 6H), 1.29 – 1.20 (m, 4H). ¹³C NMR (151 MHz, CDCl₃) δ 62.44, 52.44, 47.09, 32.53, 32.32, 29.17, 25.90, 25.66. MS (ESI⁺): C₈H₁₆O₂ [Na⁺]: Calculated: 167.1092 *m/z*. Measured: 167.1052 *m/z*.

3.1.3 3-(oxiran-2-yl)propan-1-ol

¹H NMR (600 MHz, DCM-d₂) δ 3.97 – 3.89 (qd, *J* = 6.8, 3.3 Hz, 2H), 2.83 – 2.76 (dd, 1H), 2.75 – 2.66 (dd, 1H), 3.44 – 3.37 (dd, *J* = 11.6, 6.3 Hz, 1H), 1.92 – 1.53 (m, 4H). ¹³C NMR (151 MHz, DCM-d₂) δ 59.62, 48.15, 44.85, 27.15, 26.00. MS (ESI⁺): C₅H₁₀O₂ [Na⁺]: Calculated: 125.0592 *m/z*. Measured: 125.0581 *m/z*.

3.2 One-pot synthesis approach to hPGS-C_n



Scheme S 2. Synthesis approach of hPGS-C_n by a one-pot, four-step procedure

Table S 1. Overview properties of the polymerizations.

	Glycidol [M1]		[M1]/ [I]	Theoretical M	Experimental M* (hPG)		Glycidol derivative [M2]		[M2]/ [I]	Experimental M* (hPG-C _n)		Overall Yield	Final M ** (hPGS-C _n)
	[g]	[mmol]			M _n [kDa]	Đ [-]	[g]	[mmol]		M _n [kDa]	Đ [-]		
hPGS-C ₉	7.31	98.4	70	5.0	3.8	1.7	11.0	59.10	42	9.7	1.5	13.8	12.1
hPGS-C ₆	1.32	17.9	70	5.0	3.9	1.8	1.55	10.74	42	6.6	1.8	4.1	11.5
hPGS-C ₃	0.36	4.9	70	5.0	3.9	1.8	0.30	3.0	42	6.7	1.7	0.9	10.6
hPGS-C ₀	0.37	4.9	70	5.0	4.6	1.7	-	-	-	-	-	0.7	11.3

* Measured by GPC in DMF (without any purifications). ** Calculated using ¹H NMR and Elemental analysis (See 3.2.3).

The polymerizations were all performed solvent-free in round-bottom flasks equipped with a mechanical stirrer under argon atmosphere according to our previously reported literature⁶ with some modifications. Briefly for hPGS-C₉, the flask was first heated to 140 °C under reduced pressure over night to ensure that water residues were completely removed. Following that, the flask was filled with argon and the temperature lowered to 60 °C. TMP (188.63 mg, 1.4 mmol, 1.0 eq.) was added at this point under argon circulation. The TMP was then melted under reduced pressure at 65 °C to eliminate any residual water content. To partially deprotonate TMP (~15 % of the OH groups), the temperature was lowered to 55 °C and 0.1 mL of methanolic potassium hydroxide solution (31.5 mg, 0.56 mmol, 0.4 eq.) was added and stirred for 1 h. Then, the pressure was reduced, and the temperature increased to 100 °C for an hour in order to evaporate methanol. The flask was next flushed with argon and distilled glycidol (7.3 g, 98.4 mmol, 70.0 eq.) was slowly added to the reaction over a period of three hours using a syringe pump. In order to assure that no unreacted monomer remains, the reaction condition was maintained for 6 hours followed by another 2 hours at 120 °C. Then, the distilled comonomer, 9-(oxiran-2-yl)nonan-1-ol, (11 g, 59.1 mmol, 42 eq.)

was added slowly to the reaction over a period of 3 hours and stirred for another 3 hours at 120°C. Half of the resulting product, namely hPG-C₉, was taken and placed in the fridge for later uses. As for the rest of the obtained product (7.21 g, 97.30 mmol OH groups) in the flask, it was diluted in anhydrous DMF, lowered to 60 °C, and sulfated *in situ* by adding sulfur trioxide pyridine complex in anhydrous DMF (23.2 g, 145.9 mmol, 1.5 eq. of mol of OH groups). The reaction was stirred overnight at 60 °C. At the end of the reaction, the mixture was diluted with water, followed by neutralization with 1 M NaOH to pH 11. To purify the product, an aqueous polymer solution was circulated over an ultrafiltration membrane (2 kDa MWCO) for 72 hours using TFF. Small polymers fractions and impurities were removed during the filtration *via* permeation and replaced with fresh brine continuously. Gradually, brine solution was replaced with deionized water. In the end, the product hPGS-C₉ was obtained by freeze-drying (13.8 g). Similar procedure was applied to synthesis hPGS-C₆, and hPGS-C₃. The properties of all

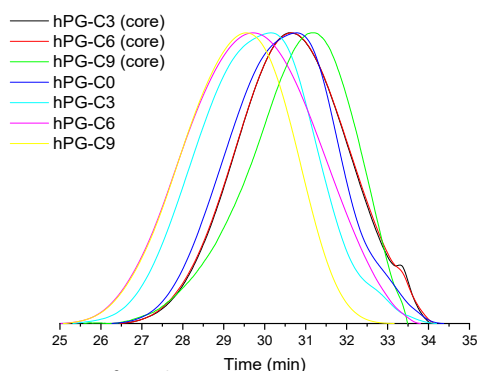


Figure S 1. GPC of synthesized polymers.

polymerizations are listed in Table S1.

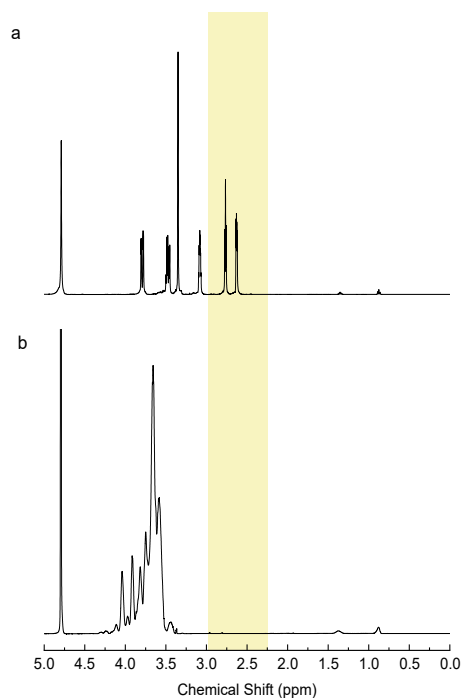


Figure S 2. ¹H NMR spectra of the reaction a) at time 0 h and b) upon adding the comonomer.

3.2.1 Degree of functionalization (DF)

The degree of functionalization was calculated using the integrals measured by $^1\text{H-NMR}$ in Figure S6 and Equation S1-S3 for hPGS-C₉, hPGS-C₆, and hPGS-C₃ respectively.

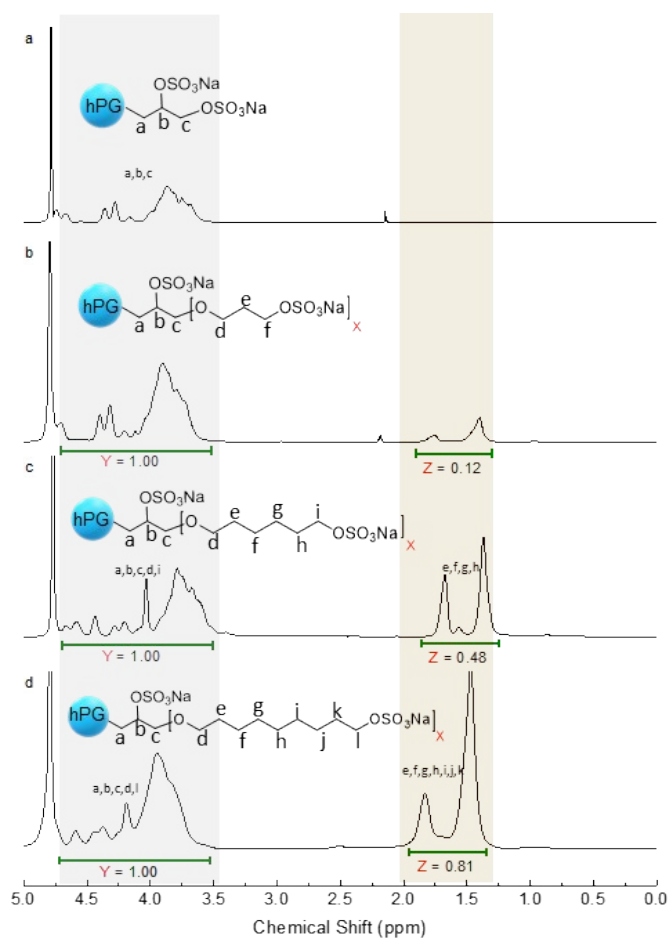


Figure S 3. ^1H NMR spectra of a) hPGS-C₀, b) hPGS-C₃, c) hPGS-C₆, and d) hPGS-C₉ in D₂O.

$$\begin{cases} Y=5+4x \\ Z=14x \\ Z/Y=0.81 \end{cases}$$

$$\rightarrow \text{DF}_{\text{hPGS-C}_9} = 38\%$$

Equation S 2

$$\begin{cases} Y=5+4x \\ Z=8x \end{cases}$$

$$\rightarrow \text{DF}_{\text{hPGS-C}_6} = 39\%$$

Equation S 3

$$Z/Y = 0.48$$

$$\left\{ \begin{array}{l} Y=5+4x \\ Z=2x \\ Z/Y=0.12 \end{array} \right. \rightarrow \text{DF}_{\text{hPGS-C}_3} = 39\% \quad \text{Equation S 4}$$

3.2.2 Degree of sulfation (DS)

On the basis of the sulfur content obtained by elemental analysis (Table S 2), equation S4-S7 were used to calculate the DS of hPGS-C₉, hPGS-C₆, hPGS-C₃, and hPGS-C₀, respectively.

Table S 2. Elemental analysis of the synthesized polymers.

Compound	C (%)	H (%)	N (%)	S (%)
hPGS-C ₉	27.61	5.06	0.03	15.07
hPGS-C ₆	26.59	4.61	0.03	15.10
hPGS-C ₃	19.78	4.63	0.01	16.58
hPGS-C ₀	20.39	3.21	0.02	16.51

$$\text{DS (hPGS-C}_n) = \frac{S\% \text{ (experimental (obtained from EA))}}{S\%_t \text{ (total S\% in case of 100\% sulfation)}} \quad \text{Equation S 5}$$

where

$$S\%_t = \text{DF} * \underbrace{(S_n \%)}_{\text{Theoretical S\% of } \text{C}_n\text{H}_n\text{O}_n\text{SO}_3\text{Na}} + (1-\text{DF}) * \underbrace{(18.2)}_{\text{Theoretical S\% of } \text{C}_1\text{H}_1\text{O}_1\text{SO}_3\text{Na}} \quad \text{Equation S 6}$$

$$\text{DS}_{\text{hPGS-C}_9} = \frac{15.07}{0.38 * 11.12 + 0.62 * 18.2} * 100\% = 97\% \quad \text{Equation S 7}$$

$$\text{DS}_{\text{hPGS-C}_6} = \frac{15.10}{0.39 * 13.02 + 0.61 * 18.2} * 100\% = 93\% \quad \text{Equation S 8}$$

$$\text{DS}_{\text{hPGS-C}_3} = \frac{16.58}{0.39 * 15.70 + 0.61 * 18.2} * 100\% = 96\% \quad \text{Equation S 9}$$

$$\text{DS}_{\text{hPGS-C}_0} = \frac{16.51}{18.2} * 100\% = 91\% \quad \text{Equation S 10}$$

3.2.3 Molecular weight

According to Equation S 12-15, the final molecular weight of each compound can be approximately calculated by using the DF, DS, and Mn values.

$$\text{Total Number of OH}_{hPGS-C_9} = \frac{3800}{74} = 51 \quad \text{Equation S 11}$$

$$\text{Total Number of OH}_{hPGS-C_6} = \frac{3900}{74} = 53 \quad \text{Equation S 12}$$

$$\text{Total Number of OH}_{hPGS-C_3} = \frac{3900}{74} = 53 \quad \text{Equation S 13}$$

$$\text{Total Number of OH}_{hPGS-C_0} = \frac{4600}{74} = 62 \quad \text{Equation S 14}$$

$$\text{Molecular weight (hPGS-C}_9\text{)} = \overbrace{3800}^{\text{Weight of hPG core (from GPC)}} - \underbrace{51 \cdot 0.97 \cdot 1.01}_{\text{Weight of H that was substituted}} + \overbrace{51 \cdot 0.38 \cdot 245.29}^{\text{-C9-OSO}_3\text{Na}} + \underbrace{51 \cdot (0.97 - 0.38) \cdot 119.05}_{\text{-OSO}_3\text{Na}} = 12.1 \text{ kDa}$$

Equation S 15

$$\text{Molecular weight (hPGS-C}_6\text{)} = \overbrace{3900}^{\text{Weight of hPG core (from GPC)}} - \underbrace{53 \cdot 0.93 \cdot 1.01}_{\text{Weight of H that was substituted}} + \overbrace{53 \cdot 0.39 \cdot 204.22}^{\text{-C6-OSO}_3\text{Na}} + \underbrace{53 \cdot (0.93 - 0.39) \cdot 119.05}_{\text{-OSO}_3\text{Na}} = 11.5 \text{ kDa}$$

Equation S 16

$$\text{Molecular weight (hPGS-C}_3\text{)} = \overbrace{3900}^{\text{Weight of hPG core (from GPC)}} - \underbrace{53 \cdot 0.93 \cdot 1.01}_{\text{Weight of H that was substituted}} + \overbrace{53 \cdot 0.39 \cdot 161.13}^{\text{-C3-OSO}_3\text{Na}} + \underbrace{53 \cdot (0.93 - 0.39) \cdot 119.05}_{\text{-OSO}_3\text{Na}} = 10.6 \text{ kDa}$$

Equation S 17

$$\text{Molecular weight (hPGS-C}_0\text{)} = \overbrace{4600}^{\text{Weight of hPG core (from GPC)}} - \underbrace{62 \cdot 0.91 \cdot 1.01}_{\text{Weight of H that was substituted}} + \overbrace{62 \cdot 0.91 \cdot 119.05}^{\text{-OSO}_3\text{Na}} = 11.3 \text{ kDa}$$

Equation S 18

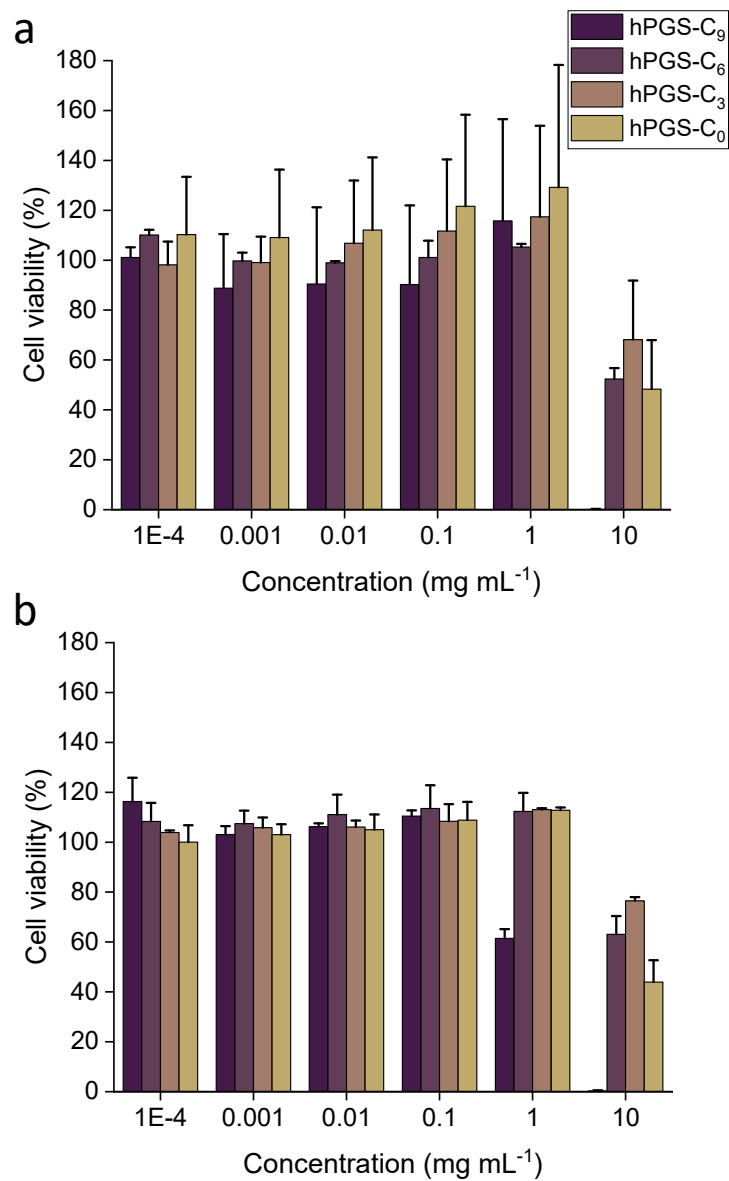


Figure S 4. Cytotoxicity profile of the synthesized inhibitors determined by a CCK-8 assay using (a) A549 and (b) 16HBE14o-. The cell viability of compound treated cells is normalized to the cell viability of non-treated cells that was

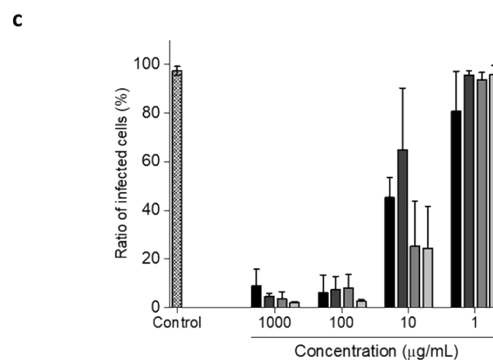
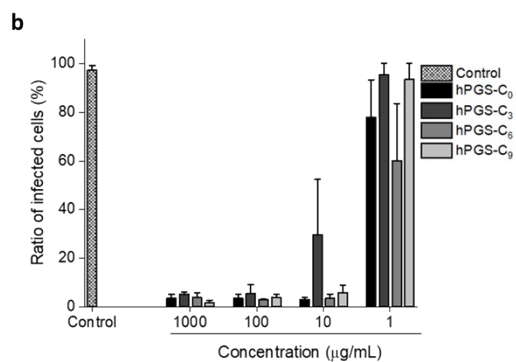
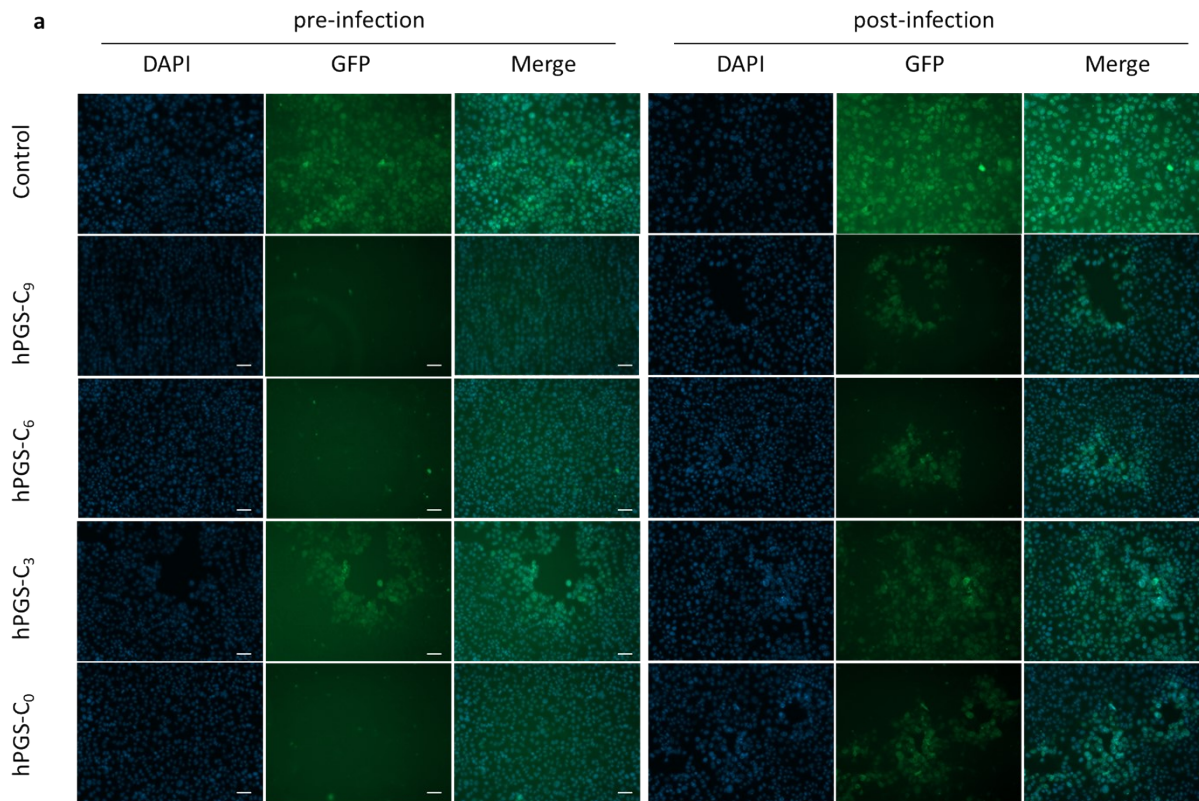


Figure S 5. a) fluorescent microscopy images of infected cells for pre- and post-infection assay for all the compounds with a concentration of 10 μg/mL. Scale bar: 20 μm. Cell nuclei are marked in blue, and infected cells in green. Ratios of infected cells for each compound obtained from b) pre-infection and c) post-infection assay. (Control: DMEM medium). Values are expressed as mean ± SD, n = 4.

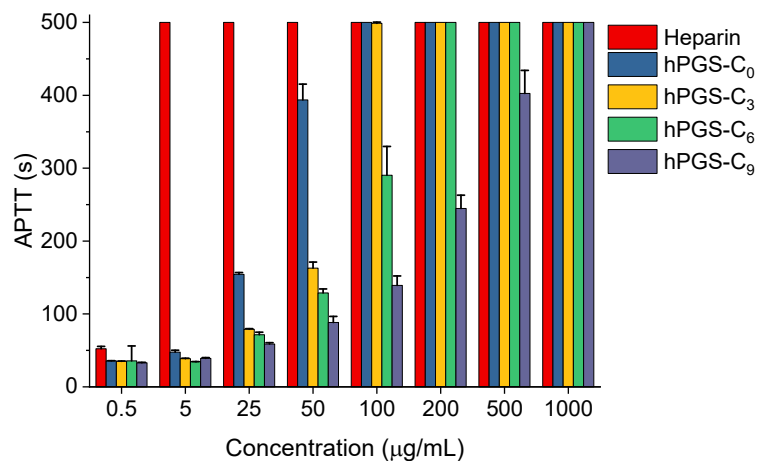


Figure S6. The APTT for synthetic inhibitors and heparin. Untreated human plasma with APTT of 31s was used as a control. Data are expressed as mean \pm SD (n=3). x-axis gives concentration in $\mu\text{g mL}^{-1}$.

4 References

1. A. Sunder, R. Hanselmann, H. Frey and R. Mülhaupt, *Macromolecules*, 1999, **32**, 4240-4246.
2. H. Türk, R. Haag and S. Alban, *Bioconjugate Chemistry*, 2004, **15**, 162-167.
3. P. Pouyan, C. Nie, S. Bhatia, S. Wedepohl, K. Achazi, N. Osterrieder and R. Haag, *Biomacromolecules*, 2021, **22**, 1545-1554.
4. J. Schindelin, I. Arganda-Carreras, E. Frise, V. Kaynig, M. Longair, T. Pietzsch, S. Preibisch, C. Rueden, S. Saalfeld, B. Schmid, J. Y. Tinevez, D. J. White, V. Hartenstein, K. Eliceiri, P. Tomancak and A. Cardona, *Nat Methods*, 2012, **9**, 676-682.
5. L. Vincent and P. Soille, *IEEE Transactions on Pattern Analysis and Machine Intelligence*, 1991, **13**, 583-598.
6. M. Wallert, J. Plaschke, M. Dimde, V. Ahmadi, S. Block and R. Haag, *Macromolecular Materials and Engineering*, 2021, **306**, 2000688.

3.3 Amphiphilic Co-polypeptides Self-Assembled into Spherical Nanoparticles for Dermal Drug Delivery

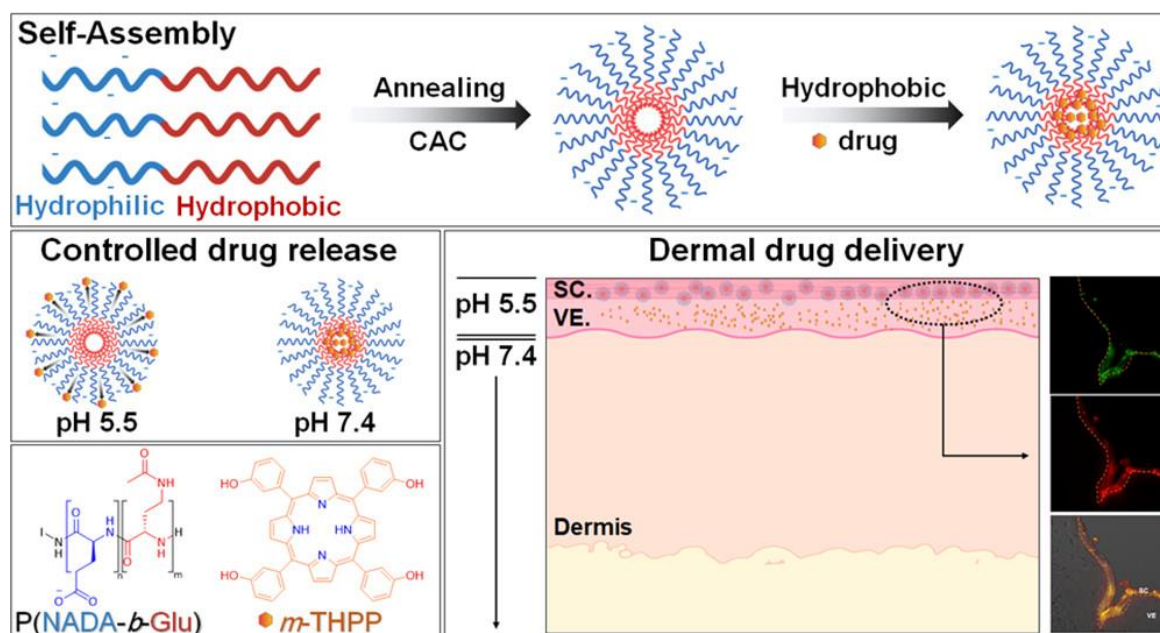


Figure 27. Reprinted with permission from Ref. [228]. Copyright 2021 American Chemistry Society.

Vahid Ahmadi, Fatemeh Zabihi, Fiorenza Rancan, Arthur Alexander Staszak, Chuanxiong Nie, Mathias Dimde, Katharina Achazi, Arno Wiehe, Annika Vogt, and Rainer Haag*

ACS Appl. Nano Mater. **2021**, 4, 7, 6709–6721

<https://doi.org/10.1021/acsnm.1c00693>

Authors contribution:

Vahid Ahmadi contributed to the concept, performed the synthesis and characterization, and evaluated the data as well as wrote the manuscript. Fatemeh Zabihi, Fiorenza Rancan, and Annika Vogt supported with the skin penetration tests. The synthesis was partly assisted by Arthur Alexander Staszak. Chuanxiong Nie conducted TEM analysis. Katharian Achazi performed the cell viability assay as well as the cellular uptake pathway. Arno Wiehe provided mTHPP. Rainer Haag supervised the project and edited the manuscript.

4 Conclusion

In this work, the focus was on the development of novel functional polymers with defined architecture for biointerface interactions. With this goal in mind, a 2D polymer in the first project was synthesized and compared to its 3D counterpart. In this regard, a new bottom-up method to synthesize two-dimensional polymers using graphene as a 2D template has been developed to meet this challenge. A layer of hPG containing 10% azide functional groups has been covalently attached to a functional graphene scaffold using pH-sensitive linkers. In addition, crosslinking of the hPG units was performed using tripropargylamine loaded on the surface of graphene. The hPG nanosheets were subsequently detached from graphene through acidification and centrifugation to yield 2D-hPG. This synthetic method relied on noncovalent interactions between the crosslinker and graphene template to control lateral crosslinking of hPG branches. Then, the nanosheets were sulfated to mimic the heparin sulfate proteoglycans, resulting in 2D-hPGS. 3D analogs of the nanosheets, namely 3D-hPG and 3D-hPGS, were synthesized that were of equivalent sizes, to investigate the role that two-dimensionality plays in nano-bio interactions. As a result of this research, 2D-hPGS was able to serve as an extracellular matrix mimic that was able to inhibit the replication of representative enveloped viruses, including HSV-1 and SARS-CoV-2. A comparison of the inhibitory efficacy of 2D-hPGS to its 3D analogues (3D-hPGS) found the former to be around four times stronger. The superiority of the 2D inhibitor over its 3D counterpart is attributed to the high aspect ratio and multivalent interactions of 2D-hPGS as compared to those of 3D analogs.

The findings from the study of nano-bio-interactions of synthesized extracellular matrix mimics in the first project led us to develop alternative polymer architectures in the second project, which are easy to synthesize and scale up. Furthermore, the main objective of this project was to develop virucidal compounds, therefore the compounds were rationally designed in a synergistic manner using alkyl chains and sulfate moieties for hydrophobic and electrostatic interactions, respectively. This was achieved by developing a one-pot reaction involving a four-step synthesis approach to engineer highly sulfated hPG with sulfated alkyl chains. The synthesis of hPG was performed using an anionic ring-opening polymerization method, then modified with hydrophobic alkyl chains and sulfated to encourage electrostatic interactions with the virus. Compounds with varying alkyl chain lengths were synthesized in a similar way to make hPGS-C₃, hPGS-C₆, and hPGS-C₉ to elaborate the role of the

hydrophobic alkyl chains on virucidal properties. All compounds exhibited significant inhibitory effects against HSV-1, as evidenced by IC₅₀ values in the nanomolar range. The compounds with shorter alkyl chains, hPGS-C₆ and hPGS-C₃, as well as hPGS-C₀, exhibited only virustatic activity, while hPGS-C₉ showed irreversible virucidal activities. In this way, due to the increase in hydrophobicity resulting from longer alkyl chains, virucidal effects may be induced, which signifies that sufficiently long alkyl chains can rupture viral envelopes.

In the first two projects, functional polymers with different architectures were developed that can be used for nano-bio interactions *in vitro*. In the third project, block copolymer architectures were developed, however, this time for a more advanced *ex vivo* skin penetration study and drug delivery through the skin. To this end, block-co-polypeptides of p(l-glutamic acid)-*b*-p(*N*γ-acetyl-l-2,4-diaminobutyric acid) with different hydrophobic-hydrophilic ratios, named P(Glu_x-*b*-NADA_y), were synthesized *via* a combination of NCA and condensation-activated monomer polymerization. The nanocarriers were loaded with 5,10,15,20-tetrakis(3-hydroxyphenyl)porphyrin (*m*-THPP), a derivative of the recognized photosensitizer 5,10,15,20-tetrakis(3-hydroxyphenyl)chlorin (*m*-THPC, temoporfin). According to the results, the drug loading capacity of the block-co-polypeptides was dependent upon their composition and the one with moderate hydrophobic content, P(Glu₅₅-*b*-NADA₂₀), was found to have a maximum loading capacity (~4 wt.%). In aqueous solutions, this co-polypeptide self-assembled and formed solid nanoparticles with an average size of 200 nm. In addition, the nanocarrier improved the release of its cargo (*m*-THPP) in pH 5.5-6.5 at a temperature of 32 °C, which is similar to skin conditions. Furthermore, a copolymer with similar molecular weight and hydrophobic content but positively charged, P(Lys₄₀-*b*-NADA₂₀), as well as the homopolymers P(Glu₄₀) and P(Lys₄₀) were also synthesized and stained with FITC to examine whether the surface charge and the amphiphilicity contribute to these nano-bio interactions. Fluorescently labeled P(Glu₅₅-*b*-NADA₂₀) and P(Lys₄₀-*b*-NADA₂₀) showed interaction and localization within the uppermost layer of human skin, stratum corneum, following 18 hours of incubation. In contrast, P(Lys₄₀) and P(Glu₄₀) showed no interaction with the stratum corneum in fluorescence images. Hydrophilicity of homopolymers could be a factor preventing their interactions with skin. The results revealed that P(Glu₅₅-*b*-NADA₂₀) and P(Lys₄₀-*b*-NADA₂₀) increased *m*-THPP penetration by 12-fold and 9-fold, respectively, over the commercially available base creams. Therefore, the negatively charged nanocarriers could improve the penetration of the drug to the viable skin layers more effectively than the positively one and cream formulations. These

differences arise from the different surface functionalities, each of which interacts differently with the skin barriers, which ultimately determines how loaded cargos are delivered to the skin.

5 Short summary

This work focused on the development of new functional polymers with defined architectures for biointerface interactions. The first project was a comparative study of a 2D polymer and its 3D counterpart. To this end, a bottom-up approach using graphene as a 2D template was developed to synthesize two-dimensional hyperbranched polyglycerol (2D-hPG). A layer of hPG bearing azide functional groups was attached to a graphene template using acid-sensitive linkers. Next, using tripropargylamine loaded on the surface of graphene, lateral cross-linking of the polyglycerol units was performed. Following this, the nanosheets were detached and then separated from the graphene through acidification and centrifugation, respectively. Afterward, nanosheets were sulfated to yield heparin mimicking sulfate proteoglycan (2D-hPGS). Aiming to examine the relevance of two-dimensionality in bio-nano interactions, 3D equivalents of the nanosheets with similar average sizes and surface charges were synthesized. The results of this study showed that 2D-hPGS was able to act as an extracellular matrix mimic and inhibit the replication of enveloped viruses, such as HSV-1 and SARS-CoV-2. The inhibitory effect of 2D-hPGS is approximately four times better than that of its 3D analogs (3D-hPGS). The superiority of the 2D inhibitor over its 3D spherical counterpart can be attributed to the high aspect ratio of the 2D-hPGS. Based on our findings from the first project on the nano-bio interactions of synthesized extracellular matrix mimics, a second project to develop alternative polymeric architectures that can be synthesized and scaled up with ease was designed. In addition, the project aimed to develop an antiviral compound with virucidal properties. Therefore, the compounds were designed in a synergistic manner by using alkyl chains for hydrophobic interactions and sulfate moieties for electrostatic interactions. The development of highly sulfated hPG containing sulfated alkyl chains was obtained using a one-pot reaction. Increasing the length of the alkyl chains resulted in higher hydrophobicity and thus virucidal activity was achieved. Against HSV-1, compounds with short (C_3) and medium (C_6) alkyl chains demonstrated strong antiviral activity with IC_{50} values in the nanomolar range yet provided only virustatic properties. In contrast, the one with long alkyl chains (C_9) exhibited irreversible virucidal properties. The first two projects focused on the development of polymers with diverse architectures to be used in nano-bio interactions *in vitro*. In the third project, block-*co*-polymer architectures were developed aimed at an *ex vivo* skin penetration and dermal drug delivery study. Toward this end, a series of anionic amphiphilic block-*co*-polypeptides with different hydrophobic to hydrophilic ratios have been synthesized using NCA and condensation-activated monomer

polymerization. The nanocarriers were loaded with *m*-THPP. According to the results, the loading capacity of the block-co-polypeptides with moderate hydrophobic content was found to be maximum (4 wt.%). The nanocarriers also self-assembled into approximately 200 nm solid nanoparticles in an aqueous solution and improved the release of *m*-THPP in an acidic environment (pH 5.5-6.5) at a temperature of 32 °C, which is similar to that found on the skin surface.

6 Kurzzusammenfassung

Ziel dieser Arbeit war die Entwicklung neuer funktioneller Polymere mit kontrollierten Architekturen für die Interaktion mit Bioschnittstellen. Das erste Projekt war eine vergleichende Studie eines 2D-Polymers und seines 3D-Gegenstücks. Zu diesem Zweck wurde ein Bottom-up-Ansatz mit Graphen als 2D-Vorlage entwickelt, um zweidimensionales hyperverzweigtes Polyglycerin (2D-hPG) zu synthetisieren. Eine Schicht aus hPG, die funktionelle Azidgruppen trägt, wurde mit Hilfe säureempfindlicher Linker an eine Graphenvorlage gebunden. Anschließend wurden die Polyglycerin-Einheiten mit Hilfe von Tripropargylamin auf der Graphenoberfläche lateral vernetzt. Anschließend wurden die Nanoblätter abgelöst und durch Ansäuern bzw. Zentrifugieren vom Graphen getrennt. Um Heparinsulfat-Proteoglykane zu imitieren, wurde 2D-hPG sulfatiert, was zu 2D-hPGS führte. Um die Rolle der Zweidimensionalität bei Bio-Nano-Wechselwirkungen zu untersuchen, wurden 3D-Analoga der Nanosheets mit ähnlichen Durchschnittsgrößen und Oberflächenladungen synthetisiert. Die Ergebnisse dieser Studie zeigt, dass 2D-hPGS in der Lage war, als extrazelluläre Matrixnachahmung zu fungieren und die Replikation von behüllten Viren wie HSV-1 und SARS-CoV-2 zu hemmen. Die hemmende Wirkung von 2D-hPGS ist etwa viermal besser als die seiner 3D-Analoga (3D-hPGS). Die Überlegenheit des 2D-Hemmstoffs gegenüber seinem sphärischen 3D-Gegenstück kann auf das hohe Seitenverhältnis des 2D-hPGS zurückgeführt werden. Auf der Grundlage unserer Erkenntnisse aus dem ersten Projekt über die Nano-Bio-Wechselwirkungen von synthetisierten extrazellulären Matrixnachbildungen wurde ein zweites Projekt zur Entwicklung alternativer Polymerarchitekturen konzipiert, die sich leicht synthetisieren und in größerem Maßstab herstellen lassen. Darüber hinaus zielte das Projekt auf die Entwicklung einer antiviralen Verbindung mit viruziden Eigenschaften ab. Daher wurden die Verbindungen auf synergistische Weise entwickelt, indem Alkylketten für hydrophobe Wechselwirkungen und Sulfateinheiten für elektrostatische Wechselwirkungen verwendet wurden. Die Entwicklung von hoch sulfatiertem hPG, das sulfatierte Alkylketten enthält, wurde durch eine Eintopfreaktion erreicht. Mit zunehmender Länge der Alkylketten wurde eine höhere Hydrophobie und damit eine viruzide Aktivität erzielt. Gegen HSV-1 zeigten die Verbindungen mit kurzen (C_3) und mittleren (C_6) Alkylketten eine starke antivirale Aktivität mit IC_{50} -Werten im nanomolaren Bereich, aber nur virustatische Eigenschaften. Die Verbindung mit langen Alkylketten (C_9) hingegen wies irreversible viruzide Eigenschaften auf. Die ersten beiden Projekte konzentrierten sich auf die Entwicklung von Polymeren mit

unterschiedlichen Architekturen, die für Nano-Bio-Interaktionen *in vitro* verwendet werden sollen. Im dritten Projekt werden Block-Co-Polymer-Architekturen für eine Studie zur *ex vivo* Hautpenetration und dermalen Wirkstoffabgabe entwickelt. Zu diesem Zweck wurde eine Reihe von anionischen amphiphilen Block-Co-Polypeptiden mit unterschiedlichen hydrophoben zu hydrophilen Verhältnissen mittels NCA und kondensationsaktivierter Monomer polymerisation synthetisiert. Die Nanocarrier wurden mit *m*-THPP beladen. Die Ergebnisse zeigen, dass die Beladungskapazität der Block-Co-Polypeptide mit moderatem hydrophobem Anteil am höchsten ist (4 Gew.-%). Die Nanoträger formten in einer wässrigen Lösung feste Nanopartikel mit einer Größe von ca. 200 nm und verbesserten die Freisetzung von *m*-THPP in einer sauren Umgebung (pH-Wert 5,5-6,5) bei einer Temperatur von 32 °C, die derjenigen auf der Hautoberfläche ähnlich ist.

7 References

- [1] R. P. Feynman, in *Engineering and Science*, Vol. 23, California Institute of Technology, **1960**, pp. 22-36.
- [2] N. Taniguchi, in *Proceedings of the International Conference on Production Engineering*, Tokyo, **1974**, pp. 5-10.
- [3] F. Allhoff, P. Lin, D. Moore, *What is nanotechnology and why does it matter?: from science to ethics*, John Wiley and Sons, **2010**.
- [4] G. Guisbiers, S. Mejía-Rosales, F. Leonard Deepak, *Journal of Nanomaterials* **2012**, 2012, 180976.
- [5] M. A. Cotta, *ACS Applied Nano Materials* **2020**, 3, 4920-4924.
- [6] S. Gong, W. Cheng, *Advanced Electronic Materials* **2017**, 3, 1600314.
- [7] M.-H. Kang, D. Lee, J. Sung, J. Kim, B. H. Kim, J. Park, in *Comprehensive Nanoscience and Nanotechnology (Second Edition)* (Eds.: D. L. Andrews, R. H. Lipson, T. Nann), Academic Press, Oxford, **2019**, pp. 55-90.
- [8] P. Dey, T. Bergmann, J. L. Cuellar-Camacho, S. Ehrmann, M. S. Chowdhury, M. Zhang, I. Dahmani, R. Haag, W. Azab, *ACS Nano* **2018**, 12, 6429-6442.
- [9] S. Das, S. Mitra, S. M. P. Khurana, N. Debnath, *Frontiers in Life Science* **2013**, 7, 90-98.
- [10] K. McNamara, S. A. M. Tofail, *Advances in Physics: X* **2017**, 2, 54-88.
- [11] D. Bobo, K. J. Robinson, J. Islam, K. J. Thurecht, S. R. Corrie, *Pharmaceutical Research* **2016**, 33, 2373-2387.
- [12] W. Wang, H. Mattoussi, *Accounts of Chemical Research* **2020**, 53, 1124-1138.
- [13] Q. Wei, J. He, W. Zhao, Y. Chen, *International Journal of Polymer Science* **2017**, 2017, 2474397.
- [14] Y. Wang, R. Cai, C. Chen, *Accounts of Chemical Research* **2019**, 52, 1507-1518.
- [15] E. Mohammadifar, A. Bodaghi, A. Dadkhahtehrani, A. Nemati Kharat, M. Adeli, R. Haag, *ACS Macro Letters* **2017**, 6, 35-40.
- [16] F. Zabihi, H. Koeppe, K. Achazi, S. Hedtrich, R. Haag, *Biomacromolecules* **2019**, 20, 1867-1875.
- [17] A. L. Sisson, D. Steinhilber, T. Rossow, P. Welker, K. Licha, R. Haag, *Angewandte Chemie International Edition* **2009**, 48, 7540-7545.
- [18] F. Asghari, M. Samiei, K. Adibkia, A. Akbarzadeh, S. Davaran, *Artificial Cells, Nanomedicine, and Biotechnology* **2017**, 45, 185-192.

- [19] M. Cherri, M. Ferraro, E. Mohammadifar, E. Quaas, K. Achazi, K. Ludwig, C. Grötzinger, M. Schirner, R. Haag, *ACS Biomaterials Science & Engineering* **2021**, *7*, 2569-2579.
- [20] E. Mohammadifar, F. Zabihi, Z. Tu, S. Hedtrich, A. Nemati Kharat, M. Adeli, R. Haag, *Polymer Chemistry* **2017**, *8*, 7375-7383.
- [21] D. Braatz, M. Dimde, G. Ma, Y. Zhong, M. Tully, C. Grötzinger, Y. Zhang, A. Mavroskoufis, M. Schirner, Z. Zhong, M. Ballauff, R. Haag, *Biomacromolecules* **2021**, *22*, 2625-2640.
- [22] F. Reisbeck, A. Ozimkovski, M. Cherri, M. Dimde, E. Quaas, E. Mohammadifar, K. Achazi, R. Haag, *Polymers* **2021**, *13*, 982.
- [23] R. Bej, K. Achazi, R. Haag, S. Ghosh, *Biomacromolecules* **2020**, *21*, 3353-3363.
- [24] L. Gao, F. Zabihi, S. Ehrmann, S. Hedtrich, R. Haag, *J Control Release* **2019**, *300*, 64-72.
- [25] Y. K. Sung, S. W. Kim, *Biomaterials Research* **2020**, *24*, 12.
- [26] P. Bhatt, S. Trehan, N. Inamdar, V. K. Mourya, A. Misra, in *Applications of Polymers in Drug Delivery (Second Edition)* (Eds.: A. Misra, A. Shahiwala), Elsevier, **2021**, pp. 1-42.
- [27] P. Pouyan, C. Nie, S. Bhatia, S. Wedepohl, K. Achazi, N. Osterrieder, R. Haag, *Biomacromolecules* **2021**, *22*, 1545-1554.
- [28] M. Wallert, C. Nie, P. Anilkumar, S. Abbina, S. Bhatia, K. Ludwig, J. N. Kizhakkedathu, R. Haag, S. Block, *Small* **2020**, *16*, 2004635.
- [29] S. Bhatia, M. Hilsch, J. L. Cuellar-Camacho, K. Ludwig, C. Nie, B. Parshad, M. Wallert, S. Block, D. Lauster, C. Böttcher, A. Herrmann, R. Haag, *Angewandte Chemie International Edition* **2020**, *59*, 12417-12422.
- [30] M. Li, C. Schlaich, J. Zhang, I. S. Donskyi, K. Schwibbert, F. Schreiber, Y. Xia, J. Radnik, T. Schwerdtle, R. Haag, *Journal of Materials Science & Technology* **2021**, *68*, 160-171.
- [31] F. Xiao, B. Cao, C. Wang, X. Guo, M. Li, D. Xing, X. Hu, *ACS Nano* **2019**, *13*, 1511-1525.
- [32] S. Bai, J. Wang, K. Yang, C. Zhou, Y. Xu, J. Song, Y. Gu, Z. Chen, M. Wang, C. Shoen, B. Andrade, M. Cynamon, K. Zhou, H. Wang, Q. Cai, E. Oldfield, S. C. Zimmerman, Y. Bai, X. Feng, *Science Advances* **2021**, *7*, eabc9917.
- [33] K. Pant, C. Neuber, K. Zarschler, J. Wodtke, S. Meister, R. Haag, J. Pietzsch, H. Stephan, *Small* **2020**, *16*, 1905013.
- [34] K. Huth, M. Glaeske, K. Achazi, G. Gordeev, S. Kumar, R. Arenal, S. K. Sharma, M. Adeli, A. Setaro, S. Reich, R. Haag, *Small* **2018**, *14*, 1800796.

- [35] C. Dong, Z. Liu, J. Liu, C. Wu, F. Neumann, H. Wang, M. Schäfer-Korting, B. Kleuser, J. Chang, W. Li, N. Ma, R. Haag, *Advanced Healthcare Materials* **2016**, *5*, 2214-2226.
- [36] Y. Braeken, S. Cheruku, A. Ethirajan, W. Maes, *Materials (Basel, Switzerland)* **2017**, *10*, 1420.
- [37] M. E. Fox, F. C. Szoka, J. M. J. Fréchet, *Accounts of Chemical Research* **2009**, *42*, 1141-1151.
- [38] N. Nasongkla, B. Chen, N. Macaraeg, M. E. Fox, J. M. J. Fréchet, F. C. Szoka, *Journal of the American Chemical Society* **2009**, *131*, 3842-3843.
- [39] M. G. McKee, S. Unal, G. L. Wilkes, T. E. Long, *Progress in Polymer Science* **2005**, *30*, 507-539.
- [40] P. J. Flory, *Journal of the American Chemical Society* **1952**, *74*, 2718-2723.
- [41] Y. Zheng, S. Li, Z. Weng, C. Gao, *Chemical Society Reviews* **2015**, *44*, 4091-4130.
- [42] B. I. Voit, A. Lederer, *Chemical Reviews* **2009**, *109*, 5924-5973.
- [43] S. Abbina, S. Vappala, P. Kumar, E. M. J. Siren, C. C. La, U. Abbasi, D. E. Brooks, J. N. Kizhakkedathu, *Journal of Materials Chemistry B* **2017**, *5*, 9249-9277.
- [44] M. Calderón, M. A. Quadir, S. K. Sharma, R. Haag, *Adv Mater* **2010**, *22*, 190-218.
- [45] N. Rades, K. Licha, R. Haag, *Polymers* **2018**, *10*, 595.
- [46] C. Holzhausen, D. Gröger, L. Mundhenk, C. K. Donat, J. Schnorr, R. Haag, A. D. Gruber, *Journal of Nanoparticle Research* **2015**, *17*, 116.
- [47] M. Elsbahy, K. L. Wooley, *Chemical Society reviews* **2012**, *41*, 2545-2561.
- [48] K. Matyjaszewski, *Science* **2011**, *333*, 1104-1105.
- [49] L. Y. Qiu, Y. H. Bae, *Pharmaceutical Research* **2006**, *23*, 1-30.
- [50] A. Lalatsa, A. G. Schätzlein, M. Mazza, T. B. Le, I. F. Uchegbu, *J Control Release* **2012**, *161*, 523-536.
- [51] H. Cabral, K. Miyata, K. Osada, K. Kataoka, *Chemical Reviews* **2018**, *118*, 6844-6892.
- [52] H. Zhang, *ACS Nano* **2015**, *9*, 9451-9469.
- [53] K. G. Goswami, S. Mete, S. S. Chaudhury, P. Sar, E. Ksendzov, C. D. Mukhopadhyay, S. V. Kostjuk, P. De, *ACS Applied Polymer Materials* **2020**, *2*, 2035-2045.
- [54] C. J. Hawker, K. L. Wooley, *Science* **2005**, *309*, 1200-1205.

- [55] A. C. Mendes, E. T. Baran, R. L. Reis, H. S. Azevedo, *WIREs Nanomedicine and Nanobiotechnology* **2013**, *5*, 582-612.
- [56] A.-C. Genix, J. Oberdisse, *Soft Matter* **2018**, *14*, 5161-5179.
- [57] S. Yadav, A. K. Sharma, P. Kumar, *Frontiers in Bioengineering and Biotechnology* **2020**, *8*.
- [58] G. Hattori, Y. Hirai, M. Sawamoto, T. Terashima, *Polymer Chemistry* **2017**, *8*, 7248-7259.
- [59] R. S. Croy, S. G. Kwon, *Current Pharmaceutical Design* **2006**, *12*, 4669-4684.
- [60] B. S. Makhmalzade, F. Chavoshy, *Journal of advanced pharmaceutical technology & research* **2018**, *9*, 2-8.
- [61] J. Liaw, Y. Lin, *J Control Release* **2000**, *68*, 273-282.
- [62] S. Küchler, M. R. Radowski, T. Blaschke, M. Dathe, J. Plendl, R. Haag, M. Schäfer-Korting, K. D. Kramer, *European Journal of Pharmaceutics and Biopharmaceutics* **2009**, *71*, 243-250.
- [63] G. Galeotti, F. De Marchi, E. Hamzehpoor, O. MacLean, M. Rajeswara Rao, Y. Chen, L. V. Besteiro, D. Dettmann, L. Ferrari, F. Frezza, P. M. Sheverdyeva, R. Liu, A. K. Kundu, P. Moras, M. Ebrahimi, M. C. Gallagher, F. Rosei, D. F. Perepichka, G. Contini, *Nature Materials* **2020**, *19*, 874-880.
- [64] A. Maio, I. Pibiri, M. Morreale, F. P. L. Mantia, R. Scaffaro, *Nanomaterials* **2021**, *11*, 1717.
- [65] M. Xu, T. Liang, M. Shi, H. Chen, *Chemical Reviews* **2013**, *113*, 3766-3798.
- [66] K. Zhang, T. H. Lee, J. H. Cha, H. W. Jang, J.-W. Choi, M. Mahmoudi, M. Shokouhimehr, *Scientific Reports* **2019**, *9*, 13739.
- [67] D. Golberg, Y. Bando, Y. Huang, T. Terao, M. Mitome, C. Tang, C. Zhi, *ACS Nano* **2010**, *4*, 2979-2993.
- [68] X. Li, X. Yang, H. Xue, H. Pang, Q. Xu, *EnergyChem* **2020**, *2*, 100027.
- [69] L. Ascherl, T. Sick, J. T. Margraf, S. H. Lapidus, M. Calik, C. Hettstedt, K. Karaghiosoff, M. Döblinger, T. Clark, K. W. Chapman, F. Auras, T. Bein, *Nature Chemistry* **2016**, *8*, 310-316.
- [70] X. Feng, A. D. Schlüter, *Angewandte Chemie International Edition* **2018**, *57*, 13748-13763.
- [71] B. Li, C. Lai, G. Zeng, D. Huang, L. Qin, M. Zhang, M. Cheng, X. Liu, H. Yi, C. Zhou, F. Huang, S. Liu, Y. Fu, *Small* **2019**, *15*, 1804565.
- [72] C. Cheng, S. Li, A. Thomas, N. A. Kotov, R. Haag, *Chemical Reviews* **2017**, *117*, 1826-1914.

- [73] D. Chimene, D. L. Alge, A. K. Gaharwar, *Advanced Materials* **2015**, *27*, 7261-7284.
- [74] L. M. Guiney, X. Wang, T. Xia, A. E. Nel, M. C. Hersam, *ACS Nano* **2018**, *12*, 6360-6377.
- [75] Z. Wang, W. Zhu, Y. Qiu, X. Yi, A. von dem Bussche, A. Kane, H. Gao, K. Koski, R. Hurt, *Chemical Society Reviews* **2016**, *45*, 1750-1780.
- [76] P. van Assenbergh, E. Meinders, J. Geraedts, D. Dodou, *Small* **2018**, *14*, 1801989.
- [77] M. Drost, F. Tu, L. Berger, C. Preischl, W. Zhou, H. Gliemann, C. Wöll, H. Marbach, *ACS Nano* **2018**, *12*, 3825-3835.
- [78] C. Tan, H. Zhang, *Nature Communications* **2015**, *6*, 7873.
- [79] R. Dong, T. Zhang, X. Feng, *Chemical Reviews* **2018**, *118*, 6189-6235.
- [80] D. P. Goronzy, M. Ebrahimi, F. Rosei, Arramel, Y. Fang, S. De Feyter, S. L. Tait, C. Wang, P. H. Beton, A. T. S. Wee, P. S. Weiss, D. F. Perepichka, *ACS Nano* **2018**, *12*, 7445-7481.
- [81] S. Kang, J. Lee, S. Ryu, Y. Kwon, K.-H. Kim, D. H. Jeong, S. R. Paik, B.-S. Kim, *Chemistry of Materials* **2017**, *29*, 3461-3476.
- [82] O. Ourdjini, R. Pawlak, M. Abel, S. Clair, L. Chen, N. Bergeon, M. Sassi, V. Oison, J.-M. Debierre, R. Coratger, L. Porte, *Physical Review B* **2011**, *84*, 125421.
- [83] J. Wang, Z. Ouyang, Z. Ren, J. Li, P. Zhang, G. Wei, Z. Su, *Carbon* **2015**, *89*, 20-30.
- [84] Z. Xu, X. Chu, Y. Wang, H. Zhang, W. Yang, *Chemical Engineering Journal* **2020**, *391*, 123548.
- [85] A. V. Kabanov, S. V. Vinogradov, *Angewandte Chemie International Edition* **2009**, *48*, 5418-5429.
- [86] D. Steinhilber, A. L. Sisson, D. Mangoldt, P. Welker, K. Licha, R. Haag, *Advanced Functional Materials* **2010**, *20*, 4133-4138.
- [87] M. Asadian-Birjand, A. Sousa-Herves, D. Steinhilber, J. C. Cuggino, M. Calderon, *Current Medicinal Chemistry* **2012**, *19*, 5029-5043.
- [88] J.-F. Lutz, J.-M. Lehn, E. W. Meijer, K. Matyjaszewski, *Nature Reviews Materials* **2016**, *1*, 16024.
- [89] S. Sutthasupa, M. Shiotsuki, F. Sanda, *Polymer Journal* **2010**, *42*, 905-915.
- [90] P. A. L. Robert J. Young, *Introduction to Polymers*, 3rd Edition ed., CRC Press, Boca Raton, **2011**.
- [91] T. A. Saleh, V. K. Gupta, in *Nanomaterial and Polymer Membranes* (Eds.: T. A. Saleh, V. K. Gupta), Elsevier, **2016**, pp. 135-160.

- [92] A. Sudo, in *Encyclopedia of Polymeric Nanomaterials* (Eds.: S. Kobayashi, K. Müllen), Springer Berlin Heidelberg, Berlin, Heidelberg, **2021**, pp. 1-11.
- [93] M. Wallert, J. Plaschke, M. Dimde, V. Ahmadi, S. Block, R. Haag, *Macromolecular Materials and Engineering* **2021**, *306*, 2000688.
- [94] M. Gervais, A.-L. Brocas, G. Cendejas, A. Deffieux, S. Carlotti, *Macromolecules* **2010**, *43*, 1778-1784.
- [95] G. L. Gregory, E. M. López-Vidal, A. Buchard, *Chemical Communications* **2017**, *53*, 2198-2217.
- [96] A. L. Sisson, I. Papp, K. Landfester, R. Haag, *Macromolecules* **2009**, *42*, 556-559.
- [97] H. R. Kricheldorf, *Angewandte Chemie International Edition* **2006**, *45*, 5752-5784.
- [98] H. Leuchs, *Berichte der deutschen chemischen Gesellschaft* **1906**, *39*, 857-861.
- [99] F. Wessely, K. Riedl, H. Tuppy, *Monatshefte für Chemie und verwandte Teile anderer Wissenschaften* **1950**, *81*, 861-872.
- [100] E. Katchalski, M. Sela, in *Advances in Protein Chemistry, Vol. 13* (Eds.: C. B. Anfinsen, M. L. Anson, K. Bailey, J. T. Edsall), Academic Press, **1958**, pp. 243-492.
- [101] A. C. Farthing, *Journal of the Chemical Society (Resumed)* **1950**, 3213-3217.
- [102] O. Masanao, K. Ryoichi, N. Hiroyuki, I. Yoshio, *Chemistry Letters* **1973**, *2*, 1143-1144.
- [103] W. H. Daly, D. Poché, *Tetrahedron Letters* **1988**, *29*, 5859-5862.
- [104] Y. Fujita, K. Koga, H.-K. Kim, X.-S. Wang, A. Sudo, H. Nishida, T. Endo, *Journal of Polymer Science Part A: Polymer Chemistry* **2007**, *45*, 5365-5370.
- [105] C. Lavilla, M. Byrne, A. Heise, *Macromolecules* **2016**, *49*, 2942-2947.
- [106] C. D. Vacogne, H. Schlaad, *Polymer* **2017**, *124*, 203-209.
- [107] X. Zhang, M. Oddon, O. Giani, S. Monge, J.-J. Robin, *Macromolecules* **2010**, *43*, 2654-2656.
- [108] Š. Gradišar, E. Žagar, D. Pahovnik, *ACS Macro Letters* **2017**, *6*, 637-640.
- [109] T. J. Deming, *Macromolecules* **1999**, *32*, 4500-4502.
- [110] T. J. Deming, in *Peptide Hybrid Polymers* (Eds.: H.-A. Klok, H. Schlaad), Springer Berlin Heidelberg, Berlin, Heidelberg, **2006**, pp. 1-18.
- [111] T. J. Deming, *Nature* **1997**, *390*, 386-389.
- [112] T. J. Deming, S. A. Curtin, *Journal of the American Chemical Society* **2000**, *122*, 5710-5717.

- [113] C. D. Vacogne, H. Schlaad, *Chemical Communications* **2015**, *51*, 15645-15648.
- [114] S. Yamada, A. Sudo, M. Goto, T. Endo, *RSC Advances* **2014**, *4*, 29890-29896.
- [115] Y. Kamei, A. Nagai, A. Sudo, H. Nishida, K. Kikukawa, T. Endo, *Journal of Polymer Science Part A: Polymer Chemistry* **2008**, *46*, 2649-2657.
- [116] Y. Kamei, A. Sudo, T. Endo, *Macromolecules* **2008**, *41*, 7913-7919.
- [117] S. Yamada, K. Koga, T. Endo, *Journal of Polymer Science Part A: Polymer Chemistry* **2012**, *50*, 2527-2532.
- [118] K. E. Eckhart, F. A. Starvaggi, S. A. Sydlik, *Biomacromolecules* **2020**, *21*, 3878-3886.
- [119] K. Karadag, S. Yamada, T. Endo, *Polymer Bulletin* **2018**, *75*, 5075-5088.
- [120] E. Vlakh, A. Ananyan, N. Zashikhina, A. Hubina, A. Pogodaev, M. Volokitina, V. Sharoyko, T. Tennikova, *Polymers* **2016**, *8*, 212.
- [121] K. E. Gebhardt, S. Ahn, G. Venkatachalam, D. A. Savin, *Langmuir* **2007**, *23*, 2851-2856.
- [122] M. Khuphe, P. D. Thornton, in *Engineering of Biomaterials for Drug Delivery Systems* (Ed.: A. Parambath), Woodhead Publishing, **2018**, pp. 199-228.
- [123] T. Miyazaki, K. Igarashi, Y. Matsumoto, H. Cabral, *ACS Biomaterials Science & Engineering* **2019**, *5*, 5727-5733.
- [124] P. Heller, B. Weber, A. Birke, M. Barz, *Macromolecular Rapid Communications* **2015**, *36*, 38-44.
- [125] Y. Li, G. H. Gao, D. S. Lee, *Journal of Polymer Science Part A: Polymer Chemistry* **2013**, *51*, 4175-4182.
- [126] R. Huisgen, *Angewandte Chemie International Edition in English* **1963**, *2*, 565-598.
- [127] H. C. Kolb, M. G. Finn, K. B. Sharpless, *Angewandte Chemie International Edition* **2001**, *40*, 2004-2021.
- [128] V. V. Rostovtsev, L. G. Green, V. V. Fokin, K. B. Sharpless, *Angewandte Chemie International Edition* **2002**, *41*, 2596-2599.
- [129] C. W. Tornøe, C. Christensen, M. Meldal, *J Org Chem* **2002**, *67*, 3057-3064.
- [130] L. Zhang, X. Chen, P. Xue, H. H. Y. Sun, I. D. Williams, K. B. Sharpless, V. V. Fokin, G. Jia, *Journal of the American Chemical Society* **2005**, *127*, 15998-15999.
- [131] P. Wu, A. K. Feldman, A. K. Nugent, C. J. Hawker, A. Scheel, B. Voit, J. Pyun, J. M. J. Fréchet, K. B. Sharpless, V. V. Fokin, *Angewandte Chemie International Edition* **2004**, *43*, 3928-3932.

- [132] D. J. V. C. van Steenis, O. R. P. David, G. P. F. van Strijdonck, J. H. van Maarseveen, J. N. H. Reek, *Chemical Communications* **2005**, 4333-4335.
- [133] N. Akeroyd, B. Klumperman, *European Polymer Journal* **2011**, *47*, 1207-1231.
- [134] D. Fournier, R. Hoogenboom, U. S. Schubert, *Chemical Society Reviews* **2007**, *36*, 1369-1380.
- [135] M. A. Gauthier, M. I. Gibson, H.-A. Klok, *Angewandte Chemie International Edition* **2009**, *48*, 48-58.
- [136] H. Gao, K. Matyjaszewski, *Macromolecules* **2006**, *39*, 4960-4965.
- [137] B. A. Laurent, S. M. Grayson, *Journal of the American Chemical Society* **2006**, *128*, 4238-4239.
- [138] S. Q. Liu, P. L. Rachel Ee, C. Y. Ke, J. L. Hedrick, Y. Y. Yang, *Biomaterials* **2009**, *30*, 1453-1461.
- [139] K. Kempe, A. Krieg, C. R. Becer, U. S. Schubert, *Chemical Society Reviews* **2012**, *41*, 176-191.
- [140] P. L. Golas, K. Matyjaszewski, *QSAR & Combinatorial Science* **2007**, *26*, 1116-1134.
- [141] Z. Geng, J. J. Shin, Y. Xi, C. J. Hawker, *Journal of Polymer Science* **2021**, *59*, 963-1042.
- [142] Y. Shi, X. Cao, H. Gao, *Nanoscale* **2016**, *8*, 4864-4881.
- [143] J.-F. Lutz, *Macromolecular Rapid Communications* **2017**, *38*, 1700582.
- [144] T.-T.-T. Nguyen, M. Baumgarten, A. Rouhanipour, H. J. Räder, I. Lieberwirth, K. Müllen, *Journal of the American Chemical Society* **2013**, *135*, 4183-4186.
- [145] T. T. Trinh, C. Laure, J.-F. Lutz, *Macromolecular Chemistry and Physics* **2015**, *216*, 1498-1506.
- [146] A. N. Zelikin, F. Stellacci, *Advanced Healthcare Materials* **2021**, *10*, 2001433.
- [147] M. H. V. Van Regenmortel, in *Encyclopedia of Virology (Third Edition)* (Eds.: B. W. J. Mahy, M. H. V. Van Regenmortel), Academic Press, Oxford, **2008**, pp. 137-142.
- [148] S. Kausar, F. Said Khan, M. Ishaq Mujeeb Ur Rehman, M. Akram, M. Riaz, G. Rasool, A. Hamid Khan, I. Saleem, S. Shamim, A. Malik, *Int J Immunopathol Pharmacol* **2021**, *35*, 20587384211002621.
- [149] E. Ruggiero, S. N. Richter, *Nucleic Acids Research* **2018**, *46*, 3270-3283.
- [150] S. T. Jones, *Journal of Materials Science* **2020**, *55*, 9148-9151.
- [151] C. S. Adamson, K. Chibale, R. J. M. Goss, M. Jaspars, D. J. Newman, R. A. Dorrington, *Chemical Society Reviews* **2021**, *50*, 3647-3655.

- [152] K. Kłysik, A. Pietraszek, A. Karewicz, M. Nowakowska, *Curr Med Chem* **2020**, *27*, 4118-4137.
- [153] R. H. Bianculli, J. D. Mase, M. D. Schulz, *Macromolecules* **2020**, *53*, 9158-9186.
- [154] N. Jarach, H. Dodiuk, S. Kenig, *Polymers* **2020**, *12*, 1727.
- [155] R. J. Whitley., in *Medical Microbiology* (Ed.: B. S.), Galveston (TX): University of Texas Medical Branch at Galveston, **1996**.
- [156] W. W. Newcomb, F. L. Homa, D. R. Thomsen, F. P. Booy, B. L. Trus, A. C. Steven, J. V. Spencer, J. C. Brown, *Journal of Molecular Biology* **1996**, *263*, 432-446.
- [157] in *Human Herpesviruses: Biology, Therapy, and Immunoprophylaxis* (Eds.: A. Arvin, G. Campadelli-Fiume, E. Mocarski, P. S. Moore, B. Roizman, R. Whitley, K. Yamanishi), Cambridge University Press Copyright © Cambridge University Press 2007., Cambridge, **2007**.
- [158] A. M. Agelidis, D. Shukla, *Future Virol* **2015**, *10*, 1145-1154.
- [159] A. Zumla, J. F. W. Chan, E. I. Azhar, D. S. C. Hui, K.-Y. Yuen, *Nature Reviews Drug Discovery* **2016**, *15*, 327-347.
- [160] T. Singhal, *The Indian Journal of Pediatrics* **2020**, *87*, 281-286.
- [161] L. E. Gralinski, R. S. Baric, *The Journal of Pathology* **2015**, *235*, 185-195.
- [162] F. He, Y. Deng, W. Li, *Journal of Medical Virology* **2020**, *92*, 719-725.
- [163] A. Banerjee, S. Kulkarni, A. Mukherjee, *Frontiers in Microbiology* **2020**, *11*.
- [164] C. Nie, P. Pouyan, D. Lauster, J. Trimpert, Y. Kerkhoff, G. P. Szekeres, M. Wallert, S. Block, A. K. Sahoo, J. Dervede, K. Pagel, B. B. Kaufer, R. R. Netz, M. Ballauff, R. Haag, *Angewandte Chemie International Edition* **2021**, *60*, 15870-15878.
- [165] N. A. Wong, M. H. Saier, Jr., *International journal of molecular sciences* **2021**, *22*, 1308.
- [166] W. Li, M. J. Moore, N. Vasilieva, J. Sui, S. K. Wong, M. A. Berne, M. Somasundaran, J. L. Sullivan, K. Luzuriaga, T. C. Greenough, H. Choe, M. Farzan, *Nature* **2003**, *426*, 450-454.
- [167] D. Wrapp, N. S. Wang, K. S. Corbett, J. A. Goldsmith, C. L. Hsieh, O. Abiona, B. S. Graham, J. S. McLellan, *Science* **2020**, *367*, 1260-+.
- [168] Y. Huang, C. Yang, X.-f. Xu, W. Xu, S.-w. Liu, *Acta Pharmacologica Sinica* **2020**, *41*, 1141-1149.
- [169] S. Bhatia, L. C. Camacho, R. Haag, *Journal of the American Chemical Society* **2016**, *138*, 8654-8666.

- [170] M. F. Gholami, D. Lauster, K. Ludwig, J. Storm, B. Ziem, N. Severin, C. Böttcher, J. P. Rabe, A. Herrmann, M. Adeli, R. Haag, *Advanced Functional Materials* **2017**, *27*, 1606477.
- [171] B. Ziem, W. Azab, M. F. Gholami, J. P. Rabe, N. Osterrieder, R. Haag, *Nanoscale* **2017**, *9*, 3774-3783.
- [172] I. S. Donskyi, W. Azab, J. L. Cuellar-Camacho, G. Guday, A. Lippitz, W. E. S. Unger, K. Osterrieder, M. Adeli, R. Haag, *Nanoscale* **2019**, *11*, 15804-15809.
- [173] I. S. Donskyi, C. Nie, K. Ludwig, J. Trimpert, R. Ahmed, E. Quaas, K. Achazi, J. Radnik, M. Adeli, R. Haag, K. Osterrieder, *Small* **2021**, *17*, 2007091.
- [174] J. Vonnemann, S. Liese, C. Kuehne, K. Ludwig, J. Dervede, C. Böttcher, R. R. Netz, R. Haag, *Journal of the American Chemical Society* **2015**, *137*, 2572-2579.
- [175] S. Bhatia, I. S. Donskyi, S. Block, C. Nie, A. Burdinski, D. Lauster, J. Radnik, A. Herrmann, R. Haag, K. Ludwig, M. Adeli, *Advanced Materials Interfaces* **2021**, *8*, 2100285.
- [176] D. WuDunn, P. G. Spear, *Journal of Virology* **1989**, *63*, 52-58.
- [177] S. Hong, P. R. Leroueil, E. K. Janus, J. L. Peters, M.-M. Kober, M. T. Islam, B. G. Orr, J. R. Baker, M. M. Banaszak Holl, *Bioconjugate Chemistry* **2006**, *17*, 728-734.
- [178] J. T. Marcio, S. Qin, M. W. Françoise, C. F. Julio, *Current Gene Therapy* **2011**, *11*, 288-306.
- [179] P. D. Somer, E. D. Clercq, A. Billiau, E. Schonne, M. Claesen, *Journal of Virology* **1968**, *2*, 878-885.
- [180] P. D. Somer, E. D. Clercq, A. Billiau, E. Schonne, M. Claesen, *Journal of Virology* **1968**, *2*, 886-893.
- [181] F. Schandock, C. F. Riber, A. Röcker, J. A. Müller, M. Harms, P. Gajda, K. Zuwala, A. H. F. Andersen, K. B. Løvschall, M. Tolstrup, F. Kreppel, J. Münch, A. N. Zelikin, *Advanced Healthcare Materials* **2017**, *6*, 1700748.
- [182] A. Vaillant, *Antiviral Research* **2016**, *133*, 32-40.
- [183] V. Cagno, P. Andreozzi, M. D'Alicarnasso, P. Jacob Silva, M. Mueller, M. Galloux, R. Le Goffic, S. T. Jones, M. Vallino, J. Hodek, J. Weber, S. Sen, E.-R. Janeček, A. Bekdemir, B. Sanavio, C. Martinelli, M. Donalisio, M.-A. Rameix Welti, J.-F. Eleouet, Y. Han, L. Kaiser, L. Vukovic, C. Tapparel, P. Král, S. Krol, D. Lembo, F. Stellacci, *Nature Materials* **2018**, *17*, 195-203.
- [184] C. Fasting, C. A. Schalley, M. Weber, O. Seitz, S. Hecht, B. Koksche, J. Dervede, C. Graf, E.-W. Knapp, R. Haag, *Angewandte Chemie International Edition* **2012**, *51*, 10472-10498.
- [185] M. Mammen, S.-K. Choi, G. M. Whitesides, *Angewandte Chemie International Edition* **1998**, *37*, 2754-2794.

- [186] W. J. Lees, A. Spaltenstein, J. E. Kingery-Wood, G. M. Whitesides, *Journal of Medicinal Chemistry* **1994**, *37*, 3419-3433.
- [187] S. Bhatia, D. Lauster, M. Bardua, K. Ludwig, S. Angioletti-Uberti, N. Popp, U. Hoffmann, F. Paulus, M. Budt, M. Stadtmüller, T. Wolff, A. Hamann, C. Böttcher, A. Herrmann, R. Haag, *Biomaterials* **2017**, *138*, 22-34.
- [188] A. Rosa Borges, L. Wieczorek, B. Johnson, A. J. Benesi, B. K. Brown, R. D. Kensinger, F. C. Krebs, B. Wigdahl, R. Blumenthal, A. Puri, F. E. McCutchan, D. L. Birs, V. R. Polonis, C.-L. Schengrund, *Virology* **2010**, *408*, 80-88.
- [189] R. Doménech, O. Abian, R. Bocanegra, J. Correa, A. Sousa-Herves, R. Riguera, M. G. Mateu, E. Fernandez-Megia, A. Velázquez-Campoy, J. L. Neira, *Biomacromolecules* **2010**, *11*, 2069-2078.
- [190] J. E. Kingery-Wood, K. W. Williams, G. B. Sigal, G. M. Whitesides, *Journal of the American Chemical Society* **1992**, *114*, 7303-7305.
- [191] G. L. Hendricks, L. Velazquez, S. Pham, N. Qaisar, J. C. Delaney, K. Viswanathan, L. Albers, J. C. Comolli, Z. Shriver, D. M. Knipe, E. A. Kurt-Jones, D. K. Fygenon, J. M. Trevejo, J. P. Wang, R. W. Finberg, *Antiviral Research* **2015**, *116*, 34-44.
- [192] I. Papp, C. Sieben, A. L. Sisson, J. Kostka, C. Böttcher, K. Ludwig, A. Herrmann, R. Haag, *ChemBioChem* **2011**, *12*, 887-895.
- [193] A. A. Date, C. J. Destache, *Biomaterials* **2013**, *34*, 6202-6228.
- [194] J. Haldar, D. An, L. Álvarez de Cienfuegos, J. Chen, A. M. Klibanov, *Proceedings of the National Academy of Sciences* **2006**, *103*, 17667-17671.
- [195] D. Park, J. Wang, A. M. Klibanov, *Biotechnology Progress* **2006**, *22*, 584-589.
- [196] J. Haldar, A. K. Weight, A. M. Klibanov, *Nature Protocols* **2007**, *2*, 2412-2417.
- [197] E. Fröhlich, *International journal of nanomedicine* **2012**, *7*, 5577-5591.
- [198] S. T. Jones, V. Cagno, M. Janeček, D. Ortiz, N. Gasilova, J. Piret, M. Gasbarri, D. A. Constant, Y. Han, L. Vuković, P. Král, L. Kaiser, S. Huang, S. Constant, K. Kirkegaard, G. Boivin, F. Stellacci, C. Tapparel, *Science advances* **2020**, *6*, eaax9318-eaax9318.
- [199] O. Kocabiyik, V. Cagno, P. J. Silva, Y. Zhu, L. Sedano, Y. Bhide, J. Mettier, C. Medaglia, B. Da Costa, S. Constant, S. Huang, L. Kaiser, W. L. J. Hinrichs, A. Huckriede, R. Le Goffic, C. Tapparel, F. Stellacci, *Advanced Science* **2021**, *8*, 2001012.
- [200] M. E. Lane, *Int J Pharm* **2013**, *447*, 12-21.
- [201] Y.-Q. Yu, X. Yang, X.-F. Wu, Y.-B. Fan, *Frontiers in Bioengineering and Biotechnology* **2021**, *9*.
- [202] M. R. Prausnitz, R. Langer, *Nature Biotechnology* **2008**, *26*, 1261-1268.

- [203] H. Trommer, R. H. H. Neubert, *Skin Pharmacology and Physiology* **2006**, *19*, 106-121.
- [204] A. Vogt, C. Wischke, A. T. Neffe, N. Ma, U. Alexiev, A. Lendlein, *Journal of Controlled Release* **2016**, *242*, 3-15.
- [205] R. D. Mosteller, *N Engl J Med* **1987**, *317*, 1098.
- [206] K. A. Walters, M. S. Roberts, in *Dermatological and Transdermal Formulations* (Ed.: K. A. Walters), CRC Press, Boca Raton, **2002**.
- [207] E. Kahraman, S. Güngör, Y. Özsoy, *Therapeutic Delivery* **2017**, *8*, 967-985.
- [208] J. Lademann, F. Knorr, H. Richter, U. Blume-Peytavi, A. Vogt, C. Antoniou, W. Sterry, A. Patzelt, *Skin Pharmacology and Physiology* **2008**, *21*, 150-155.
- [209] J. Lademann, F. Knorr, H. Richter, U. Blume-Peytavi, A. Vogt, C. Antoniou, W. Sterry, A. Patzelt, *Skin Pharmacol Physiol* **2008**, *21*, 150-155.
- [210] M. Dimde, F. F. Sahle, V. Wycisk, D. Steinhilber, L. C. Camacho, K. Licha, J. Lademann, R. Haag, *Macromolecular Bioscience* **2017**, *17*, 1600505.
- [211] S. Wang, D. Zeng, J. Niu, H. Wang, L. Wang, Q. Li, C. Li, H. Song, J. Chang, L. Zhang, *Journal of Materials Chemistry B* **2014**, *2*, 877-884.
- [212] M. Lapteva, K. Mondon, M. Möller, R. Gurny, Y. N. Kalia, *Molecular Pharmaceutics* **2014**, *11*, 2989-3001.
- [213] U. Agrawal, N. K. Mehra, U. Gupta, N. K. Jain, *Journal of Drug Targeting* **2013**, *21*, 497-506.
- [214] Y. G. Bachhav, K. Mondon, Y. N. Kalia, R. Gurny, M. Möller, *Journal of Controlled Release* **2011**, *153*, 126-132.
- [215] E. López-Ramírez, C. Chapa-González, C. A. Martínez-Peréz, R. Escobedo-González, M. I. Nicolás Vázquez, F. Medellín-Rodríguez, P. E. García-Casillas, *Journal of Drug Delivery Science and Technology* **2021**, *64*, 102630.
- [216] J. Frombach, M. Unbehauen, I. N. Kurniasih, F. Schumacher, P. Volz, S. Hadam, F. Rancan, U. Blume-Peytavi, B. Kleuser, R. Haag, U. Alexiev, A. Vogt, *Journal of Controlled Release* **2019**, *299*, 138-148.
- [217] D. Papakostas, F. Rancan, W. Sterry, U. Blume-Peytavi, A. Vogt, *Archives of dermatological research* **2011**, *303*, 533.
- [218] Y. Yang, S. Sunoqrot, C. Stowell, J. Ji, C.-W. Lee, J. W. Kim, S. A. Khan, S. Hong, *Biomacromolecules* **2012**, *13*, 2154-2162.
- [219] J. Lademann, F. Knorr, H. Richter, S. Jung, M. C. Meinke, E. Rühl, U. Alexiev, M. Calderon, A. Patzelt, *Journal of Innovative Optical Health Sciences* **2015**, *08*, 1530004.

- [220] F. F. Sahle, M. Giubudagian, J. Bergueiro, J. Lademann, M. Calderón, *Nanoscale* **2017**, *9*, 172-182.
- [221] J. Yoo, S. Shanmugam, C.-K. Song, D.-D. Kim, H.-G. Choi, C.-S. Yong, J.-S. Woo, B. K. Yoo, *Archives of Pharmacal Research* **2008**, *31*, 1652-1658.
- [222] V. V. Venuganti, P. Sahdev, M. Hildreth, X. Guan, O. Perumal, *Pharmaceutical Research* **2011**, *28*, 2246.
- [223] M. N. Stadtmueller, S. Bhatia, P. Kiran, M. Hilsch, V. Reiter-Scherer, L. Adam, B. Parshad, M. Budt, S. Klenk, K. Sellrie, D. Lauster, P. H. Seeberger, C. P. R. Hackenberger, A. Herrmann, R. Haag, T. Wolff, *Journal of Medicinal Chemistry* **2021**, *64*, 12774-12789.
- [224] K. Numata, *Polymer Journal* **2015**, *47*, 537-545.
- [225] H.-A. Klok, *Angewandte Chemie International Edition* **2002**, *41*, 1509-1513.
- [226] E. Mohammadifar, V. Ahmadi, M. F. Gholami, A. Oehrl, O. Kolyvushko, C. Nie, I. S. Donskyi, S. Herziger, J. Radnik, K. Ludwig, C. Böttcher, J. P. Rabe, K. Osterrieder, W. Azab, R. Haag, M. Adeli, *Advanced Functional Materials* **2021**, *31*, 2009003.
- [227] V. Ahmadi, C. Nie, E. Mohammadifar, K. Achazi, S. Wedepohl, Y. Kerkhoff, S. Block, K. Osterrieder, R. Haag, *Chemical Communications* **2021**, *57*, 11948-11951.
- [228] V. Ahmadi, F. Zabihi, F. Rancan, A. A. Staszak, C. Nie, M. Dimde, K. Achazi, A. Wiehe, A. Vogt, R. Haag, *ACS Applied Nano Materials* **2021**, *4*, 6709-6721.

8 Appendix

8.1 List of abbreviations

2D	two-dimensional
2DN	2D nanomaterials
3D	three-dimensional
ACE2	angiotensin-converting enzyme 2
ADMET	acyclic diene metathesis
AFM	atomic force microscopy
AM	activated monomer
ARGET	activators regenerated by electron transfer
AROP	anionic ring-opening polymerization
ATRP	atom-transfer radical polymerization
BP	black phosphorus
Bn	benzyl
CAC	critical aggregation concentration
CH ₂ Cl ₂	dichloromethane (DCM)
CMC	critical micellization concentration
COF	covalent organic frameworks
COVID-19	corona virus disease 19
CoVs	Coronaviruses
CRP	controlled radical polymerization
CuAAC	copper catalyzed azide alkyne cycloaddition
DDS	drug delivery system
DMF	<i>N,N'</i> -Dimethylformamide
DLS	dynamic light scattering
DP _n	degree of polymerization
eq.	equivalent
FDA	food and drug administration
G	generation
GPC	gel permeation chromatography
h	hour
hPG	hyperbranched polyglycerol
hPGS	hyperbranched polyglycerol sulfate
HSPG	heparan sulfate proteoglycans
Hz	herz
HS	heparan sulfate

HSPGs	heparan sulfate proteoglycans
HSV-1	herpes simplex virus type 1
IAV	influenza A virus
IC50	half maximal inhibitory concentration
ICAR	initiators for continuous activator regeneration
J	coupling constant
LPG	linear polyglycerol
LPGS	linear polyglycerol sulfate
MALDI-ToF	Matrix Assisted Laser Desorption Ionization Time-of-Flight
MeOH	methanol
MeOK	potassium methoxide
MOF	metal-organic frameworks
NA	normal amine
NCA	<i>N</i> -carboxyanhydride
NG	nanogel
NMP	nitroxide-mediated polymerization
NMs	nanomaterials
NMP	<i>N</i> -methyl pyrrolidin-2-on
NMR	Nuclear Magnetic Resonance
NP	nanoparticle
NTA	<i>N</i> -thiocarboxyanhydride
PAMAM	poly(amidoamine)
PDI	poly dispersity index
PEG	polyethylene glycol
PEI	polyethyleneimines
PEO	polyethylne oxide
PG	polyglycerol
PGA	poly(glutamic acid)
ppm	parts per million
Ph	phenyl
RAFT	reversible addition–fragmentation chain-transfer polymerization
RBD	receptor binding domain
ROP	ring opening polymerization
ROMP	ring-opening metathesis polymerization
RSV	respiratory syncytial virus
SARA	supplemental activator and reducing agent

SARS-CoV-2	severe acute respiratory syndrome coronavirus 2
SPPS	Solid Phase Peptide Synthesis
TEM	transmission electron microscopy
TFA	Trifluoroacetic acid
TLC	Thin Layer Chromatography
TMP	1,1,1-tris (hydroxymethyl) propane
TMRSS2	TM protease serine 2
TRGO	thermally reduced graphene oxide

8.2 List of publications, patents, and Conference Contributions

Publications

V. Ahmadi,* C. Nie, E. Mohammadifar, K. Achazi, S. Wedepohl, Y. Kerkhoff, S. Block, K. Osterrieder, and R. Haag,* *One-pot gram-scale synthesis of virucidal heparin-mimicking polymers as HSV1 inhibitors. ChemCommun.*, 2021, **57**, 11948-11951.

V. Ahmadi, F. Zabihi, F. Rancan, A. A. Staszak, M. Dimde, K. Achazi, A. Vogt, and R. Haag,* *Amphiphilic Co-polypeptides Self-Assembled into Spherical Nanoparticles for Dermal Drug Delivery, ACS Appl. Nano Mater.* 2021, **4**, 7, 6709–6721

E. Mohammadifar, † **V. Ahmadi**, † M.F. Gholami, A. Oehrl, O. Kolyvushko, C. Nie, I. S. Donskyi, S. Ehrmann, J. Radnik, C. Böttcher, J. P. Rabe, K. Osterrieder, W. Azab, R. Haag,* M. Adeli,* *Graphene-Assisted Synthesis of 2D Polyglycerols as Innovative Platforms for Multivalent Virus Interactions, Adv. Funct. Mater.* 2021, 202009003.

† *These authors contributed equally to this work.*

M. Wallert, J. Plaschke, M. Dimde, **V. Ahmadi**, S. Block,* R. Haag,* *Automated Solvent-Free Polymerization of Hyperbranched Polyglycerol with Tailored Molecular Weight by Online Torque Detection, Macromol. Mater. Eng.* 2021, **306** (7), 2000688.

C. Nie, M. Stadtmüller, B. Parshad, M. Wallert, **V. Ahmadi**, Y. Kerkhoff, S. Bhatia, S. Block,* C. Cheng,* T. Wolff,* R. Haag,* *Heteromultivalent topology-matched nanostructures as potent and broad-spectrum influenza A virus inhibitors, Sci. Adv.*, 2021, **7** (1), eabd3803.

Poster presentation

V. Ahmadi, M. Ferraro, P. Pouyan, E. Mohammadifar, M. Tully, and R. Haag. *Biocompatible Polyglycerols as Versatile Platform for Biomedical Applications. Innovative polymers for the nanomedicine of 21st century*, 2019. Conference, Jena, Germany.

V. Ahmadi, F. Zabihi, F. Rancan, K. Achazi, A. Vogt, and R. Haag, *Synthesis of pH-sensitive polypeptide-based nanocarriers for dermal delivery application.*, Macromolecular Colloquium Freiburg 2021.

V. Ahmadi, E. Mohammadifar, M. Fardin Gholami, A. Oehrl, J. P. Rabe, M. Adeli, and Rainer Haag. Two-dimensional Hyperbranched Polyglycerol Innovative Platform for Robust Multivalent Interactions at Biointerfaces. *Frontiers in polymer science*.2019, Budapest, Hungary.

Patent

"VIRUCIDAL COATING ARRANGEMENT", Europäische Patentanmeldung Nr. 21 154 393.9

8.3 Curriculum Vitae

Der Lebenslauf ist aus Gründen des Datenschutzes nicht enthalten.